Ferromagnetic Resonance for Investigating Magnetization Dynamics in Magnetic Thin Films

نفیس مقناطیسی پرتوں میں مقناطیسی حرکیات جانچنے کے لیے مقناطیسی گونج کا طریقہ

Muhammad Basit

Acknowledgments

First and foremost, thanks to ALLAH, the Almighty, for His divine benison on me throughout my life. May ALLAH's blessings shower upon His Prophet Muhammad (peace be upon him) and his family.

My deep gratitude and sincerest thanks goes first to my advisor, Dr. Muhammad Sabieh Anwar, who expertly provided me with his invaluable guidance throughout my research. His heartiness, vigor and pizzazz for science kept me constantly engaged with my research to unveil new insights. He has taught me the scientific approach towards research and to present the research with utmost clarity. I'm extremely obliged for his kindness and patience throughout these two years. I would also like to thank him for his amity, empathy and the warmth. It was a great honor to work and study under his supervision. I also express my warmest gratitude to my co-advisor, Dr. Ali Akbar, without his continuous optimism and concern this study would hardly have been completed. I can't thank him enough for his kind support, friendship and encouragement throughout my research period. I'm extremely grateful for what he has taught me.

This study could not be completed without the ongoing efforts of my fellows and friends, Wardah Mehmood, Bilal Azam, Bisma Haq and Muhammad Ali, who stood by me to complete this challenging task. I'd also like to thank Shahbaz Khan from University of Western Australia for providing the required samples and timely suggestions. My appreciation also extended to Physlab's team members and technical staff from whom I got significant help, Muhammad Shafique, Muhammad Rizwan, Khadim Mehmood, Ayaz Mehmood and Ali Sabir. Their

monitoring and encouragement have been especially valuable. A special thanks to Hafsa Shahbaz Virk for being there all the time and providing the enormous amount of emotional support. Above all, I am indebted to my family for supporting me spiritually throughout my life, for providing inspiration and for making me what I am today. Specially, the love and care of parents are deep sources of solace I needed to mitigate the stress and pressure.

At last, I'd like to thank National Research Program for Universities (NRPU-10375) from the Higher Education Commission (HEC) of Pakistan for providing the financial support.

اماں جی کے نام

موضوعِ مقالہ، حجتِ تحقیق

گذشتہ چند برس میں وسیع فریکوئنسی بساط میں مقناطیسی مواد کی خصوصیات کی چھان بین کے لیے تحقیق میں خاطر خواہ پیش رفت ہوئی ہے۔ مقناطیسی مواد کی ایک اہم خاصیت، مقناطیسی حرکیات ہے، جس کے نتیجے میں مقناطیسی مواد ایک حالت سے دوسری حالت میں منتقل ہو جاتا ہے۔ یہ مقناطیسی تبدیلی، مِثال کے طور پہ ہمارے کمپیوٹر میں معلومات کی نگہداشت اور ذخیرہ کرنے والی ہارڈ ڈسک کے استعمال میں لائی جاتی ہے۔ متذکرہ تبدیلی کا انحصار مختلف عوامل پہ ہوتا ہے جس سے مقناطیسی مواد کی خصوصیات ،اس کی ایٹمی ساخت اور مقناطیسی نفیس پرتوں کا طول و عرض پہ ہے۔ بنیادی طور پہ مقناطیسی مواد پہ برقی مقناطیسی تابکاری[a] کے ساتھ تعامل کو جانچا جاتا ہے، خواہ آپ بیرونی مقناطیسی میدان[b] کو روبہ عمل کریں یا نہیں ،اور اس تعامل سے مقناطیسی مواد کی مقناطیسی خصوصیات میں کچھ تبدیلیاں کیونکر متاثر ہوتی ہیں۔ یہی ہمارے مقالے کا مرکزی خیال ہے۔

سائنسی تحقیق اور صنعت میں مقناطیسی حرکیات کی اہمیت سے گریز نہیں کیا جا سکتا۔ مثال کے طور پہ صنعتوں میں مائکروویو ارتعاش[c] کے استعمال پہ منحصر آلات، یاداشتی آلات اور کمپیوٹر ٹیکنالوجی میں مقناطیسی حرکیات کا استعمال اب کسی سے ڈھکا چھُپا نہیں۔ ان آلات نے نفیس مقناطیسی پرتوں کی جامد اور متحرک مقناطیسی خصوصیات کی تفہیم کے سلسلے میں حقائق کے نئے، انوکھے اور علم افزا در وا کیئے ہیں۔ لہذا، مقناطیسی حرکیات کی بنیادی خصوصیات میں تحقیق کی بہت گنجائش ہے۔ زیرِ نظر مقالے میں ہم نے مقناطیسی حرکیات کی کامل پیمائش کے لیے ایک آلہ تخلیق کیا ہے، جو دو مختلف زاویوں سے کام کرتا ہے اور نفیس پرتوں، جن کی موٹائی سو نینو میٹر سے کم ہے، میں فیرو مقناطیسی گونج کو ڈھونڈتا اور گرفت میں لا کے نپے تلے اعداد و شمار فراہم کرتا ہے۔ اس سے ہمیں مواد کی مقناطیسی حیثیت جاننے میں مدد ملتی ہے۔

[a] Electromagnetic radiation

[b] Magnetic field

[c] Microwave radiation

خلاصہِ تحقیق

یہ مقالہ جس طرح منظم کیا گیا ہے اس کا خاکہ پیش ہے۔
پہلے حصے میں فیرو مقناطیسی گونج[a] کا مطالعہ کیا گیا ہے جو کہ ایک شاندار اور کارآمد تکنیک ہے[b] جو فیرو اور فیری مقناطیسی مواد میں مقناطیسی حرکیات اور خصوصیات کے بارے میں معلومات فراہم کرتی ہے۔اس تکنیک میں یہ دیکھا جاتا ہے کہ مادہ برقی مقناطیسی توانائی[c] کو کسی طرح جذب کرتا ہے۔ جب ایک یکساں مقناطیسی میدان کی موجودگی میں مادے پہ برقی مقناطیسی موجیں ڈالی جاتی ہے تو کرسٹل میں جوش آتا ہے اور اس میں گونج اس وقت پیدا ہوتی ہے جب اطلاق شدہ مقناطیسی میدان پیش کی گئی فریکونسی کے ساتھ میل کھاتا ہے۔ مختصراً ہماری اس تحقیق کا مقصد اس گونج کو ماپنے کے لیے آلات کی تیاری ہے اور ساتھ ہی ساتھ ان کی مکمل جانچ پڑتال اور افادیت کے تمام پہلوؤں کو سمجھنے اور ناپنے کی کوشش ہے۔
مقالے کے دوسرے حصے میں مقناطیسی متحرک حرکت کے بنیادی اصولوں کو نظریاتی پسِ منظر کے ساتھ پیش کیا گیا ہے۔ لینڈو، لیفشٹز اور گلبرٹ کی مساوات[d] اور اس کے حل کی وضاحت بھی شامل کی گئی ہے۔ساتھ ہی مقناطیسیت کی مخالفت میں پید ہونے والے میدان[e] اور مقناطیسیی خصوصیات میں سمتی انحصار کی وضاحت کی گئی ہے۔ جسکا مطلب یہ ہے کہ مقناطیسی مادے میں مقناطیسیت کے لیئے سخت اور آسان محور قائم ہو جاتے ہیں۔اس حصے میں نہایت نفیس مقناطیسی پرتوں کی جیومیٹری کو کیٹل کی مساوات[f] کی مدد سے پرکھا کیا گیا ہے جو مقناطیسی سمتی انحصار کی مراعات کو شامل کر کے گونج کی حالت کا بخوبی تعین کرتی ہے۔چُنانچہ اس حصے کا بنیادی مقصد ایک مضبوط نظریاتی پس منظر تیار کرنا ہے جو بعد میں ہم اپنے تجرباتی اعداد و شمار اور تجربے کی نظریاتی پیش گویوں کے موازنے کے لیے استعمال کریں گے۔
تیسرے اور آخری حصے میں تجرباتی کام اور کلیدی نتائج پہ سیر حامل بحث کی گئی ہے۔اس کا آغاز فیرو مقناطیسی گونج کی پیمائش کے لیے نمونہ تیار کرنے کے عمل اور تجرباتی آلات اور جزئیات کی ترتیب اور تعمیر کی تفصیلات سے ہوتا ہے۔

[a] Ferromagnetic resonance
[b] Ferrimagnetic
[c] Electromagnetic radiation
[d] LLG equation
[e] Demagnetizing fields
[f] Kittel's equation

مقناطیسی آلات اور سخت محوروں کے تعین میں مستعمل تجرباتی سیٹ اپ کی وضاحت بھی کی گئی ہے۔ اس باب میں دو آلات یعنی ویکٹر نیٹ ورک پیما[a] اور لاک ان ایمپلیفائر[b] کی مدد سے گونج کی پیمائش کا خاکہ پیش کیا گیا ہے نیز تیار کردہ تجربے سے حاصل کردہ نتائج اس مقالے کا اہم حصہ ہیں۔ ان نتائج سے مختلف نفیس پرتوں میں مقناطیسیت سے متعلق اہم کیفیات کے بارے میں کارآمد اعداد و شمار اخذ کیے گئے ہیں اور ان کا دیگر محققین کے نتائج سے کماحقہٗ، موازنہ بھی کیا گیا ہے۔ امید ہے کہ یہ تحقیقی کاوِش فیرو مقناطیسی گونج کے حوالے سے دیگر طلبہ، اساتذہ اور محققین کے لیے ایک مفید اور دیرپا مقالے کے طور پر قبولِ عام حاصل کرے گی۔

[a] Vector network analyzer

[b] Lock-in amplifier

Abstract

Ferromagnetic resonance describes the precessional motion of magnetization in the ferromagnetic material under the influence of an external magnetic field. This study mainly focuses on the design and construction of a broadband ferromagnetic resonance system for probing the magnetization dynamics of magnetic thin films in the microwave frequency range (up to 8 GHz). We have developed two measurement techniques: measurement with the help of a vector network analyzer (VNA-FMR) and with lock-in detection (LI-FMR). Resonance is induced in the thin film with a coplanar waveguide (CPW) or a stripline, and the change in electromagnetic energy has been examined with frequency and magnetic field sweeps. Both of these techniques employ a flip-chip setup in which the sample is placed face-down on the stripline. The frequency swept VNA-FMR technique unravels static magnetic properties such as saturation induction, anisotropy fields, effective magnetization and Landé g-factor, whereas, the lock-in detection measures complementary dynamic properties of magnetic thin films which such as damping and loss mechanisms. Both of the setups that we've developed in this work are capable of conducting broadband frequency and magnetic field swept measurements in the in-plane (IP) and out-of-plane (OOP) orientations. The present study will be helpful in enhancing the magnetic properties of ferromagnetic materials by doing the full angle dependent measurements in both IP and OOP orientations.

Contents

1 An Overview **24**

2 An Introduction to Broadband Ferromagnetic Resonance **28**

2.1 The Magnetic Moment 29

2.2 The Bloch Equation 30

2.3 The Landau-Lifshitz-Gilbert Equation 33

2.4 Effects of Demagnetizing Fields 36

2.5 Susceptibility Tensor 38

2.6 Kittel's Equation 42

2.7 Effects of Crystalline Anisotropy Energy 44

2.8 Smit-Beljers Equation 47

2.9 Concluding Remarks 49

3 VNA Based Experimental Setups and Measurement Techniques for FMR **50**

3.1 Thin Film Deposition 52

3.2 Magneto-optic Kerr Effect 54

3.3 Introduction to S-Parameters and VNA 56

3.4 Basics of Waveguides for FMR 58

3.5 FMR with the VNA and Z-Line 60

3.5.1 Frequency Swept FMR 60

3.5.2 Analytical Evaluation of Measurement Parameters 64
3.5.2.1 Field Linewidth 65
3.5.2.2 Frequency Linewidth 66
3.5.3 Experimental Methods for IP VNA-FMR Measurements . 67
3.6 Results from the IP VNA-FMR Scheme 70
3.7 Extraction of Measurement Parameters 72
3.7.1 Resonance Frequency 72
3.7.2 Gyromagnetic Ratio and Saturation Magnetization 74
3.7.3 Gilbert's Damping Parameter 75

4 Lock-In Amplifier Based Phase Sensitive Detection of FMR 78
4.1 Basics of the Lock-In Amplifier 79
4.2 Experimental Method for Lock-In Detection Based FMR 82
4.2.1 Overview of Field Swept FMR 82
4.2.2 Individual Testing of RF Components 83
4.2.3 The Experiment Itself 86
4.3 Results from the IP LI-FMR Scheme 88
4.4 Extraction of Measurement Parameters 90
4.4.1 Resonant Field 90
4.4.2 Gyromagnetic Ratio and Saturation Magnetization 91
4.4.3 Gilbert's Damping Parameter 92

5 Conclusion and Future Outlook 95
5.1 Limitations 95
5.2 Future Perspectives 96

A The First Appendix 99
A.1 Modulation Amplitudes of Magnetization 99

A.2 Few Words on Spin Orbit Torque 102
A.3 SMA Cable Holder Drawing 103
A.4 LabView Interface for FMR Setup 104
A.5 FMR Spectrum of S1 with Lock-In Detection 106
A.6 FMR Source Codes 106
A.6.1 Matlab Script for Data Extraction 106
A.6.2 Python Scripts for Extraction of Measurement Parameters 111

Bibliography **118**

List of Figures

2.1 Magnetization dynamics in which the magnetization ($\mathbf{M}$) is precessing around the effective magnetic field ($\mathbf{H}_{\text{eff}}$). In a) $\mathbf{M}$ is precessing around $\mathbf{H}_{\text{eff}}$ indefinitely under the action of precessional torque τ_P, whereas b) shows the damped precession of $\mathbf{M}$ around $\mathbf{H}_{\text{eff}}$, invoking the extra damping torque τ_D. 33

2.2 Attenuated magnetization precession around the effective magnetic field for $\alpha > 0$. 34

2.3 Time evolution of different components of magnetization ($\mathbf{M}$) for different damping constants under different initial conditions. In *a*) $\alpha = 0.1$, $\mathrm{H}_z = 5$ T and $\mathbf{M}_\mathrm{o} = (1, 0, 0)$ and *b*) $\alpha = 0.05$, $\mathrm{H}_z = 15$ T and $\mathbf{M}_\mathrm{o} = (1, 0, 0)$. Here $\mathbf{M}_\mathrm{o}$ represents the initial magnetization vector. 35

2.4 Graphs of real and imaginary parts of complex susceptibility tensor as a function of resonance frequency (ω_o) for a fixed value of magnetic field. In a) the real and imaginary parts of χ_{xx} are shown, whereas b) shows the real and imaginary parts χ_{xy}. 42

2.5 Graphs of resonant FMR frequency (ω_o) as a function of external magnetic field ($\mathbf{H_o}$) for a ferromagnetic material. In a) the resonant condition for a spherical geometry is shown, b) shows the resonant condition for a thin film with OOP magnetization $< H_a$, c) shows the resonant condition for a thin film with OOP magnetization $> H_a$ and d) presents the resonant condition for a thin film with IP magnetization. Here H_a represents the anisotropy field. 45

2.6 Sample geometry of equilibrium magnetization and applied magnetic field. 48

3.1 In-plane and out-of-plane configurations of an FMR system. In a) in-plane configuration is shown with magnetization parallel to applied magnetic field, whereas b) shows the out-of-plane configuration with magnetization perpendicular to applied magnetic field. 51

3.2 Different geometries of MOKE. In a) longitudinal geometry (L-MOKE) is shown in which **M** is parallel to the plane of incidence and sample surface, b) shows polar geometry (P-MOKE) in which **M** is parallel to the plane of incidence but perpendicular to the sample surface and c) transverse geometry in which **M** is perpendicular to the plane of incidence but parallel to the sample surface. 54

3.3 Experimental setup of the longitudinal MOKE geometry in which **M** is parallel to the plane of incidence and sample surface. Path taken by beam is shown in aqua color, where **L**= laser, **P**= polarizer, **B**= beam-splitter, **F**= focusing lens, **EM**= electromagnet, **S**= sample, **PEM**= photoelastic modulator, **A**= analyzer, **I**= iris, **D**= detector and **M**= mirror. 55

3.4 Experimental setup of the polar MOKE geometry in which **M** is parallel to the plane of incidence but perpendicular to the sample surface. Components identifies are the same as in Figure 3.3. . . . 55

3.5 Graphs of intensity data obtained from lock-in amplifier as a function of external applied magnetic field ($\mathbf{H_o}$). In a) experimental result of L-MOKE for a 20 nm permalloy thin film is shown, whereas b) shows the experimental result of P-MOKE for the same thin film. 56

3.6 Interface between the VNA and the DUT. 57

3.7 A schematic illustration of waveguides for FMR. In a) the geometry of grounded-CPW is shown, whereas b) shows the geometry of strilpline. 59

3.8 Lab built CPW and Z-shaped stripline with end-launch connectors. 59

3.9 Graph of differential transmission scattering parameter ($\mathrm{d}_D\mathrm{S}_{21}$) as a function of resonance frequency (ω_o) for a fixed value of external magnetic field ($\mathbf{H}_\mathrm{o}$). 63

3.10 Graph of resonance frequency (ω_o) as a function of external magnetic field ($\mathbf{H}_\mathrm{o}$) for a thin film in which $\mathbf{H}_\mathrm{o}$ is perpendicular to the surface of thin film. 64

3.11 A schematic illustration of VNA-FMR spectrometer with IP frequency swept technique. The DUT is placed between the electromagnet and VNA works in tandem as a source and as a detector. 68

3.12 Plane view of the DUT placed inside the VNA-FMR spectrometer with frequency swept technique in IP configuration, in which a 100 nm permalloy sample ($S4$) is placed on the Z−line. 69

3.13 Graphs of resonance frequency ($\omega_o/2\pi$) plotted against the differential real part of transmission coefficient (dS_{21}) for $S2$ and $S3$ with $\mathbf{H}_o$ applied parallel to the plane of thin films, where $\mathbf{a}$ = 0.45 mT−74.6 mT, $\mathbf{b}$ = 1.35 mT−74.6 mT, $\mathbf{c}$ = 2.16 mT−74.6 mT and $\mathbf{d}$ = 3.08 mT−74.6 mT. Solid lines are guide to the eyes. . . . 70

3.14 Graph of resonant frequency ($\omega_o/2\pi$) plotted against the differential real part of transmission parameter (dS_{21}) for the 100 nm permalloy thin film, where $\mathbf{a}$ = 0.45 mT−74.6 mT, $\mathbf{b}$ = 1.35 mT−74.6 mT, $\mathbf{c}$ = 2.16 mT−74.6 mT and $\mathbf{d}$ = 3.08 mT−74.6 mT. Solid lines are guide to the eyes. 71

3.15 Real and imaginary parts of a specific portion of FMR data plotted against the resonance frequency ($\omega_o/2\pi$) for the 49 nm, 72 nm and 100 nm permalloy thin film samples. Solid lines are the least square curve fit to the experimental data. The data is fit to Eqs. (3.14) and (3.15). 73

3.16 Graphs of static magnetic field ($\mathbf{H}_o$) as a function of resonance frequency ($\omega_o/2\pi$) for $S2$ and $S3$ in IP configuration are shown in a) and b), respectively. Solid lines are least square curve fit to the experimental data. The data is fit to Eq. (2.53). 74

3.17 Graph of static magnetic field ($\mathbf{H}_o$) plotted against the resonant frequency ($\omega/2\pi$) for $S4$ in IP configuration. Solid line is least square curve fit to the experimental data. 75

3.18 Graphs of resonant frequency ($\omega_o/2\pi$) plotted against the linewidth (FWHM) for $S2$ and $S3$ in IP configuration are shown in a) and b), respectively. Solid lines are least square curve fit to the experimental data. The data is fit against Eq. (3.24). 76

3.19 Graph of resonant frequency ($\omega/2\pi$) plotted against the linewidth (FWHM) for $S4$ in IP configuration. Solid lines are least square curve fit to the experimental data. The data is fit against Eq. (3.24). 76

4.1 Block diagram of phase-sensitive lock-in amplifier, where **Amp=** amplifier, **PSD=** phase-sensitive detection box, **M=** mixer and **L.P=** low pas filter. 79

4.2 A schematic illustration of IP field swept LI-FMR spectrometer. The DUT is placed between the electromagnet and a pair of Helmholtz coils. A lock-in amplifier is also used to detect the output signal coming from the rf power detectors. 82

4.3 Block diagram of an oscilloscope interface showing an rf output of 530 mV when an rf input signal of 50 MHz and 0 dBm power is generated by the microwave source. 84

4.4 Block diagram of an oscilloscope interface showing rf outputs of 254 and 250 mV at port-1 and port-2 of the power splitter, respectively. An rf input signal of 50 MHz and 0 dBm power is applied to the Port-S of power splitter. 85

4.5 Block diagram of an oscilloscope interface showing an rf output of 249.1 mV and coupled rf output of 24.9 mV for a 10 dB directional coupler. An rf input signal of 50 MHz and 0 dBm power is applied to the directional coupler. 85

4.6 Block diagram of an oscilloscope interface showing the dc outputs of 870 mV for two rf power detectors. An rf input signal of 50 MHz and 0 dBm power is applied to the power splitter. 86

4.7 Experimental setup of lock-in detection based FMR spectrometer with field sweep technique in IP configuration. The DUT is placed between the electromagnets and a pair of Helmholtz coils. The lock-in amplifier compares the rf microwave signal coming from power detector (D1) and an rf FMR signal coming from power detector (D2) in A-B mode for higher sensitivity. 87

4.8 Graphs of a specific portion of FMR measurement plotted as a function of external field ($\mathbf{H}_o$) for $S2$ and $S3$ on Z−line for fixed values of frequencies, where $\mathbf{a} = 4$ GHz, $\mathbf{b} = 4.5$ GHz, $\mathbf{c} = 5$ GHz and $\mathbf{d} = 5.5$ GHz. Solid lines are guide to the eyes. 88

4.9 Graph of a specific portion of FMR measurement plotted against the external field ($\mathbf{H}_o$) of $S4$ on Z−line for fixed values of frequencies, where $\mathbf{a} = 4$ GHz, $\mathbf{b} = 4.5$ GHz, $\mathbf{c} = 5$ GHz and $\mathbf{d} = 5.5$ GHz. Solid lines are guide to the eyes. 89

4.10 Graphs of a specific portion of FMR measurement plotted against external field ($\mathbf{H}_o$) for samples $S2$ and $S3$ in a) and b), respectively. Solid red line represents the resonant field of each peak at 6.5 GHZ. 90

4.11 Graph of a specific portion of FMR measurement plotted against the external field ($\mathbf{H}_o$) for $S4$ on Z−line for a fixed value of frequency. Red line represents the resonant field of the absorption peak. 91

4.12 Graphs of external field ($\mathbf{H}_o$) as a function of specific frequency ($\omega_o/2\pi$) for $S2$ and $S3$ in IP configuration are shown in a) and b). Solid lines are least square curve fit to the experimental data. The data is fit to Eq. (2.53) 91

4.13 Graph of external field ($\mathbf{H}_o$) as a function of specific frequency ($\omega_o/2\pi$) for $S4$ in IP configuration. Solid line is least square curve fit to the experimental data. 92

4.14 Graphs of resonant frequency ($\omega_o/2\pi$) plotted against the linewidth (FWHM) for $S2$ and $S3$ in IP configuration are shown in a) and b). Solid lines are least square curve fit to the experimental data. The data is fit against Eq. (3.18). 93

4.15 Graph of resonant frequency ($\omega_o/2\pi$) plotted against the linewidth (FWHM) for $S4$ in IP configuration. Solid lines are least square curve fit to the experimental data. The data is fit against Eq. (3.18). 93

A.1 Drawings of 58 mm SMA cable holders. All the dimensions are in millimeters. 103

A.2 Design of 58 mm SMA cable holders. 104

A.3 Front panel of FMR Setup visualized in LabView. The graphical VI's displays the output voltages from lock-in channels (X and Y), whereas the current tab controls the input current of power supply. 104

A.4 Block diagram of virtual elements of LabView program for FMR setup. Where **DAQ Assistant** = data acquisition, **loop iterations** controls the input current of power supply and **write to measurement** = element for storing data. 105

A.5 Graph of a specific portion of FMR measurement plotted against the resonant field ($\mathbf{H}_o$) for $S1$ on Z−line for fixed values of frequencies. 106

List of Tables

2.1 Demagnetization factors for some simple geometries with applied magnetic field in different directions. 37

3.1 Optimized parameters for magnetron sputtering of permalloy thin film samples. 53

3.2 Critical dimensions and characteristic impedance of CPWs and Z-shaped stripline. 60

3.3 Extracted VNA-FMR measurement parameters for IP configuration. 77

4.1 RF components along with the brand names. 84

4.2 Extracted lock-in FMR measurement parameters for IP configuration. 94

List of Abbreviations

CPW Coplanar Waveguide

D1 RF Power Detector-1

D2 RF Power Detector-2

dc Direct Current

DUT Device-under-test

FMR Ferromagnetic Resonance

IP In-Plane

L-MOKE Longitudinal Magneto Optical Kerr Effect

LI-FMR Lock-In Detection Ferromagnetic Resonance

LL Landau-Lifshitz

LLG Landau-Lifshitz-Gilbert

OOP Out-of-Plane

P-MOKE Polar Magneto Optical Kerr effect

PSD Phase-Sensitive Detection

RK Runge-Kutta

SOLT Short, Open, Load and Through

SOT Spin Orbit Torque

STT Spin Transfer Torque

VNA-FMR Vector Network Analyzer Ferromagnetic Resonance

Chapter 1

An Overview

The last few years have witnessed many research advances in investigating characteristics of magnetic materials [1, 2]. The growing interest is mainly due to the quest for smaller, faster and more sensitive magnetic systems: a common denominator to different technological applications in the field of spintronics [3], high density storage media [4], magnetic field sensors [5] and advanced microwave devices [6].

Magnetic materials are classified into two categories. The first class comprises materials which possess spontaneous magnetization and includes ferromagnetic, antiferromagnetic and ferrimagnetic materials [7]. The second class contains materials which are not spontaneously magnetized and includes diamagnetic and paramagnetic materials [8]. The presence of spontaneous magnetization is attributed to the exchange interaction among neighbouring spins which also carries over to large distances, leading to long range order. One important aspect of any magnetic material is magnetization dynamics which determines how the magnetization of a system responds, in time, to external stimuli such as magnetic fields and rf waves. Needless to say, the magnetization response of the medium is highly dependent on the microscopic magnetic properties. The study of these dynamics

are of great relevance for applications in both research and in the industry. To name a few, pertinent applications include microwave signal processing devices [9], memory logic devices [10], magnetic memory devices [11], magnetic sensors [12], magnetic tunnelling junctions (MTJ) [13] and giant magneto-resistive spin valves (GMR-SV) [14]. For example, the fast switching of MTJs are important for the development of non-volatile random access memories (MRAM) [15], whereas GMR-SV systems are used to fabricate ultra-sensitive hard disk drive read heads [16].

The study of magnetization dynamics is also crucial to the blossoming field of spintronics [17, 18] which employs the spin degree of freedom in lieu of the electron's charge. Spintronics has gathered immense attention because of its vast promise of commercial applications such as excitation of spin currents through temperature gradients [19], current pulses [20] etc. Ferromagnetic materials and their counterparts, antiferro and ferrimagnetic materials are of great interest for spintronics devices. Characterization of these materials is critical to understanding their suitability for use in spintronics devices. Some of the properties that are useful in this respect include static magnetic properties such as: anisotropies, phase transitions, exchange interactions, coupling interactions, spin-transfer torque and spin-orbit torque [21] and dynamic magnetic properties such as: damping, loss mechanisms, Landé g-factor and magnetic domain wall motion etc [22].

Advancing the argument further, there are several methods and techniques which have been employed throughout the literature to explore these dynamic properties. These techniques include MOKE [23], X-ray magnetic circular dichroism (XMCD) [24], VSM [25], AFMR [26] and FMR. In this work, we explore one of these techniques, namely, FMR.

Ferromagnetic resonance (FMR) is a versatile technique which probes in one go, both the static and dynamical properties of magnetic materials in the microwave frequency range. In essence, in FMR, a magnetic thin film is placed inside a dc magnetic field which initiates the presession of the magnetization vector [27]. Superimposing on this dc field, the absorption of a microwave field is measured. The variation of the absorption is registered with frequency or field, and the spectrum becomes a treasure house of useful information.

The current work aims to develop a better intuition of FMR along with the development of measuring techniques and the real construction of an experimental FMR system.We first outline how this thesis is organized. In Chapter 2, we start with preliminaries of dynamical motion of magnetization. The chapter is further organized as follows. Sections 2.1 and 2.2 describes the free precession of magnetization vector with the help of the Bloch equation. Section 2.3 present a theoretical background about the magnetization dynamics and how the Landau-Lifshitz-Gilbert (LLG) equation describes the time evolution of magnetization. Section 2.4 covers demagnetizing fields and the origin of magnetic anisotropies. Section 2.5 connects the susceptibility tensor with the LLG equation. In section 2.6, the geometry of thin films is described with the help of Kittel's equation which determines the resonant condition for the precessional motion, while incorporating magnetic anisotropies. Section 2.7 covers the effects of crystalline anisotropy on the FMR frequency. In section 2.8, the Smith-Beljers equation is also presented, which is a generalized tool for calculating the resonant condition for precessional frequency. The end goal of this chapter is to develop a strong theoretical background, so that later on, we can draw a comparison between experimental data and theoretical predictions.

Chapter 3 describes our experimental work and key results of VNA-FMR scheme.

It is our main body of work. It begins by providing details of sample fabrication, measurement techniques and experimental arrangements made for FMR measurements. Sections 3.1 and 3.2 describe how the samples were synthesized using magnetron sputtering and characterized in advance, by mageto-optic Kerr effect (MOKE) to determine the easy and the hard axes of magnetization. Sections 3.3 and 3.4 includes an introduction to the vector network analyzer (VNA) and fabrication of different coplanar waveguides (CPWs) and striplines. Finally, section 3.5 present measurement techniques and the experimental setup of VNA-FMR. Chapter 4 describes our experimental work and key results of LI-FMR scheme. We start with the basics of lock-in amplifier and testing of rf components. Section 4.1 present the basic underlying physics of lock-in amplifier. Section 4.2 covers testing of rf components and gives a brief overview of the experimental setup of LI-FMR scheme. Key results of FMR spectra obtained are interspersed in this thesis. We use these spectra to derive important static and dynamic magnetic characteristics of the thin film samples. Finally, we wrap up in Chapter 5.

Chapter 2

An Introduction to Broadband Ferromagnetic Resonance

Ferromagnetism and ferrimagnetism are characterized by materials possessing a spontaneous magnetization. This effect originates from the long-range alignment of atomic spins and magnetic moments [28] mediated by the exchange interaction. It is worth mentioning here that only electron's spin contribute to the FMR (nuclear contribution is negligible). In order to minimize energy [29] a ferromagnetic material morphologically splits into smaller regions, called domains. All of the spins are aligned parallel in each domain; however in the absence of a magnetic field, various domains can be sometimes oriented in random directions, rendering the overall sample in an unmagnetized form.

When an external magnetic field ($\mathbf{H}$) is applied to a ferromagnetic material the magnetization vector ($\mathbf{M}$) precessess around the field. Now, if a transverse rf microwave oscillating field is applied, so-called resonance may occur when the oscillating magnetic field matches with the precessional Larmor frequency (ω_o). This phenomenon is central to the technique of *ferromagnetic resonance*.

In the following pages, we gradually build up the mathematical and physical

framework that is necessary to describe FMR. Throughout this thesis, we consider that the precession frequency is uniform through the sample. This is called zero-mode FMR [30], typifying $\mathbf{k} = 0$ magnons (quanta of spin waves).

2.1 The Magnetic Moment

The idea of a magnetic dipole moment is central to understand magnetic forces and torques at the atomic level. In the early 1900s, detailed understanding of the origin of microscopic magnetic moment was explained by Heisenberg. Today, it's a well known fact that the strong interaction between neighboring atomic moments finds its origin in quantum mechanical exchange interaction between the spins [30]. The magnetic moment $\boldsymbol{\mu}$ of an electron in an atom is associated with the total angular momentum $\mathbf{J}$ and is given by

$$\boldsymbol{\mu} = -\gamma \mathbf{J}, \tag{2.1}$$

where $\gamma = eg/2m_e$ represents the gyromagnetic ratio of an electron, e is the charge and m_e its mass and $\mathbf{J}$ is the sum of orbital and spin angular momenta $\mathbf{J} = \mathbf{L} + \mathbf{S}$. For an electron g is called the Landé g-factor and has a value ≈ -2. For comparison, for a proton, $g \approx +5.586$.

The reason for the strong interaction between neighboring atomic moments is the overlapping of their orbital wave functions. Pauli exclusion principle states that the total wave function of a quantum mechanical system should be anti-symmetric [31]. Thus, for a quantum mechanical system, having two atoms i, j with spins $\mathbf{S}_i$ and $\mathbf{S}_j$ aligning parallel, have anti-symmetric wave function, whereas the wave function is symmetric if two spins align anti-parallel to each other. These two states have different electrostatic Coulomb energies because the symmetric and

anti-symmetric wave functions represents two different charge distributions. The difference between the energies of these two states is called Exchange energy and can be written as [32]

$$E_{exc} = -2J\mathbf{S}_i \cdot \mathbf{S}_j, \tag{2.2}$$

where J represents the exchange constant of the interaction and $\mathbf{S}_i$, $\mathbf{S}_j$ are the electronic spins of two atoms i and j, respectively. Eq. (2.2) is also called Heisenberg energy.

For ferromagnetic materials, J $>$ 0 which means the exchange energy will be minimum when two spins align parallel to each other. On the other hand, J $<$ 0 for antiferromagnetic materials in which the exchange energy will minimum when spins align anti-parallel to each other. Besides the exchange interaction, there are many other interactions like: long-range alignment of atomic spins and magnetic moments by magnetic-dipole interaction and interaction with external stimuli such as magnetic fields and rf waves through spin-orbit coupling (magnetic anisotropy energy). These interactions will be discussed in detail later in this chapter.

In the next section, we will discuss how the classical equations of electromagnetism govern the motion of magnetic moment in the presence of external magnetic field.

2.2 The Bloch Equation

In the presence of an external magnetic field, the energy of the magnetic moment for an infinite size magnetic material is given by

$$E = -\boldsymbol{\mu} \cdot \mathbf{B}. \tag{2.3}$$

Eq. (2.3) shows that the energy will be minimum when the magnetic moment is aligned with the external magnetic field. Consequentially, a torque will act whose form is

$$\boldsymbol{\tau} = \boldsymbol{\mu} \times \mathbf{B}. \tag{2.4}$$

The angular momentum $\mathbf{J}$ of magnetic moment is associated with with the torque and is given as

$$\boldsymbol{\tau} = d\mathbf{J}/dt. \tag{2.5}$$

Using Eqs. (2.1), (2.6) and (2.5) we can write

$$\frac{d\boldsymbol{\mu}}{dt} = -\gamma(\boldsymbol{\mu} \times \mathbf{B}). \tag{2.6}$$

For a magnetic system, the microscopic quantity $\boldsymbol{\mu}$ is replaced with a macroscopic magnetization vector $\mathbf{M}$ which is the sum of all magnetic moments per unit volume [33]. Hence, Eq. (2.6) takes the form

$$\frac{d\mathbf{M}}{dt} = -\gamma(\mathbf{M} \times \mu_{\mathrm{o}}\mathbf{H}). \tag{2.7}$$

Here we have replaced $\mathbf{B}$ by $\mu_{\mathrm{o}}\mathbf{H}$, where μ_{o} is the magnetic permeability and $\mathbf{H}$ represents the external magnetic filed. Eq. (2.7) is sometimes called the Bloch equation and describes the presessional motion of the magnetization vector in the absence of magnetic damping. In order to describe the motion of magnetic moment in rectangular coordinates, with external field applied in the z-direction

$\mathbf{H}(x, y, z) = H_o(0, 0, z)$, the magnetization takes the form

$$\mathbf{M} = M_{ox}\hat{i} + M_{oy}\hat{j} + M_s\hat{k}, \tag{2.8}$$

where M_s is the *saturation magnetization* and other two components M_{ox} and M_{oy} are small compared to the z-component of magnetization, $M_s \gg M_{ox}$ and M_{oy}. Using Eq. (2.8) we can decompose the Eq. (2.7) in rectangular components as

$$\frac{dM_{ox}}{dt} = -\gamma\mu_o M_y H_o, \tag{2.9}$$

$$\frac{dM_{oy}}{dt} = \gamma\mu_o M_x H_o, \tag{2.10}$$

$$\frac{dM_{oz}}{dt} = 0. \tag{2.11}$$

A solution of above Eqs. (2.9) and (2.10) can be written as

$$M_{ox} = m_o \cos\omega_o t, \tag{2.12}$$

$$M_{oy} = m_o \sin\omega_o t, \tag{2.13}$$

where m_o is the amplitude and ω_o is angular frequency of precession. By putting Eqs. (2.12) and (2.13) in Eqs. (2.9) and (2.10), respectively we get the angular frequency as

$$\omega_o = \gamma\mu_o H_o. \tag{2.14}$$

Eq. (2.14) is called the Larmor equation which describes that the *magnetic resonance frequency* (ω_o) is directly proportional the applied magnetic field H_o. Figure 2.1a illustrates an idealized situation of free precession in the absence of

magnetic damping. This picture contradicts the experimental observation where the magnetization vector **M** eventually aligns with the applied field. The correction term was introduced by Landau-Lifshitz and we discuss this in the next section.

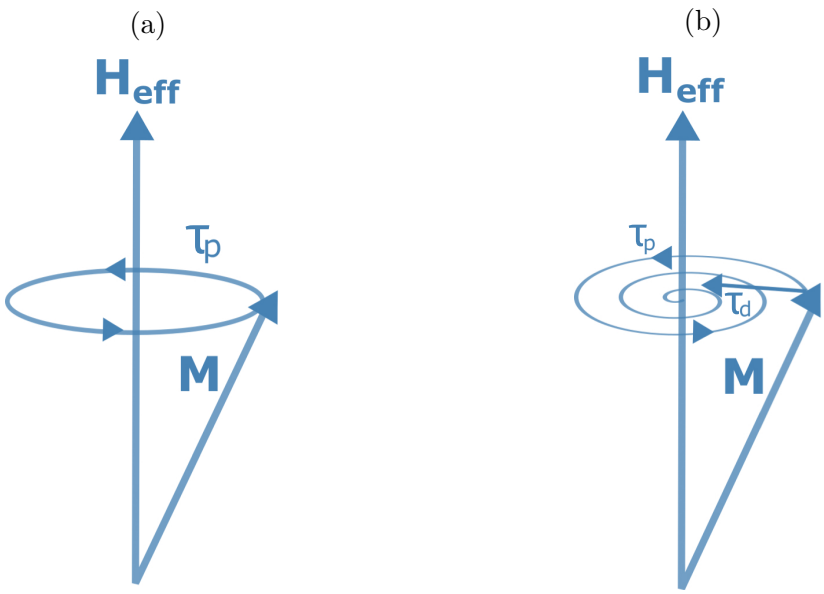

Figure 2.1: Magnetization dynamics in which the magnetization (**M**) is precessing around the effective magnetic field ($\mathbf{H}_{\text{eff}}$). In a) **M** is precessing around $\mathbf{H}_{\text{eff}}$ indefinitely under the action of precessional torque τ_P, whereas b) shows the damped precession of **M** around $\mathbf{H}_{\text{eff}}$, invoking the extra damping torque τ_D.

2.3 The Landau-Lifshitz-Gilbert Equation

The Landau-Lifshitz (LL) equation [34] shows the evolution of magnetization in space and time under the local effective field ($\mathbf{H}_{\text{eff}}(\mathbf{r}, t)$), and can be written as

$$\frac{d\mathbf{M}}{dt} = -\gamma^{'}(\mathbf{M} \times \mu_o \mathbf{H}_{\text{eff}}) - \frac{\lambda}{M_s^2}\big(\mathbf{M} \times (\mathbf{M} \times \mu_o \mathbf{H}_{\text{eff}})\big), \tag{2.15}$$

where $\gamma^{'} = \gamma/(1+\alpha^2)$, $\lambda = \gamma\alpha M_s/(1+\alpha^2)$, **M** is the magnetization vector and $\mathbf{H}_{\text{eff}}$ is is the combination of external and endogenous factors, as we explain later in this chapter. The first term, on the R.H.S. in Eq. (2.15) is similar to Eq. (2.7)

and is called precessional torque (τ_P), whereas the second term introduces a phenomenological additional torque perpendicular to the precessional torque, called the damping torque (τ_D), and brings back $\mathbf{M}$ to equilibrium as shown in Figure 2.1b. Eq. (2.15) was further modified by Gilbert, yielding the LLG equation as [35]

$$\frac{d\mathbf{M}}{dt} = -\gamma^{'}(\mathbf{M} \times \mathbf{H}_{\text{eff}}) - \frac{\gamma^{'}\alpha}{M_s}\big(\mathbf{M} \times (\mathbf{M} \times \mathbf{H}_{\text{eff}})\big). \tag{2.16}$$

In the preceding equation, α is the Gilbert's damping parameter and signifies the rate at which $\mathbf{M}$ returns to equilibrium. Its value typically lies in the range $\alpha = 0.005$ to 0.1. For $\alpha = 0$, Eq. (2.16) reduces to the Bloch equation and predicts that $\mathbf{M}$ will precess indefinitely around $\mathbf{H}_{\text{eff}}$, never aligning parallel to $\mathbf{H}_{\text{eff}}$. However, for $\alpha \neq 0$, $\mathbf{M}$ precesses around $\mathbf{H}_{\text{eff}}$ with an angle that is exponentially attenuated ($e^{-\alpha t}$). The behavior is simulated in Figure 2.2.

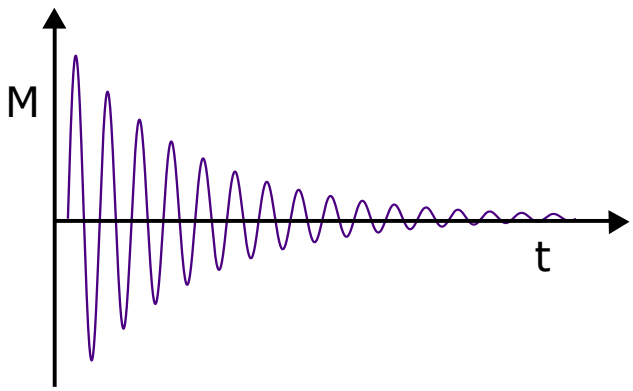

Figure 2.2: Attenuated magnetization precession around the effective magnetic field for $\alpha > 0$.

The general solutions for the linearized LLG equation are called spin waves that corresponds to the propagation of deviations of the spin alignment from equilibrium. Spin waves harbor information about the underlying magnetic systems such as: the anisotropy energy, external magnetic field, demagnetization effects and

saturation magnetization ($\mathbf{M}_\mathrm{s}$) [34]. In quantized form, they are called magnons (quanta of spin waves) [30].

Spin waves can be detected and measured by FMR, especially the isotropic ($\mathbf{K} = 0$) modes. For an external magnetic field applied in the z-direction $\mathbf{H}(x, y, z) = H_\mathrm{z}(0, 0, z)$ Eq. (2.16) can be decomposed in rectangular components [36] yielding,

$$\frac{dM_x}{dt} = -\frac{\gamma_o}{(1+\alpha^2)}(M_y H_z) - \frac{\gamma_o \alpha}{M_s(1+\alpha^2)}(M_x M_z H_z), \tag{2.17}$$

$$\frac{dM_y}{dt} = \frac{\gamma_o}{(1+\alpha^2)}(M_x H_z) - \frac{\gamma_o \alpha}{M_s(1+\alpha^2)}(M_y M_z H_z), \tag{2.18}$$

$$\frac{dM_z}{dt} = \frac{\gamma_o \alpha}{M_s(1+\alpha^2)} H_z (M_x^2 + M_y^2). \tag{2.19}$$

Eqs. (2.17), (2.18) and (2.19) are non-linear coupled differential equations which can be solved by, for example, the Runge-Kutta (RK) method. The simulated results for different damping parameters and initial conditions are shown in Figure 2.3.

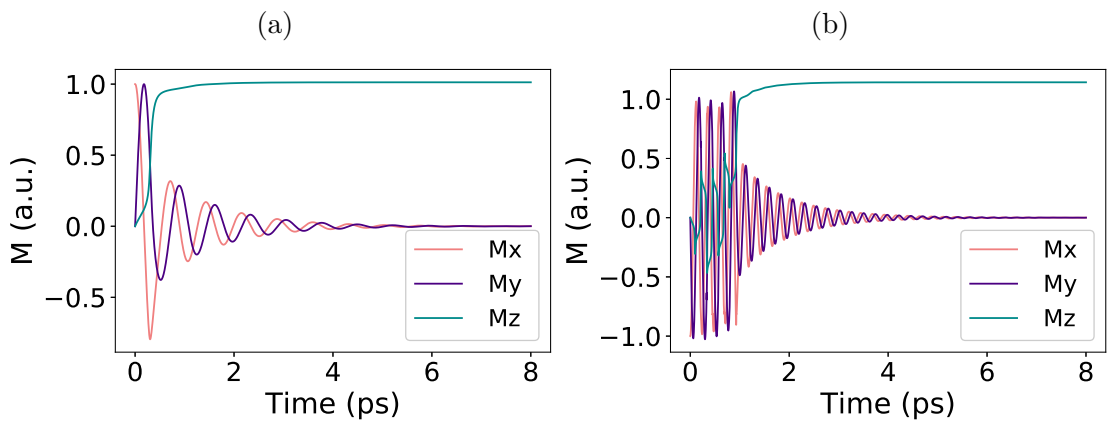

Figure 2.3: Time evolution of different components of magnetization ($\mathbf{M}$) for different damping constants under different initial conditions. In a) $\alpha = 0.1$, $\mathrm{H}_z = 5$ T and $\mathbf{M}_\mathrm{o} = (1, 0, 0)$ and b) $\alpha = 0.05$, $\mathrm{H}_z = 15$ T and $\mathbf{M}_\mathrm{o} = (1, 0, 0)$. Here $\mathbf{M}_\mathrm{o}$ represents the initial magnetization vector.

Figure 2.3 shows the time evolution of magnetization under different initial-conditions for lightly and heavily damped systems, respectively. It also gives information about the time taken by both systems to align in the direction of applied magnetic field.

The presence of spontaneous magnetization in ferro and ferrimagnetic materials can be explained by the intrinsic field generated inside a magnetic material. This in turn requires a careful differentiation between the effective magnetic field ($\mathbf{H}_{\text{eff}}$), applied magnetic field ($\mathbf{H}_{\text{app}}$) and demagnetizing field ($\mathbf{H}_{\text{d}}$) as we discuss in the next section.

2.4 Effects of Demagnetizing Fields

In ferro and ferrimagnetic materials, the magnetic resonance frequency strongly depends on the shape of sample. Its because of the long-range alignment of atomic spins and magnetic moments by magnetic-dipole interaction which in turn produces *demagnetizing* field on the surface of the sample. There are two other interactions which effects the resonance frequency of FMR, namely, exchange interaction and crystalline anisotropy energy. We start initially with the exchange interaction and then the demagnetizing field. The effects of crystalline anisotropy on the FMR frequency will be discussed later in this chapter.

If we consider a sample with uniform mode of precession frequency, magnetization is uniform so that all spins are parallel to each other. In this case, using Eqs. (2.1) and (2.3), we can rewrite the exchange energy of magnetic moment as

$$E = -\boldsymbol{\mu} \cdot \mu_o \mathbf{H}, \tag{2.20}$$

where $\mathbf{H}$ is the external magnetic field, proportional to the magnetization vector $\mathbf{M}$. Since, the free precesional motion is governed by Bloch equation (2.7), and $(\mathbf{M} \times \mu_{\mathrm{o}}\mathbf{H} = 0)$. Which means that the exchange interaction does not effect the frequency of uniform mode FMR, therefore we will ignore the effects of exchange interaction on the FMR frequency in the forthcoming sections.

If we place a ferromagnetic material (ellipsoid shaped) under an external magnetic field ($\mathbf{H}_{\mathrm{app}}$), the discontinuity of magnetization between the surface and the interfaces of sample gives rise to magnetic dipoles which in return creates a demagnetizing field ($\mathbf{H}_{\mathrm{d}}$). The demagnetizing field affects the resonance frequency of FMR and also changes the effective field ($\mathbf{H}_{\mathrm{eff}}$) as

$$\mathbf{H}_{\mathrm{eff}} = \mathbf{H}_{\mathrm{app}} + N_d\mathbf{M}, \tag{2.21}$$

where N_d is tensor in nature and represents the demagnetizing factor which depends on the shape of the magnetic medium and direction of applied field [33]. The additional term in the above equation is the demagnetizing field, i.e., $\mathbf{H}_{\mathrm{d}} = -N_d\mathbf{M}$ which plays an important role in determining the magnetization state of ferromagnetic materials.

Table 2.1: Demagnetization factors for some simple geometries with applied magnetic field in different directions.

Shape of Sample	**Direction of Magnetization**	N_x	N_y	N_z
Sphere	In-plane	1/3	1/3	1/3
Thin plate	Out-of-plane	0	0	1
Thin plate	In-plane	0	1	0

In rectangular coordinate system, N_d tensor is diagonal with components N_x, N_y and N_z. As shown in Table 2.1, for different shapes of samples, demagnetization factors are also different.

In the next section, we'll discuss how magnetization changes under external magnetic field and an additional rf field and how magnetization precession create time varying demagnetizing fields in particular directions.

2.5 Susceptibility Tensor

The magnetic properties of any material are defined in terms of a response under the application of an external stimuli which is a magnetic field. The ratio conceptually expressed through the constitutive relationship $\mathbf{M} = \chi\mathbf{H}$ is called susceptibility. Note that working in SI units, $\mathbf{M}$ and $\mathbf{H}$ have the same dimensions so the susceptibility (χ) is a dimensionless quantity.

For diamagnetic, paramagnetic and antiferromagnetic materials, magnetization disappears if the external magnetic field is removed. However, for ferromagnetic and ferrimagnetic materials, magnetization maybe retain the material even in the absence of external field for which we have used the term spontaneous magnetization. For ferromagnetic materials, susceptibility is a function of applied field and has a large positive value ($\chi \gg 1$) [37], whereas for paramagnetic and diamagnetic materials, χ is small (close to zero).

The susceptibility, in general is a tensor. Furthermore, for these materials the resonance condition can be encapsulated in the form of the susceptibility term ($\chi > 1$) and ($\chi < 1$), respectively. By introducing a small ac signal which produces a small oscillating magnetic field the LLG equation (2.16) can be solved and the susceptibility tensor is subsequently derived [38]. For this purpose, let's define oscillating magnetization vector $\mathbf{M}$ in the following form

$$\mathbf{M} = M_{ox}e^{i\omega t}\hat{i} + M_{oy}e^{i\omega t}\hat{j} + M_s e^{i\omega t}\hat{k}, \tag{2.22}$$

where M_{ox}, M_{oy} and $M_s \approx M_{oz}$ are x-, y- and z-components of magnetization vector, respectively. By applying an external magnetic filed in the z-direction and on top of it superimposing a perpendicular oscillating magnetic field, $\mathbf{H}_{\text{app}}$ and $\mathbf{H}_{\text{d}}$ can be rewritten as

$$\mathbf{H_{app}} = \mathbf{h_t} + H_o\hat{k}, \tag{2.23}$$

$$\mathbf{H_d} = (N_x M_x + N_y M_y + N_z M_{oz})e^{i\omega t}. \tag{2.24}$$

In the above equation, $\mathbf{h}_{\text{t}}$ is the small oscillating magnetic field, i.e., $\mathbf{h}_{\text{t}} = H_{ox}e^{i\omega t}\hat{i} + H_{oy}e^{i\omega t}\hat{j}$. By putting Eqs. (2.23) and (2.24) in Eq. (2.21), the effective field $\mathbf{H}_{\text{eff}}$ can be decomposed in x-,y- and z-components as

$$\begin{aligned} H_x &= (H_{ox} - N_x M_x)e^{i\omega t}, \\ H_y &= (H_{oy} - N_y M_y)e^{i\omega t}, \\ H_z &= (H_o - N_z M_{oz})e^{i\omega t}. \end{aligned} \tag{2.25}$$

By using Eq. (2.22) in conjunction with Eq. (2.25) and suppressing the exponential terms reduces the Eq. (2.16) to

$$\frac{d\mathbf{M}}{dt} = \hat{i}(-\omega_y M_y + \gamma H_{oy} M_{oz}) + \hat{j}(\omega_x M_x - \gamma H_{ox} M_{oz}), \tag{2.26}$$

where $\omega_x = \gamma\mu_o H_x$ and $\omega_y = \gamma\mu_o H_y$. By taking $N_x = N_y = N_z$, $\omega_x = \omega_y = \omega_o = \gamma\mu_o H_o$ and $\omega_m = \gamma\mu_o M_{oz}$ the above equation can be decomposed into rectangular components as

$$\frac{dM_x}{dt} = -\omega_o M_y + \omega_m H_y, \tag{2.27}$$

$$\frac{dM_y}{dt} = \omega_o M_x - \omega_m H_x, \tag{2.28}$$

$$\frac{dM_{oz}}{dt} = 0. \tag{2.29}$$

In the above equation, $dM_{oz}/dt = 0$ because $M_{oz}H_z \gg M_xH_y$ and M_xH_y. Eqs. (2.27) and (2.28) are coupled differential equations and can be solved to get the transverse components of magnetization as [39]

$$M_x = \frac{\omega_o\omega_m}{(\omega_o^2 - \omega^2)}H_x + i\frac{\omega\omega_m}{(\omega_o^2 - \omega^2)}H_y, \tag{2.30}$$

$$M_y = \frac{\omega_o\omega_m}{(\omega_o^2 - \omega^2)}H_y - i\frac{\omega\omega_m}{(\omega_o^2 - \omega^2)}H_x. \tag{2.31}$$

These are the equations of motions for magnetic dipoles under forced precessions. The magnetization has a linear relationship with magnetic filed as $\mathbf{M} = \chi\mathbf{H}$, where susceptibility ($\chi$) can be written in tensor form as

$$\mathbf{M} = \begin{pmatrix} \chi_{xx} & \chi_{xy} & 0 \\ \chi_{yx} & \chi_{yy} & 0 \\ 0 & 0 & 0 \end{pmatrix} \mathbf{H}. \tag{2.32}$$

By comparing Eq. (2.32) with Eqs. (2.30) and (2.31), we get the susceptibilities as

$$\chi_{xx} = \chi_{yy} = \frac{\omega_o\omega_m}{(\omega_o^2 - \omega^2)}, \tag{2.33}$$

$$\chi_{xy} = -\chi_{yx} = i\frac{\omega\omega_m}{(\omega_o^2 - \omega^2)}. \tag{2.34}$$

The above two Eqs. (2.33) and (2.34) describes how the amplitude of magnetization increases rapidly as forced precessional frequency (ω) approaches the Larmor frequency (ω_o). These two equations also diverge at $\omega = \omega_o$ which is a non-physical phenomena, called *gyromagnetic resonance*, showing the importance of considering relaxation and damping. Now, the loss can be accounted for by assuming $\omega_o \to \omega_o + i\alpha\omega$ in Eqs. (2.33) and (2.34) making the susceptibilities

complex as

$$\chi_{xx} = \chi_{xx}^{'} - \iota\chi_{xx}^{''}, \tag{2.35}$$

$$\chi_{xy} = \chi_{xy}^{''} + \iota\chi_{xy}^{'}. \tag{2.36}$$

The above equations reveal that if we apply the oscillating magnetic field either in the x- or y-direction, $\mathbf{M}$ will be produced in both directions (because $\mathbf{M}$ is precessing around the z-axis). Thus, the precessional motion of magnetization vector with frequency (ω) is associated with its x- and y- components through Eqs. (2.30) and (2.31). That's why the relation between $\mathbf{M}$ and $\mathbf{H}$ is tensorial and not a scalar relation. Thus, the real and imaginary parts of Eqs. (2.35) and (2.36) are given as

$$\chi_{xx}^{'} = \frac{\omega_o\omega_m(\omega_o^2 - \omega^2) + \omega_o\omega_m\omega^2\alpha^2}{\left[\omega_o^2 - \omega^2(1+\alpha^2)\right]^2 + 4\omega_o^2\omega^2\alpha^2}, \tag{2.37}$$

$$\chi_{xx}^{''} = \frac{\alpha\omega\omega_m\left[\omega_o^2 + \omega^2(1+\alpha^2)\right]}{\left[\omega_o^2 - \omega^2(1+\alpha^2)\right]^2 + 4\omega_o^2\omega^2\alpha^2}, \tag{2.38}$$

$$\chi_{xy}^{'} = \frac{\omega\omega_m\left[\omega_o^2 - \omega^2(1+\alpha^2)\right]}{\left[\omega_o^2 - \omega^2(1+\alpha^2)\right]^2 + 4\omega_o^2\omega^2\alpha^2}, \tag{2.39}$$

$$\chi_{xy}^{''} = \frac{2\omega_o\omega_m\omega^2\alpha}{\left[\omega_o^2 - \omega^2(1+\alpha^2)\right]^2 + 4\omega_o^2\omega^2\alpha^2}. \tag{2.40}$$

Note that the real part of susceptibility describes a Lorentzian shape absorption peak and imaginary part is the first derivative of this Lorentzian function. The measurement techniques we've developed in this work are sensitive to both amplitude and phase, therefore the real and imaginary parts of susceptibility can be measured using above equations. The simulated results of above Eqs. (2.37–2.40) are shown in Figure 2.4.

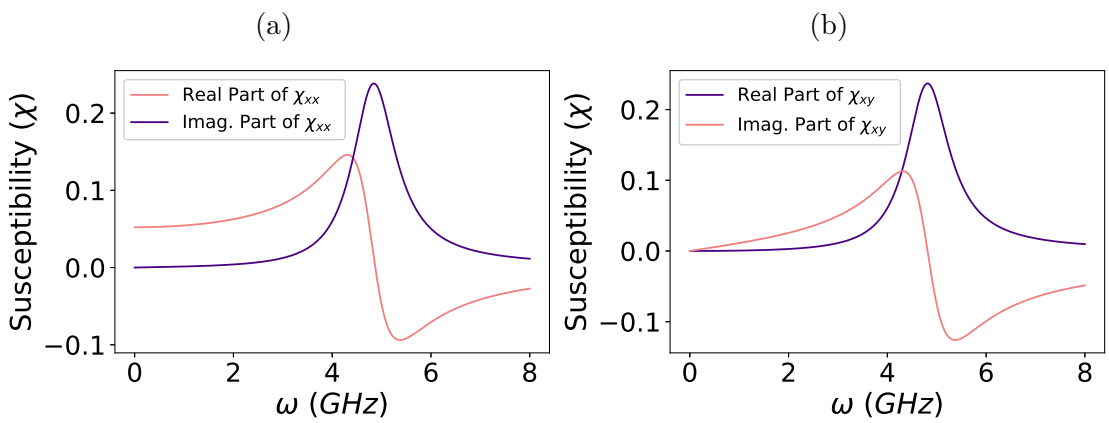

Figure 2.4: Graphs of real and imaginary parts of complex susceptibility tensor as a function of resonance frequency (ω_o) for a fixed value of magnetic field. In a) the real and imaginary parts of χ_{xx} are shown, whereas b) shows the real and imaginary parts χ_{xy}.

In the next section, we'll discuss some standard analytic results in order to understand the connection between applied magnetic field and resonance frequency. This connection is well describe by Kittel's equation, which is the condition of resonance frequency for uniform mode excitation in ferromagnetic materials.

2.6 Kittel's Equation

For a cubic ferromagnetic material placed inside an external magnetic field applied in the z-direction $\mathbf{H}_{\text{eff}}(x, y, z) = H_o(0, 0, z)$, Eq. (2.21) reduces to

$$H_x = -N_x M_x, \tag{2.41}$$

$$H_y = -N_y M_y, \tag{2.42}$$

$$H_z = H_o - N_z M_o. \tag{2.43}$$

Note that the demagnetization factors relate the applied and demagnetizing rf fields near the surface of ferromagnetic sample. Using Eqs. (2.8), (2.41), (2.42)

and (2.43) in Eq. (2.7) we get the equations of motion for the x-, y- and z-components of transverse magnetization as

$$\frac{\partial M_x}{\partial t} = \gamma\mu_o(H_y M_o - H_z M_y), \tag{2.44}$$
$$\frac{\partial M_y}{\partial t} = \gamma\mu_o(H_z M_x - H_x M_o), \tag{2.45}$$
$$\frac{\partial M_o}{\partial t} = \gamma\mu_o(H_x M_y - H_y M_x). \tag{2.46}$$

By considering the demagnetization factors and ignoring the MH product, above equations reduces to.

$$\frac{\partial M_x}{\partial t} = \gamma\mu_o\big((N_z - N_y)M_o - H_o\big)M_y, \tag{2.47}$$
$$\frac{\partial M_y}{\partial t} = \gamma\mu_o\big(H_o + (N_x - N_z)M_o\big)M_x, \tag{2.48}$$
$$\frac{\partial M_o}{\partial t} = 0, \tag{2.49}$$

The solutions of above Eqs. (2.47) and (2.48) has the same form as in Eqs. (2.12) and Eqs. (2.13). Hence, the resonance frequency becomes

$$\omega_o^2 = \gamma^2 {\mu_o}^2\Big(H_o + \big(N_y - N_z\big)M_o\Big)\Big(H_o + \big(N_x - N_z\big)M_o\Big), \tag{2.50}$$

where ω_o is known as the frequency of uniform mode FMR. The above Eq. (2.50) is known as Kittel's equation [40] which tells that the resonant FMR frequency depends on the demagnetization factors (shape of ferromagnetic material) and the the direction of applied magnetic field.

At this juncture, we would like to extend our discussion to some special case results and its validity for ferromagnetic thin films. It is worthwhile to compare the resonance frequencies for three different geometries like the sphere, thin plate

with OOP magnetization and thin plate with IP magnetization, given by

$$\omega_o^{sphere} = \gamma\mu_o H_o, \tag{2.51}$$

$$\omega_o^{IP} = \gamma\mu_o(H_o - M_o), \tag{2.52}$$

$$\omega_o^{OOP} = \gamma\mu_o\big(H_o(H_o + M_o)\big)^{1/2}. \tag{2.53}$$

The above three equations (2.51–2.53) are obtained by taking the demagnetization factors mentioned in the Table 2.1. The typical simulated results for the resonant FMR frequency as a function of applied magnetic field using above mentioned geometries are shown in Figure 2.5. Notice that the FMR frequency in case of a sphere and thin film with IP magnetization goes to zero as the applied magnetic field goes to zero. In contrast, the resonance frequency of a thin film with OOP magnetization remains very high even in the absence of external magnetic field which can be very useful in designing high frequency signal processing devices [41].

At this moment, we would like to introduce magnetic anisotropy which is a significant parameter in investigation of magnetic materials. Magnetic anisotropy arises due to the system's tendency to align in a preferred direction (easy axis) to hard axis. This deviation adds an additional energy consideration into the system—magnetic anisotropy energy.

2.7 Effects of Crystalline Anisotropy Energy

In this section, we will discuss one factor which greatly affects the hysteresis curve or magnetic properties of a system, is magnetic anisotropy. This interaction has not been considered previously. In summary, it tells us that the magnetic properties of a system depend on the preferred direction in which they are measured

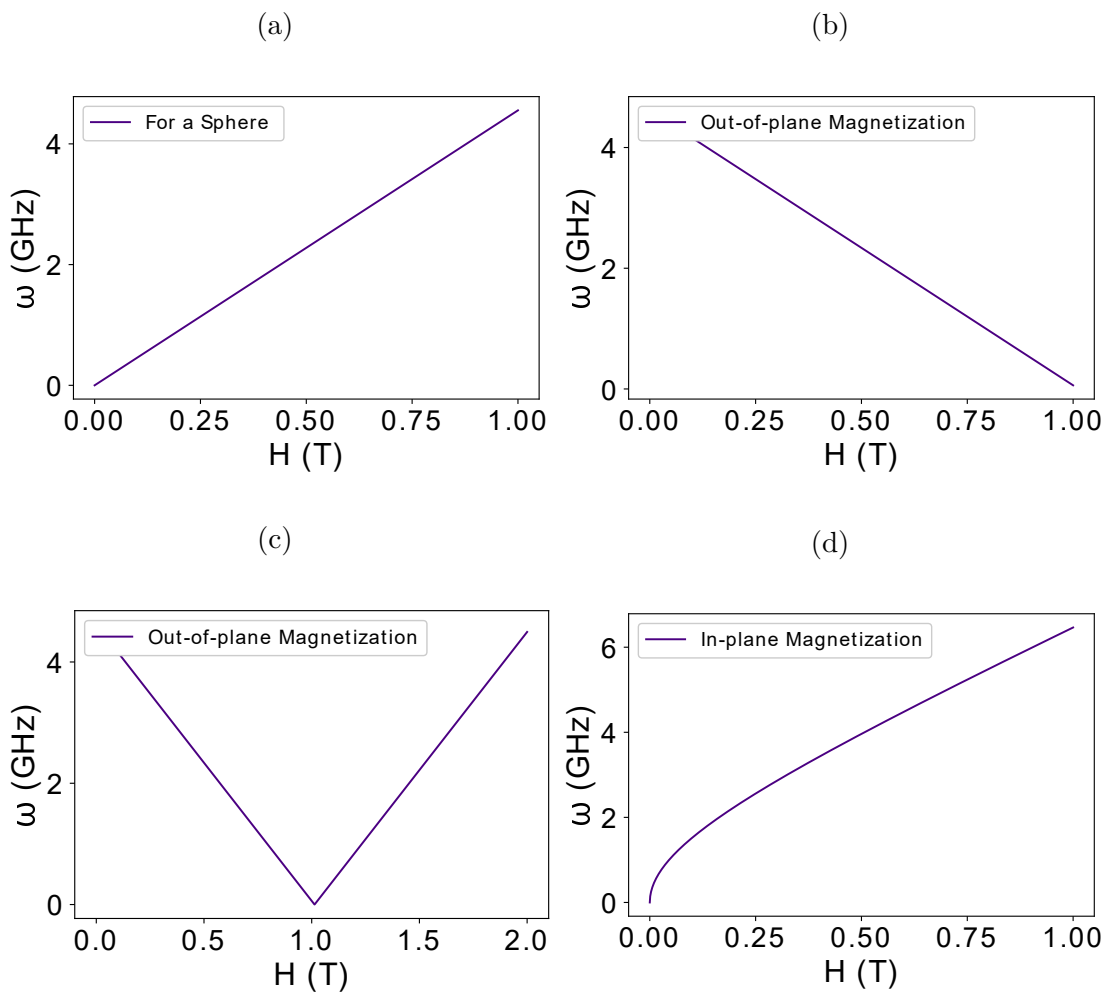

Figure 2.5: Graphs of resonant FMR frequency (ω_o) as a function of external magnetic field ($\mathbf{H_o}$) for a ferromagnetic material. In a) the resonant condition for a spherical geometry is shown, b) shows the resonant condition for a thin film with OOP magnetization $< \mathrm{H_a}$, c) shows the resonant condition for a thin film with OOP magnetization $> \mathrm{H_a}$ and d) presents the resonant condition for a thin film with IP magnetization. Here $\mathrm{H_a}$ represents the anisotropy field.

[33]. Magnetic anisotropy finds its origin in the spin-orbit coupling—interaction between electronic spins and orbital angular momentum [37].

Magnetic anisotropy strongly affect the magnetization dynamics in ferromagnetic materials and can be studied using the expression for anisotropy energy. For a cubic crystal in which there are many equivalent preferred directions, the crys-

talline anisotropy energy density is defined as the energy per unit volume between magnetization along the easy and the hard axes and can be written as [42]

$$E = K_o + K_1(\alpha_1^2\alpha_2^2 + \alpha_2^2\alpha_3^2 + \alpha_3^2\alpha_1^2) + K_2(\alpha_1^2\alpha_2^2\alpha_3^2), \tag{2.54}$$

where K_0, K_1 and K_2 are anisotropy constants and α_1, α_2 and α_3 are the direction cosines which $\mathbf{M}$ makes relative to the crystal axes [100], [010] and [001], respectively. In Eq. (2.54) the higher order terms $(K_3, K_4, \ldots)$ are ignored. For $K_2 = 0$, the direction of easy axis of magnetization can be determined by the sign of K_1. If $K_1 > 0$ then anisotropy energy in the $\langle 111 \rangle$ direction (E_{111}) will be maximum and $\langle 100 \rangle$ will be the easy axis of magnetization. If $K_1 < 0$ then anisotropy energy in the $\langle 100 \rangle$ direction (E_{100}) will be maximun and $\langle 111 \rangle$ will be the hard axis of magnetization.

In ferromagnetic materials the direction of magnetic moment changes according to the symmetry of lattice. This deviation of magnetic moment gives rise to *crystalline anisotropy* energy which can be defined as the indignation of magnetization to align in a preferable crystallographic direction under the application of an external magnetic field.

In angle dependent FMR measurements, the resonance frequency or field is a function of angle between magnetization and the easy axis of local anisotropy energy [43], as we discuss in the next section which also gives information about the magnetic anisotropy of a ferromagnetic system. In this case, the uniaxial anisotropy energy is given by [44]

$$E_{crystal} = -K_{\mathrm{eff}} \cos^2\theta, \tag{2.55}$$

where K_{eff} is the effective uniaxial (out-of-plane) anisotropy energy the expression for which can be written as

$$K_{\text{eff}} = K_u - \frac{1}{2}(N_z - N_x)M_s^2. \tag{2.56}$$

By using Eq. (2.56) in conjunction with Eq. (2.55), expression for uniaxial magneto crystalline anisotropy becomes [43]

$$E_{crystal} = -K_u \cos^2\theta + \frac{1}{2}(N_z - N_x)M_s^2 cos^2\theta. \tag{2.57}$$

In the above equation, N_x, N_y and N_z are the demagnetization factors along the axes of magnetic material and K_u is some additional second-order uniaxial anisotropy.

In the next section, we present the derivation of a general equation to calculate the resonance frequency of a ferromagnetic material with various interactions and for different directions of applied magnetic field. The equation is useful to calculate the resonant condition including the effects of crystalline anisotropy on the FMR frequency.

2.8 Smit-Beljers Equation

The effects of crystalline and shape anisotropy energy on the resonance frequency of FMR can be calculated by taking a spherical shape ferromagnetic material and writing $\mathbf{M}$ and $\mathbf{H}_{\text{eff}}$ in spherical coordinates as

$$\mathbf{M} = m(\hat{r}, \hat{\theta}, \hat{\phi}), \tag{2.58}$$

$$\mathbf{H}_{\text{eff}} = (H_r\hat{r}, H_\theta\hat{\theta}, H_\phi\hat{\phi}), \tag{2.59}$$

where the magnetization is along $\hat{r}$ so we can take $\mathbf{M} = m(\hat{r})$. We can find H_θ and H_ϕ by considering a change in the energy of dipole with a infinitesimal rotation as shown in Figure 2.6.

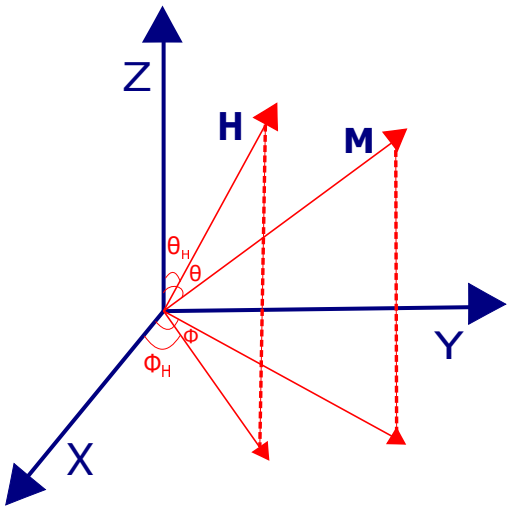

Figure 2.6: Sample geometry of equilibrium magnetization and applied magnetic field.

By taking rotation along the polar angle θ which is discussed in detail in Appendix A.1. The energy of magnetic moment ($\mathbf{m}$) in the presence of magnetic field ($\mathbf{H}_{\text{eff}}$) can be written as

$$E = -\mathbf{m} \cdot \mathbf{H}_{\text{eff}}. \tag{2.60}$$

Now, if we put the values of $\mathbf{m}$ and $\mathbf{H}_{\text{eff}}$ from Eq. (A.9) and (2.59), respectively in Eq. (2.60) and then take rotation along θ and ϕ we get

$$H_\theta = \frac{-1}{m}\frac{\partial E}{\partial \theta}, \tag{2.61}$$

$$H_\phi = \frac{-1}{m \sin\theta}\frac{\partial E}{\partial \phi}, \tag{2.62}$$

$$0 = \frac{\partial M_r}{\partial t}. \tag{2.63}$$

If we put Eqs. (2.61) and (2.62) in Eq. (2.59) and solve for Eq. (2.7), we get

$$\frac{\partial E}{\partial \phi} = \frac{M \sin\theta\dot{\theta}}{\gamma}, \tag{2.64}$$

$$\frac{\partial E}{\partial \theta} = \frac{-M \sin\theta\dot{\phi}}{\gamma}. \tag{2.65}$$

By solving Eqs. (2.64) and (2.65) and ignoring the higher order terms we get

$$\omega^2 = \frac{\gamma^2}{M^2 \sin^2\theta_o}\left[\frac{\partial^2 E}{\partial \theta^2}\frac{\partial^2 E}{\partial \phi^2}\left(\frac{\partial^2 E}{\partial \theta \phi}\right)^2\right] \tag{2.66}$$

where E is the total magnetic energy of a ferromagnetic material. Eq. (2.66) is called the Smit-Beljers equation, which is is an alternate tool for calculating the resonance frequency in different configurations of a ferromagnetic material.

2.9 Concluding Remarks

In this chapter, we briefly discussed the fundamentals of dynamical motion of magnetization. To set the stage for ferromagnetic resonance in magnetic thin, films which is the main focus of this thesis, we started with the Landau-Lifshitz-Gilbert (LLG) equation. We found that the key role player in magnetization dynamics is the spins of the electrons. We then connected the LLG equation to the susceptibility tensor. We finally derived Kittel's equation which determines the resonant condition for the precessional motion incorporating the magnetic anisotropies in case of ferromagnetic materials. In the next chapter, we'll discuss the experimental setups and measurement techniques we developed. We'll use two different techniques to get FMR spectra of permalloy thin film samples.

Chapter 3

VNA Based Experimental Setups and Measurement Techniques for FMR

Today, many studies focus on the magnetic properties of nanoparticles, nanostructured materials, thin and ultra thin films [45]. One commonality between these novel materials is the phenomenon of magnetic resonance. It forms the basis for nuclear magnetic resonance (NMR) [46], nuclear quadrupole resonance (NQR) [47], electron spin resonance (ESR) [48], electron paramagnetic resonance (EPR) [49], spin wave resonance (SWR) [50] and ferromagnetic resonance (FMR). In this chapter, we'll discuss the basic underlying principles of an experimental FMR system along with the different experimental setups developed in this work. We'll also illustrate the advantages of an FMR system for probing the magnetic properties of ferromagnetic thin films, in our case permalloy thin films. Two techniques were developed for the FMR measurements of thin film samples which use a vector network analyzer (VNA) and phase-sensitive lock-in detection (LI).

In this chapter, we'll discuss the VNA-FMR which is a fast but less sensitive technique because it measures the FMR response of the device-under-test (DUT). In literature, VNA-FMR is used with a frequency sweep, whereas LI-FMR generally implies a field swept response of the magnetic sample, as we see later in Chapter 4. In principle, both techniques can be delivered in either frequency or field swept modes.

In FMR, for commonly applied fields, radiation absorption occurs in the microwave range and for that purpose we need a microwave excitation source, a detector and a coplanar waveguide (CPW) or stripline (which connects our sample to the microwave source). The CPW and stripline will be defined shortly. Either of VNA or LI-FMR measures the diagonal terms of the complex susceptibility tensor, Eqs. (2.37–2.40).

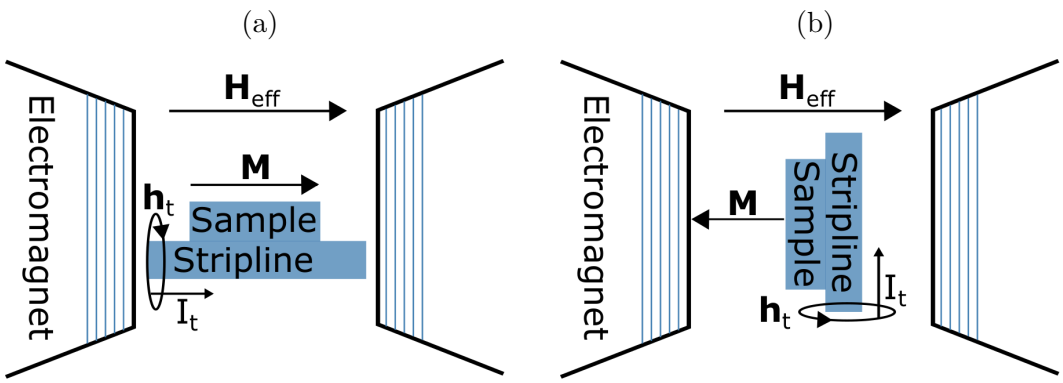

Figure 3.1: In-plane and out-of-plane configurations of an FMR system. In a) in-plane configuration is shown with magnetization parallel to applied magnetic field, whereas b) shows the out-of-plane configuration with magnetization perpendicular to applied magnetic field.

The FMR response of a sample is obtained by applying an external static magnetic field in-plane (IP) or out-of-plane (OOP) to the sample which is placed on a CPW or stripline and absorbs energy from the microwave source. The two geometries are shown in Figure 3.1. A detector then records the change in transmitted (absorbed) microwave energy by sweeping the frequency or field.

Before discussing the VNA-FMR technique in detail we need to discuss how thin film samples were synthesized and characterized. The chapter is organized by discussing sample preparation followed by some morphological measurements and supplementary detection using the technique of magneto-optic Kerr effect (MOKE). We then go into the specifics of VNA-FMR, explaining the setup we built and present the data acquired from a systematic protocol of measurement on this system. Finally, we extract useful parameters and interpret the physics.

3.1 Thin Film Deposition

Sputtering is a physical vapor deposition technique in which the desired material is ejected from the target by the impact of high energy particles [51]. The ejected atoms then deposit on the surface of substrate. For the deposition of our thin film samples, we have specifically used the technique of *magnetron sputtering*.
In magnetron sputtering, electric and magnetic fields are applied between the target and the substrate placed inside a vacuum chamber. Once the desired vacuum has been achieved, a small amount of argon gas is introduced into the vacuum chamber. The electric field ionises the argon atoms, causing them to accelerate towards the negatively biased target. Because of atomic collisions, atoms and electrons are ejected from the target. Some of these ejected target atoms condense on the surface of the substrate forming a thin film of the desired material. The ejected electrons are maneuvered near the surface of the substrate by means of a magnetic field which increases the ionisation rate of argon gas and therefore increases the sputter rate. The electric field can be dc or rf, rendering the names dc and rf magnetron sputtering.
The magnetic thin film samples we used during the course of this work were deposited using a magnetron sputtering unit (VTS KOREA DaoN 1000s) which

is equipped with two dc power supplies and a single rf supply. To have a fine deposition of good quality thin films, cleaning of the substrate is an essential pre-requisite. The substrate was first dipped in acetone and then placed in an ultrasonic bath for 15 minutes. This process was followed with iso-propanol and then with distilled water. For the deposition of permalloy ($Ni_{80}Fe_{20}$) thin film samples with varying thicknesses on a silicon substrate the operating parameters for the sputtering unit were set according to Table 3.1.

Table 3.1: Optimized parameters for magnetron sputtering of permalloy thin film samples.

Parameters	**Optimized values**
Base pressure	1.0×10^{-6} Torr
RF power	100 Watt
Ar pressure	4.8×10^{-3} Torr
Ar flow rate	50 sccm
Substrate temperature	298 K
Target to substrate distance	7 cm

In total we synthesized various thin films of permalloy with different thicknesses. However, for purpose of demontration in this work, we will demonstrate FMR measurements with four samples prepared by the courtesy of Shahbaz Ahmad from the University of Western Australia Sydney: 20 nm ($S1$), 49 nm ($S2$), 72 nm ($S3$) and 100 nm ($S4$). As a confirmatory step, the magnetic response of the deposited thin film was measured by magneto-optic Kerr effect (MOKE) which is a non-contact, remote magnetization probing technique.

3.2 Magneto-optic Kerr Effect

The magneto-optical Kerr effect (MOKE) has been widely used to investigate magnetic properties of a system such as the spin reorientation transition [52] and observation of perpendicular anisotropy in ultra thin films [53]. The basic underlying principle for MOKE is magnetic circular dichroism which translates in the rotation of polarization plane of incident light as well as the accrual of ellipticity. More details of the technique can be found in [51]. MOKE has been classified into three geometries depending upon the relative orientation of **M**, the plane of incidence and the sample surface and are shown in Figure 3.2.

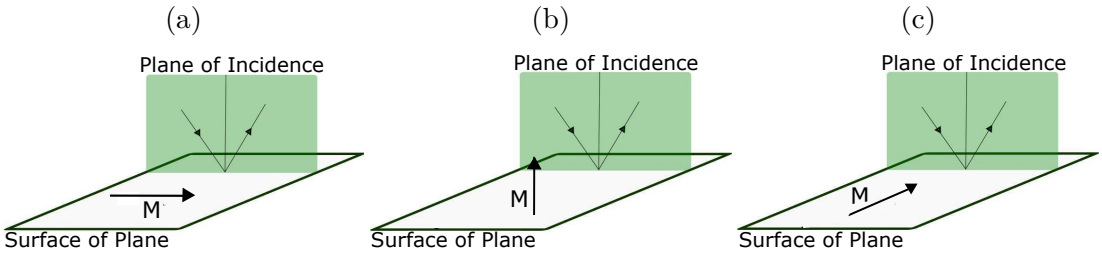

Figure 3.2: Different geometries of MOKE. In a) longitudinal geometry (L-MOKE) is shown in which **M** is parallel to the plane of incidence and sample surface, b) shows polar geometry (P-MOKE) in which **M** is parallel to the plane of incidence but perpendicular to the sample surface and c) transverse geometry in which **M** is perpendicular to the plane of incidence but parallel to the sample surface.

With the help of MOKE, we can find the easy and the hard axes of magnetic thin films. Here we've used two out of three geometries to find the direction of magnetization: L-MOKE (IP) and P-MOKE (OOP). Experimental setups of both geometries are shown in Figures 3.3 and 3.4.

Figure 3.5 illustrate the L- and P-MOKE measurement results for the 20 nm permalloy thin film ($S1$). It is noticeable in Figure 3.5a that magnetization saturates at low field values and the hysteresis loop is squarish, whereas for P-

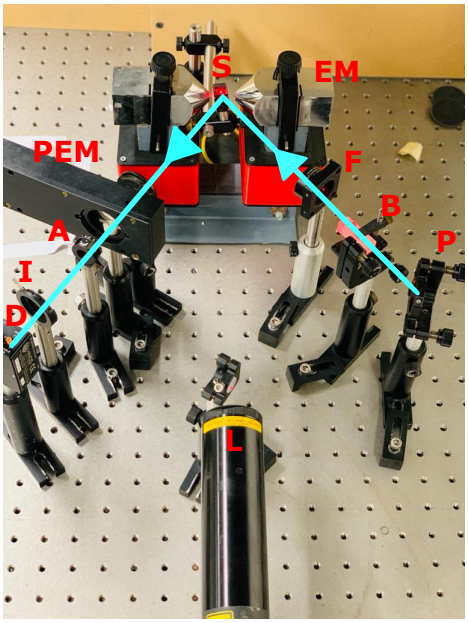

Figure 3.3: Experimental setup of the longitudinal MOKE geometry in which **M** is parallel to the plane of incidence and sample surface. Path taken by beam is shown in aqua color, where **L**= laser, **P**= polarizer, **B**= beam-splitter, **F**= focusing lens, **EM**= electromagnet, **S**= sample, **PEM**= photoelastic modulator, **A**= analyzer, **I**= iris, **D**= detector and **M**= mirror.

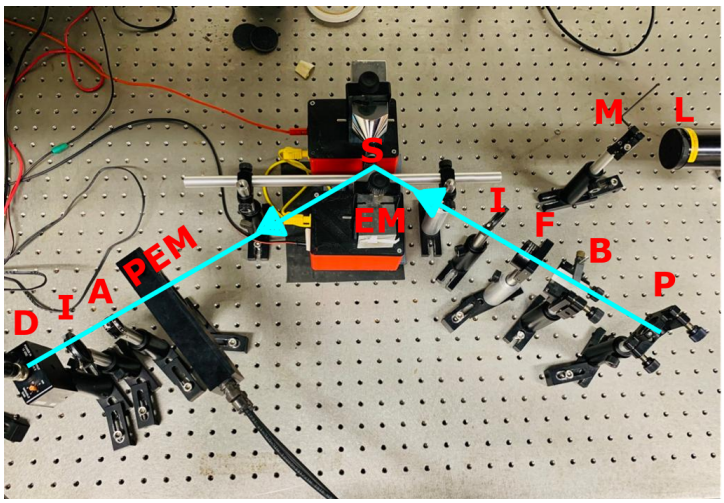

Figure 3.4: Experimental setup of the polar MOKE geometry in which **M** is parallel to the plane of incidence but perpendicular to the sample surface. Components identifies are the same as in Figure 3.3.

MOKE configuration, the magnetization vector does not align completely with the field applied perpendicular to the plane of thin film and the hysteresis loop

remains softer like a stretched **S**. The response is indicative of the presence of uniaxial anisotropy with the easy axis lying in-plane.

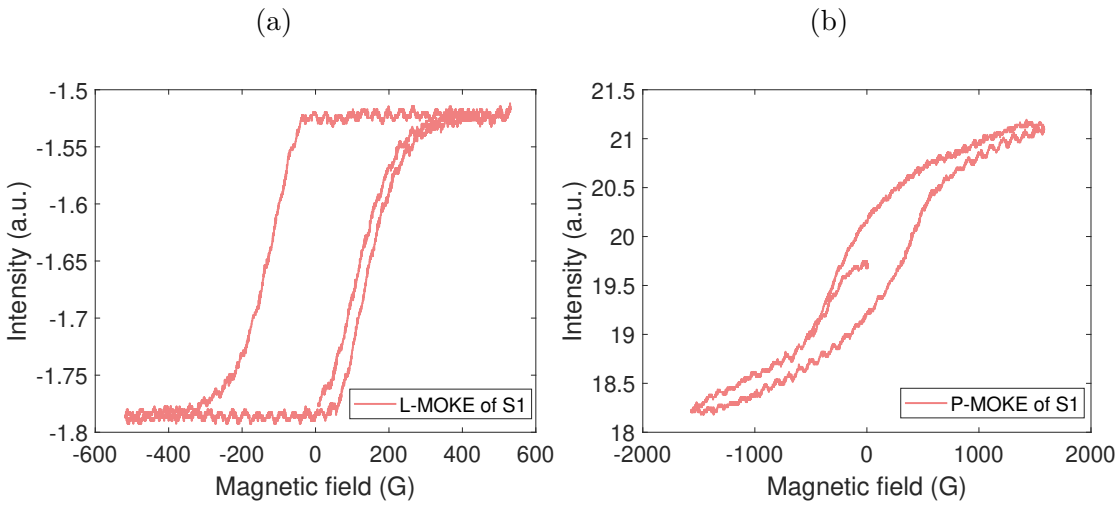

Figure 3.5: Graphs of intensity data obtained from lock-in amplifier as a function of external applied magnetic field ($\mathbf{H_o}$). In a) experimental result of L-MOKE for a 20 nm permalloy thin film is shown, whereas b) shows the experimental result of P-MOKE for the same thin film.

The discussion on thin film deposition and the experimental arrangement of MOKE ends here. The next section deals with another interesting topic, i.e., vector network analyzer (VNA), which is one of the two tools we employ for FMR.

3.3 Introduction to S-Parameters and VNA

The vector network analyzer (VNA) is an instrument used to investigate the characteristics of a device-under-test (DUT) by sending in electromagnetic waves. It works both as a source and detector in the frequency ranges that can go as high as upto hundreds of GHz. The incident waves are reflected or transmitted after interacting with the DUT. By measuring the power of reflection or transmission or both the scattering parameters of DUT can be measured and that too in a

phase-sensitive manner. Figure 3.6 shows how the DUT and the VNA interface with one another.

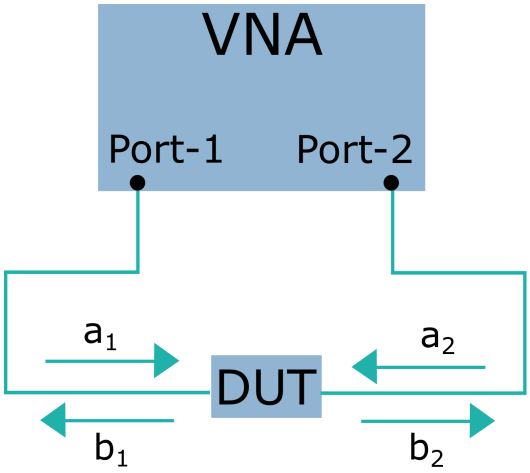

Figure 3.6: Interface between the VNA and the DUT.

The scattering parameters (S_{ij}) are the power ratios of incident waves at port-j measured at port-i, where $i, j = 1, 2$. Reflectance is measured by S_{11} and S_{22} parameters whereas S_{21} and S_{12} indicate the transmittance. The definitions of scattering parameters (S_{ij}) are given by

$$S_{11} = \frac{b_1}{a_1} = \frac{\text{reflected on port-1}}{\text{incident on port-1}}, \tag{3.1}$$

$$S_{12} = \frac{b_1}{a_2} = \frac{\text{transmitted on port-1}}{\text{incident on port-2}}, \tag{3.2}$$

$$S_{21} = \frac{b_2}{a_1} = \frac{\text{transmitted on port-2}}{\text{incident on port-1}}, \tag{3.3}$$

$$S_{22} = \frac{b_2}{a_2} = \frac{\text{reflected on port-2}}{\text{incident on port-2}}. \tag{3.4}$$

Like any other instrument VNA also needs to be calibrated for an accurate quantitative assessment of the device, in our case the stripline or CPW. One of the most common calibration methods is short-open-load-through (SOLT) which utilizes known standard parameters: a short circuit, an open circuit, a load which is matched to the overall system impedance and a through. What this means

is that DUT = S, O, L and T in four successive measurements and the measurement results are then referenced to the plane where the CPW and stripline are eventually placed. This protocol removes the background due to the cabling and connectors as well. These standard parameters are usually contained in the calibration kits.

Another important part of this chapter is to introduce the basic physics and fabrication of CPWs and striplines (we have employed both). In the following section, we discuss how we can fabricate and then use these CPWs and striplines for FMR measurements.

3.4 Basics of Waveguides for FMR

The coplanar waveguide (CPW) and the stripline works as a transmission line which connects the sample under investigation to the microwave source. A CPW on a dielectric substrate consists of a central conductor plane of width (w_g) and two ground planes at a distance of (w_{sg}) on either side. Besides the conventional CPW there is another type, called grounded-CPW with an additional ground plane at the bottom of the surface of dielectric substrate. The grounded-CPW not only provides mechanical support to the dielectric substrate [54] but also lowers the characteristic impedance [55].

On the other hand, stripline has a uni-planar transmission structure with only one strip conductor of width (w_g) [56]. The advantage of striplines over conventional CPWs is effectively more substrate area, improved characteristic impedance and no dependence on any additional wraparounds and via holes which induce additional parasitic elements [56]. Both of these geometries support a quasi-TEM mode [54] in which the central conductor plane or strip carries the rf signal which produces a magnetic field in the clockwise direction around conductor. The ge-

ometries of both, grounded-CPW and stripline are shown in Figure 3.7.

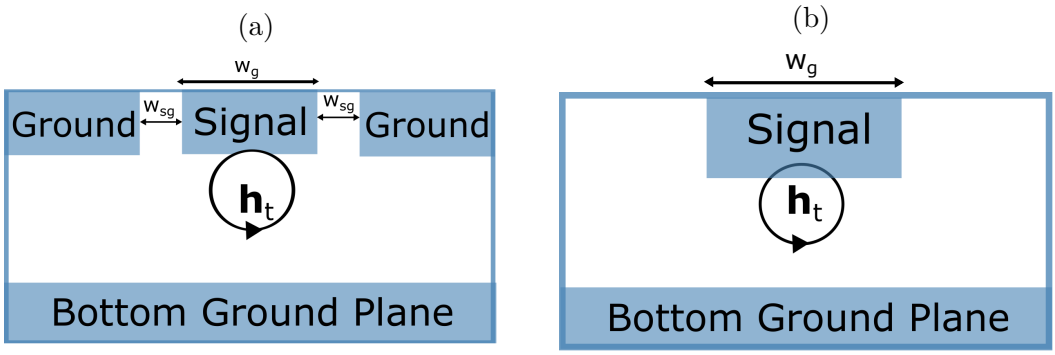

Figure 3.7: A schematic illustration of waveguides for FMR. In a) the geometry of grounded-CPW is shown, whereas b) shows the geometry of strilpline.

One of the key features while designing a CPW or stripline is impedance matching. Impedance mismatch causes unwanted reflection distorting the transmitted signal at higher frequencies which in turn compromises the quality and sensitivity of the FMR signal. Therefore, its important to have an impedance match of 50 Ω over a wide range of frequency.

In section 2.5 we introduced an ac magnetic field ($\mathbf{h}_t$) to excite the precession. This ac magnetic field ($\mathbf{h}_t$) is generated by an oscillating current (I_t) provided by the VNA coupled with the CPW or stripline through SMA connectors. One of our fabricated CPW and stripline are shown in Figure 3.8.

Figure 3.8: Lab built CPW and Z-shaped stripline with end-launch connectors.

Now, a little bit on how we fabricated our waveguides. In total, we've constructed three kinds of CPWs and one Z−line. For the FMR setup, the CPWs and striplines we've designed in our research lab are all fabricated with a PCB milling machine on a copper-plated dielectric substrate (Rogers RO4350b) which has a dielectric constant of 3.48 and thickness of 0.726 cm. We've designed several CPWs and striplines with different critical dimensions, depending on the type of connectors. Table 3.2 shows the center conductor width (w_{g}), ground to conductor distance (w_{sg}), ground width (w_{gr}), length and characteristic impedance of all CPWs and the Z-shaped stripline. All of these critical dimensions are calculated using [57]. The impedance mismatch was high with CPWs due to the limitation

Table 3.2: Critical dimensions and characteristic impedance of CPWs and Z-shaped stripline.

CPW Name	w_g (mm)	w_{sg} (mm)	w_{gr} (mm)	Length (mm)	Z_o (Ω)
CPW−1	1.2	0.2	5.8	25.4	48.7
CPW−2	1.4	0.4	5.8	25.4	42.6
CPW−3	1.2	0.2	5.8	25.4	53.7
Z−line	1.6	0.2	5.8	50.8	50.3

imposed by the PCB milling machine resolution (0.1 mm). Furthermore, due to the CPW mismatch we were not able to obtain a clear FMR signal, therefore we will be discussing only the stripline analysis in the forthcoming sections.

3.5 FMR with the VNA and Z-Line

3.5.1 Frequency Swept FMR

Kittel's equation (2.50) is the resonant condition for uniform mode FMR, which depends on both frequency and the strength of external magnetic field. In a

typical frequency swept FMR measurement, frequency is swept with the help of VNA at certain fixed magnetic field, with measurements subsequently repeated for a wide range of field values. At the FMR resonance, there is a measurable loss in the enhanced absorption coefficient (S_{11}) and the transmission coefficient (S_{21}) of the stripline. The absorption takes the form of a complex Lorentzian, a diagonal term in the susceptibility tensor described in Eq. (2.33) which we rewrite here [58]

$$\chi_{(\omega,H_o)} = \frac{\omega_m\big(\omega_o - i\Delta\omega\big)}{\big(\omega_o^2(H_o) - \omega^2\big) - i\omega\Delta\omega}, \tag{3.5}$$

where $\omega_m = \gamma\mu_o M_o$, $\omega_o = \gamma\mu_o H_o$ and $\Delta\omega$ is the linewidth (FWHM) of absorption peak shown in Figure 2.4. After some algebraic manipulations, Eq. (3.5) can be decomposed into the real and imaginary components as

$$\chi'_{(\omega,H_o)} = \omega_m\big(\frac{\omega_o(\omega_o^2 - \omega^2) + \Delta\omega^2\omega}{(\omega_o^2 - \omega^2) + \omega^2\Delta\omega^2}\big), \tag{3.6}$$

$$\chi''_{(\omega,H_o)} = i\omega_m\Delta\omega\big(\frac{\omega\omega_o - (\omega_o^2 - \omega^2)}{(\omega_o^2 - \omega^2) + \omega^2\Delta\omega^2}\big). \tag{3.7}$$

The mathematical forms given above can principally be fit to the data collected from VNA-FMR measurements.

In this work, rather than fitting the change in transmission parameter to the complex susceptibility, a new method is used which is known as the derivative-divide (d_D) method [58]. In this method, ferromagnetic resonance can be detected as an induced voltage in the conductor strip of the stripline which is connected to complex susceptibility as [59]

$$V_{induced} = -i\omega A V_o \chi(\omega, H_o)e^{i\phi}. \tag{3.8}$$

where A is the scaling parameter, $e^{i\phi}$ is the phase acquired due to the stripline and microwave wires and V_o is the voltage measured at port-2 when V_i voltage is applied at port-1 of the VNA. The transmission coefficient (S_{21}) also known as transmittance and can be written as

$$S_{21} = \frac{b_2}{a_1} = \frac{V_o}{V_i} e^{i\phi}. \tag{3.9}$$

If we take whole setup into account including the stripline and the VNA, there also exists a frequency dependent background voltage $e^{\iota\phi} V_o^B(\omega)$ with the induced voltage due to the losses induced by the stripline and electric length of the microwave wires. This background voltage and Eq. (3.8) modify Eq. (3.9) to

$$S_{21} = \frac{V_{induced} + e^{i\phi} V_o^B(\omega)}{V_i}. \tag{3.10}$$

We can use the d_D method to remove the frequency dependent background voltage. This analysis method involves the central differential of S_{21} w.r.t. H_o with a step of ΔH (not to be confused with the field linewidth of absorption peak) and can be written as

$$d_D S_{21}(\omega, H_o) = \frac{S_{21}(\omega, H_o + \Delta H) - S_{21}(\omega, H_o - \Delta H)}{S_{21}(\omega, H_o)\Delta H}. \tag{3.11}$$

Inserting the value of S_{21} from Eq. (3.10) into Eq. (3.11) we obtain

$$d_D S_{21}(\omega, H_o) = -i\omega A \frac{\chi(\omega, H_o + \Delta H) - \chi(\omega, H_o - \Delta H)}{\Delta H}, \tag{3.12}$$

which can also be recast as

$$d_D S_{21} = -i\omega A \frac{d\chi}{dH_o}. \tag{3.13}$$

Finally substituting the real and imaginary parts of susceptibility from Eqs. (3.6) and (3.7) into Eq. (3.13), we attain the real and imaginary parts of differential scattering parameter $d_D S_{21}$ as

$$d_D S_{21}^{'} = \omega A \frac{d\chi^{''}}{dH_o}, \tag{3.14}$$

$$d_D S_{21}^{''} = -i\omega A \frac{d\chi^{'}}{dH_o}. \tag{3.15}$$

Eqs. (3.14) and (3.15) produce complex Lorentzian signals which can be fit to the data collected from VNA-FMR measurements as shown in Figure 3.9.

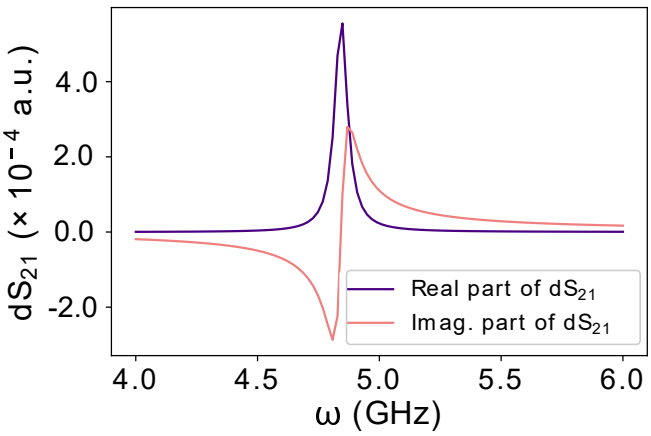

Figure 3.9: Graph of differential transmission scattering parameter ($d_D S_{21}$) as a function of resonance frequency (ω_o) for a fixed value of external magnetic field ($\mathbf{H}_o$).

The derivative-divide (d_D) method was developed to obtain the FMR signal in a broadband frequency range to remove the background voltage, noises and other non-magnetic field dependent components. The complex Lorentzian signals obtain from Eqs. (3.14) and (3.15) are equivalent to the data obtained from experimental frequency swept VNA-FMR and can be fit to experimental data in order to extract the desired FMR parameters.

Next, in the following section, we systematically introduce the analytical ex-

traction of measurement parameters like the resonant field, gyromagnetic ratio, saturation magnetization and damping parameter from FMR spectra.

3.5.2 Analytical Evaluation of Measurement Parameters

Kittel's equation not only gives the resonant condition for ferromagnetic materials but also tells how the resonant frequency changes by changing the external magnetic field parallel or perpendicular to the ferromagnetic material. This effect was illustrated in Figure 2.5 for different geometries.

The two types of FMR measurements, frequency and field swept have their own utility for convinience in extracting magnetic parameters. For example, by performing a field swept FMR measurement in IP or OOP configuration, we can find parameters associated with a magnetic system such as the effective magnetization ($\mathbf{M}_{\mathrm{o}}$), gyromagnetic ratio (γ), Landé g-factor (g), the anisotropy field ($\mathbf{H}_{\mathrm{a}}$) and inhomogeneous broadening (ΔH_o). The inhomogeneous broadening can be defined as the measure of magnetic material's imhomogeneties.

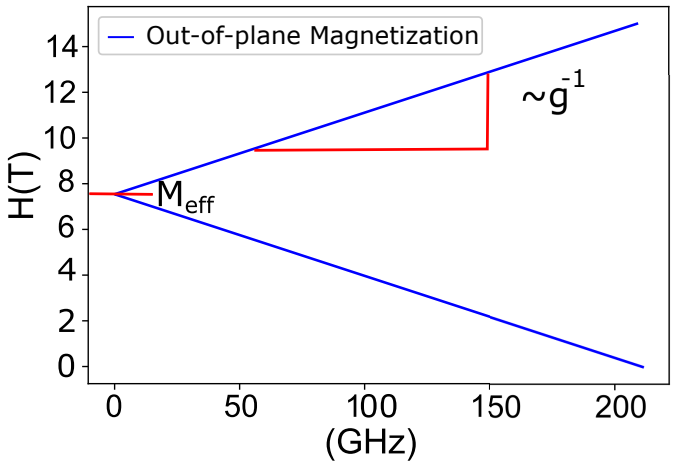

Figure 3.10: Graph of resonance frequency (ω_o) as a function of external magnetic field ($\mathbf{H}_{\mathrm{o}}$) for a thin film in which $\mathbf{H}_{\mathrm{o}}$ is perpendicular to the surface of thin film.

As discussed in Section 2.6, the resonance frequency of a thin film with OOP

magnetization remains very high even in the absence of external magnetic field which can be very useful for the extraction of measurement parameters. This idea is shown in Figure 3.10. Considering a linear relationship between $\mathbf{B}$ and $\mathbf{H}_{\mathrm{o}}$, i.e., $\mathbf{B} = \mu_o \mathbf{H}_{\mathrm{o}}$, Eq. (2.52) can be modified as

$$\mathbf{B} = \frac{\omega_o}{\gamma} + \mu_o \gamma \mathbf{M}_{\mathrm{o}}, \tag{3.16}$$

where $\omega_o = 2\pi f$ and Eq. (3.16) is similar to the equation for a straight line whose slope and y-intercept are given by $\mu_o 2\pi/\gamma = \mu_o 2\pi\hbar/g\mu_B$ and $\mu_o \gamma \mathbf{M}_{\mathrm{o}}$, respectively. From the slope we can thus find the gyromagnetic ratio (γ) which could lead us to the Landé g-factor (g). Similarly, from the intercept we can find the effective magnetization ($\mathbf{M}_{\mathrm{o}}$). Furthermore, from the effective magnetization we can estimate the anisotropy field ($\mathbf{H}_{\mathrm{a}}$) using the expression [58].

$$\mathbf{M}_{\mathrm{o}} = \mathbf{M}_s - \mathbf{H}_a, \tag{3.17}$$

where $\mathbf{M}_{\mathrm{s}}$ is the saturation magnetization (estimated theoretically) and $\mathbf{H}_{\mathrm{a}}$ is the anisotropy field.

3.5.2.1 Field Linewidth

For a field swept FMR measurement, the resonance occur when the absorbed power is maximum, yielding, $H_o = H_r$, such that $\omega_o = \gamma \mu_o H_r$. The linewidth is defined as the width of the absorption curve for which the complex susceptibility is half compared to its maximum value. By measuring the linewidth from field swept FMR measurement, we can get information about the Gilbert's damping constant (α) and inhomogeneous broadening (ΔH_o) which is shown as [60]

$$\Delta H = \Delta H_o + \frac{2\alpha\omega_o}{\sqrt{3}|\gamma|2\pi}, \tag{3.18}$$

where ΔH is the field linewidth (FWHM), $\omega_o/2\pi$ is the specific applied frequency and ΔH_o is the inhomogeneous broadening (arising from sample imperfections). It's not straightforward to calculate α directly from Eq. (3.18) because there exists another unknown parameter (ΔH_{o}).

3.5.2.2 Frequency Linewidth

In order to extract Gilbert's damping parameter from frequency swept FMR measurement we have to modify the field linewidth by differentiating the Kittel's equation. (2.50) w.r.t. the effective field (H_{eff}). But first, let's define ΔH as

$$\Delta H = \Delta\omega \frac{\partial H_o}{\partial \omega}, \tag{3.19}$$

where $\Delta\omega$ is the frequency linewidth (FWHM) of the absorption curve and H_o is the resonant field. Extracting the value of H_o from Kittel's equation (2.52) as

$$H_o = \frac{\omega_o}{\mu_o \gamma} + M_o. \tag{3.20}$$

If we insert the values of H_o and ΔH from Eqs. (3.20) and (3.18), respectively into Eq. (3.19). We get the OOP frequency linewidth $\Delta\omega$ as [60]

$$\Delta\omega = \gamma\mu_o \Delta H_o + 2\alpha\omega_o. \tag{3.21}$$

Eq. (3.21) illustrates that there is a linear dependence of linewidth ($\Delta\omega$) on both the resonant frequency (ω_{o}) and inhomogeneous broadening (ΔH_o). The frequency linewidth obtain from Eq. (3.21) can be fit to experimental data obtain from OOP VNA-FMR measurement in order to extract Gilbert's damping parameter. Similarly, for an IP frequency swept FMR measurement, we can define

$\Delta\omega$ as

$$\Delta\omega = \Delta H \frac{\partial \omega_o}{\partial H}. \tag{3.22}$$

If we put the value of ω_o from Eq. (2.53) into Eq. (3.22), we get

$$\Delta\omega = \gamma\mu_o \Delta H \frac{\partial \left(H_o^2 + H_o M_o\right)^2}{\partial H}. \tag{3.23}$$

By putting the the value of ΔH from Eq. (3.18) into Eq. (3.23) and differentiate w.r.t. the applied field H, we get the IP frequency linewidth $\Delta\omega$ as [60]

$$\Delta\omega = (2\alpha\omega_o + \gamma\Delta H_o)\sqrt{1 + \left(\frac{\gamma M_o}{2\omega_o}\right)^2}, \tag{3.24}$$

which depicts an inverse square-root dependence of $\Delta\omega$ on ω_o. The frequency linewidth obtain from Eq. (3.24) can be fit to experimental data obtain from IP VNA-FMR measurement in order to extract Gilbert's damping parameter.

This completes our analytic discussion on the field and frequency swept VNA-FMR. The foregoing discussion is also important for the analytical evaluation of measurement parameters. In the next section, we'll discuss the experiment in which we obtain the FMR response of our thin film samples using IP frequency swept VNA-FMR scheme.

3.5.3 Experimental Methods for IP VNA-FMR Measurements

Figure 3.11 shows the schematic arrangement of an IP frequency swept VNA-FMR spectrometer. For VNA-FMR measurements a Z-shaped stripline (Z−line) has been used. A broadband microwave generator PicoVNA-106 (3 to 6 GHz) generates an rf signal that passes through the stripline and gives rise to an os-

cillating magnetic field. A gauss meter is used to measure the ac and dc fields. The DUT is placed inside a GMW-3470 electromagnet that generates a static dc magnetic field. The DUT has been kept in place with the help of 58 mm long SMA cable holders, whose drawings are shown in Appendix A.3.

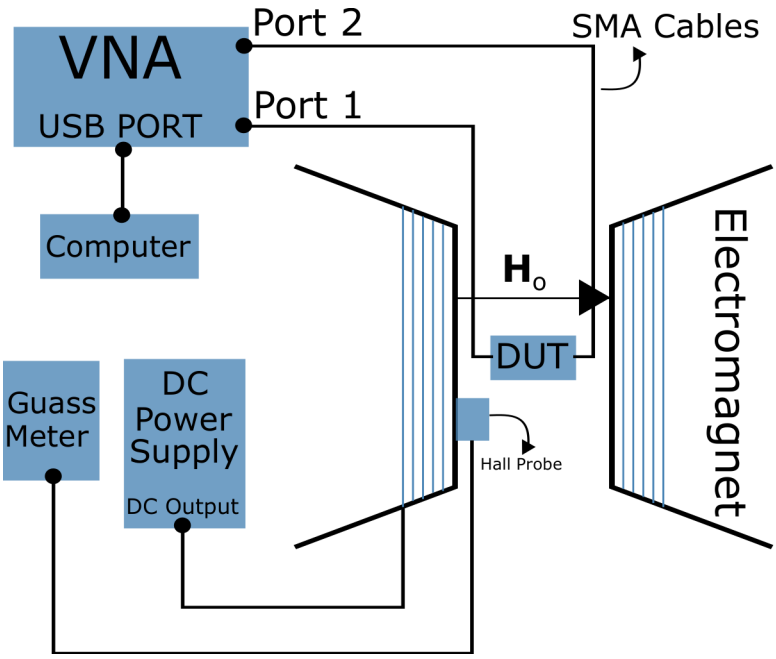

Figure 3.11: A schematic illustration of VNA-FMR spectrometer with IP frequency swept technique. The DUT is placed between the electromagnet and VNA works in tandem as a source and as a detector.

The rf microwave signal going through the Z−line generates an ac magnetic field which excites the sample. The technique we have developed employes a flip-chip method in which the sample is placed face down on the Z−line and a layer of Kapton tape is put in between to electrically insulate the sample from stripline. The electromagnet is powered by a Sorensen-DLM power supply which is integrated and interfaced with computer within the Labview environment, shown in Appendix (A.4). We've used data acquisition card (National Instruments, PCI−6221) for digitization of analog input from the power supply in order to generate the control signal for the electromagnet. The complete hardware is

computer controlled.

The VNA has two ports, port-1 generates the rf microwaves and detect the change in the absorption energy at port-2. For the FMR measurement, the stripline (Z−line) is connected to both ports of VNA via SMA cables to measure the transmission coefficient S_{21}. The range of frequency sweep is 0.01 to 6 GHz with a step size of 100 Hz so that the whole sweep contains 512 points of transmission coefficient S_{21} taken at a particular value of the static magnetic filed ($\mathbf{H}_o$). This static dc magnetic filed is along the plane of stripline as shown in Figure 3.12.

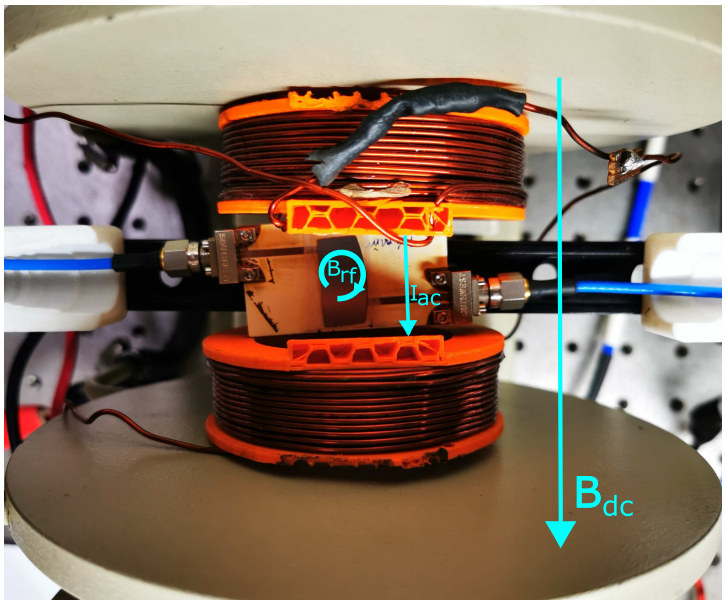

Figure 3.12: Plane view of the DUT placed inside the VNA-FMR spectrometer with frequency swept technique in IP configuration, in which a 100 nm permalloy sample ($S4$) is placed on the Z−line.

It is worth mentioning here that the ac magnetic field generated by rf signal should be perpendicular to the applied static dc magnetic field. The frequency is swept through stripline and scattering parameters are measured at a particular value of applied magnetic field. This process is repeated 15 times as the applied static field is changed from 0.45 to 20.2 mT with a step of 0.9 mT.

The forgoing discussion covers the experimental method for the VNA-FMR mea-

surement in determining the static and dynamical properties of ferromagnetic samples. The next section discusses the FMR responses of the various permalloy samples.

3.6 Results from the IP VNA-FMR Scheme

For FMR measurements of $S2$, $S3$ and $S4$ with Z−line we fixed the input power level to −3 dBm, number of sweep points to 512 and selected measurement bandwidth of 50 Hz. A Matlab script is written to plot the real and differential real parts of S_{21} which is reproduced in Appendix A.6. Figure 3.13 shows differential real parts of S_{21} for samples $S2$ and $S3$. These differentials are defined in Eqs. (3.14) and (3.15), respectively. We now interpret these results, in light of forgoing discussion.

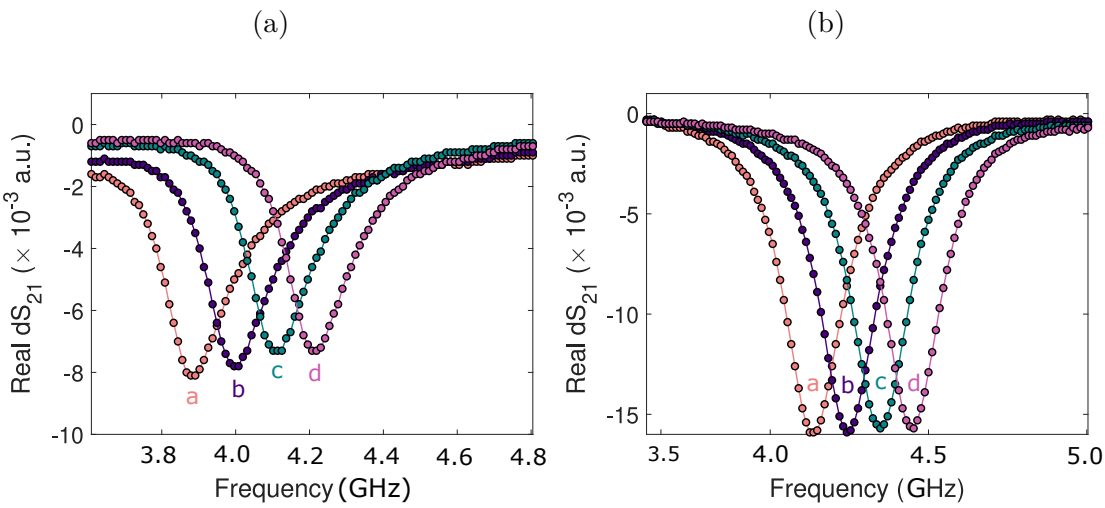

Figure 3.13: Graphs of resonance frequency ($\omega_o/2\pi$) plotted against the differential real part of transmission coefficient (dS_{21}) for $S2$ and $S3$ with $\mathbf{H}_o$ applied parallel to the plane of thin films, where **a** = 0.45 mT−74.6 mT, **b** = 1.35 mT−74.6 mT, **c** = 2.16 mT−74.6 mT and **d** = 3.08 mT−74.6 mT. Solid lines are guide to the eyes.

It is noticeable that varying the magnetic field changes the resonance frequency.

Consequentially, the resonant peaks shift towards higher frequencies as $\mathbf{H}_o$ goes up. The differential is obtained by subtracting the transmission signal in the presence of sample at a very high field value from the transmission signal in the presence of sample at low field values. The reason for taking a very high field value is that the signal becomes non-magnetic at such high field values as it goes out of the resonance frequency range. A similar result obtained for $S4$ is shown in Figure 3.14.

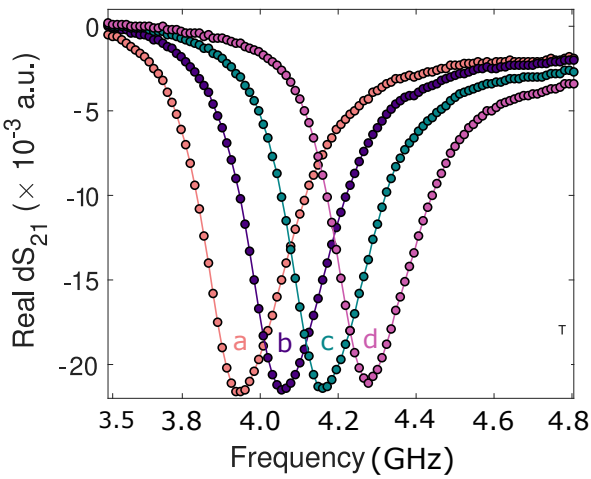

Figure 3.14: Graph of resonant frequency ($\omega_o/2\pi$) plotted against the differential real part of transmission parameter (dS_{21}) for the 100 nm permalloy thin film, where **a** = 0.45 mT−74.6 mT, **b** = 1.35 mT−74.6 mT, **c** = 2.16 mT−74.6 mT and **d** = 3.08 mT−74.6 mT. Solid lines are guide to the eyes.

From Kittel's Eq. (2.50) we can calculate the resonance frequencies (ω_o) of our thin film samples. For the applied static magnetic field range (0.45 to 20.17 mT), the resonant frequency (ω_o) ranges from a few MHz to nearly 6 GHz. There are two parameters which are crucial for FMR measurement: power levels (P) and bandwidths (BW). Bandwidth basically determines the available dynamic range during the frequency swept measurements because it truncates the frequency domain data at fixed values.

We've tried different combinations of these parameters with the Z−line. Both of

these parameters are central because changing the power level and the bandwidth have dramatic effects on the FMR response of thin film samples. For example, by increasing the power level of VNA, the strength of the FMR signal decreases and if we increase the bandwidth of VNA, it will decrease the resulting amplitude of the FMR signal.

This completes our discussion on FMR spectra of different ferromagnetic thin film samples. The next step is parameter extraction based on the methods outlined on Section 3.5.2.

3.7 Extraction of Measurement Parameters

3.7.1 Resonance Frequency

In order to extract the resonance frequencies from FMR measurements of $S2$, $S3$ and $S4$ thin film samples, as illustrated in Figures 3.13 and 3.14, we need to extract a representative portion of each absorption peak. This is done by selecting real and imaginary parts of a specific resonance peak at a constant field value from the experimental FMR data. Then, Eqs. (3.14) and (3.15) are fit to the experimental FMR data in order to get the resonance frequency of each peak. A python script is written for the curve fitting which is reproduced in Appendix A.6.

The resonance peak has the shape of a Lorentzian function with resonance occurring at the maximum value of differential S_{21}. The real and imaginary parts of resonance peaks for samples $S2$, $S3$ and $S4$ are shown in Figures 3.15.

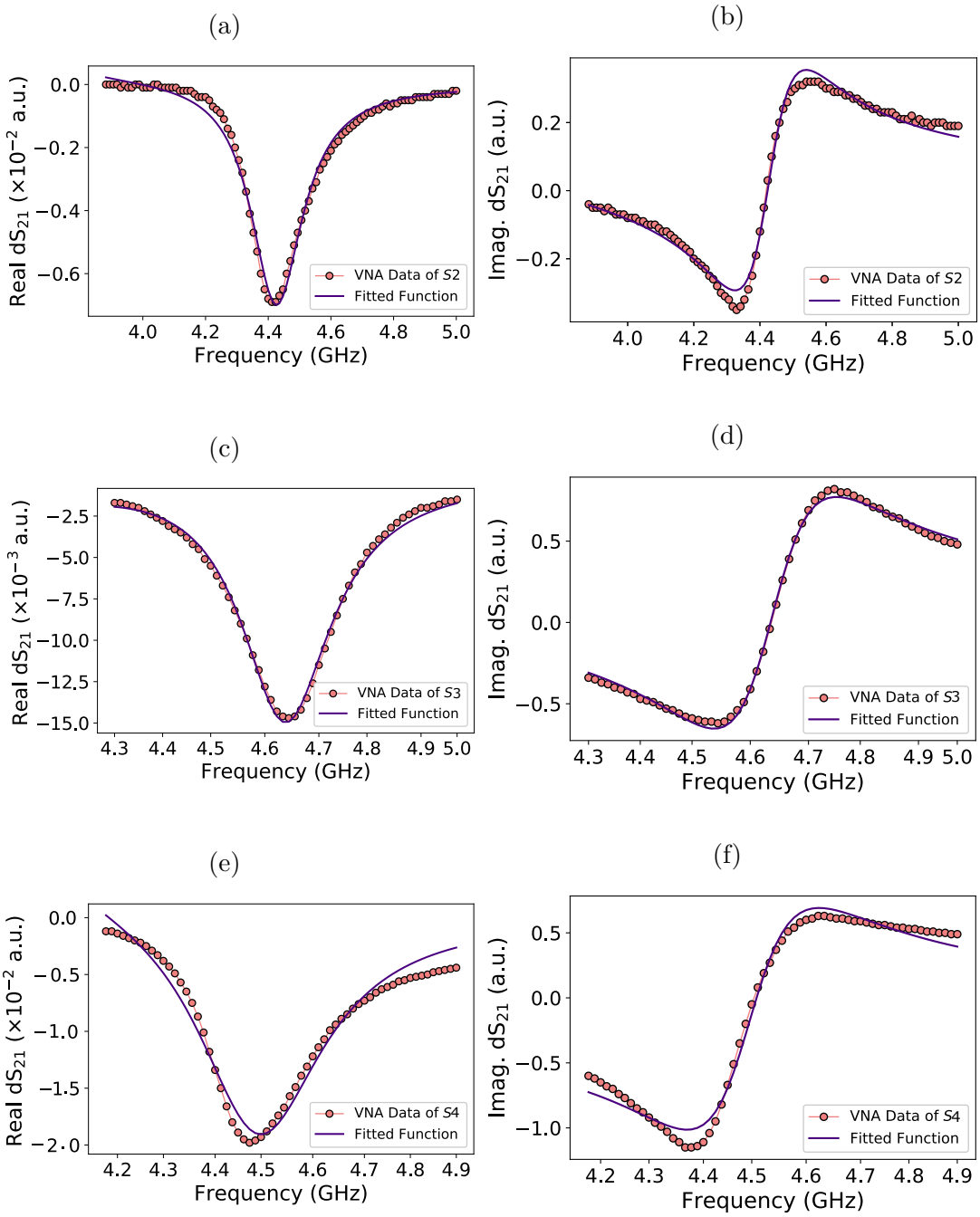

Figure 3.15: Real and imaginary parts of a specific portion of FMR data plotted against the resonance frequency ($\omega_o/2\pi$) for the 49 nm, 72 nm and 100 nm permalloy thin film samples. Solid lines are the least square curve fit to the experimental data. The data is fit to Eqs. (3.14) and (3.15).

3.7.2 Gyromagnetic Ratio and Saturation Magnetization

In order to extract the values of gyroamgnetic ratio (γ) and saturation magnetization ($\mathbf{M}_s$) for our thin film samples we've written a python script which curve fits Kittel's Eq. (2.53) onto the experimental FMR data. Fitting is done using the Optimize library in python and the code is reproduced in Appendix A.6. The

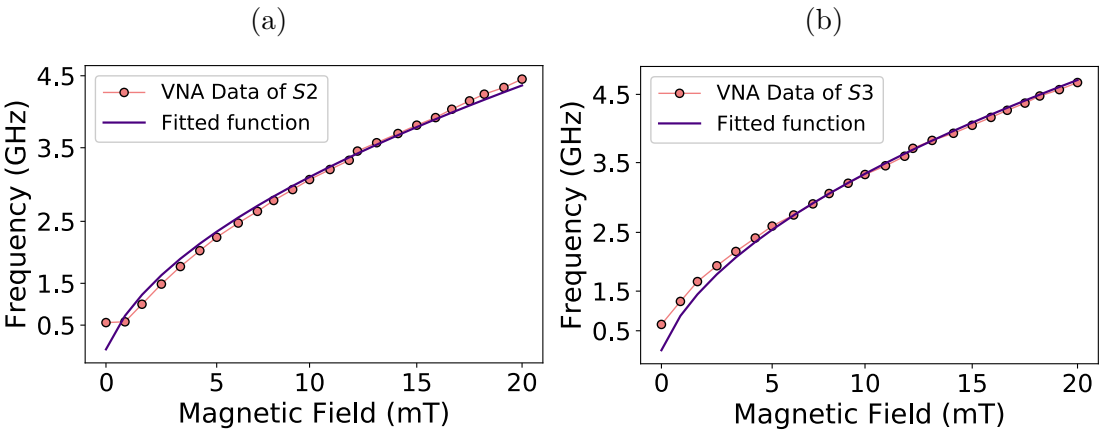

Figure 3.16: Graphs of static magnetic field ($\mathbf{H}_o$) as a function of resonance frequency ($\omega_o/2\pi$) for $S2$ and $S3$ in IP configuration are shown in a) and b), respectively. Solid lines are least square curve fit to the experimental data. The data is fit to Eq. (2.53).

average value of saturation magnetization ($\mathbf{M}_s$) is found by Kittel's Eq. (2.53) and then the algorithm makes use of this value to calculate the Landé g-factor (g) for our thin film samples. The extracted value of $\mathbf{M}_s$ is $\approx$ 1.107 T for all three samples which is in excellent agreement with reported value of 1.114 [55]. Similarly, the extracted values of g are found to be: 2.0601, 2.225 and 2.0871 for $S2$, $S3$ and $S4$, respectively. These values are in good agreement with the literature value of 2.0–2.14 [61].

After extracting the value of g we used the expression $\gamma = g\mu_B/\hbar$, to calculate the values of gyromagnetic ratio (γ) in rad s^{-1} T^{-1}. After conversion, the extracted values of γ in GHz T^{-1} are: 28.94, 31.26 and 29.32 for $S2$, $S3$ and

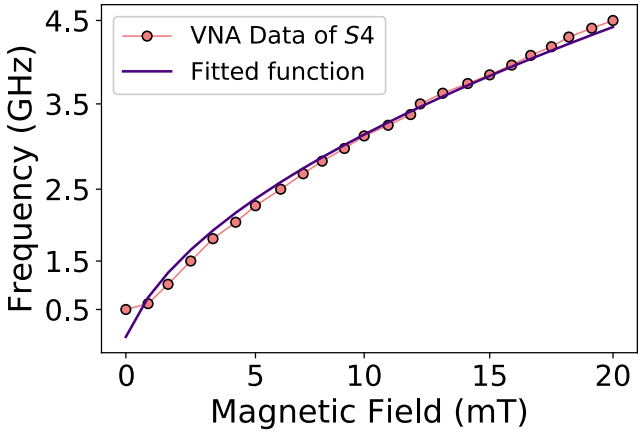

Figure 3.17: Graph of static magnetic field ($\mathbf{H}_o$) plotted against the resonant frequency ($\omega/2\pi$) for $S4$ in IP configuration. Solid line is least square curve fit to the experimental data.

$S4$, respectively. It's clear that the extracted values of γ are in good agreement with the values found in literature [61]. However, the 72 nm thin film exhibits a systematically higher vale of the gyromagnetic ratio.

3.7.3 Gilbert's Damping Parameter

In order to extract the values of Gilbert's damping parameter (α) for our thin film samples a Matlab script is written to find the resonance frequency and linewidth of each absorption peak using the FindPeaks library. Linewidth of each peak has been extracted by choosing the fitting area of each peak manually. After extracting the linewidth of each peak, Eq. (3.24) is fitted to the experimental FMR data using a Python script. The script makes use of Eq. (3.24) and extracted values of $\mathbf{M}_s$ and γ for curve fitting in order to calculate the values of α and the inhomogeneous line broadening (ΔH_o). Matlab and Python scripts are reproduced in Appendix A.6. The graphs of resonance frequency vs linewidth (FWHM) for $S2$ and $S3$ and $S4$ are shown in Figures 3.18 and 3.19.

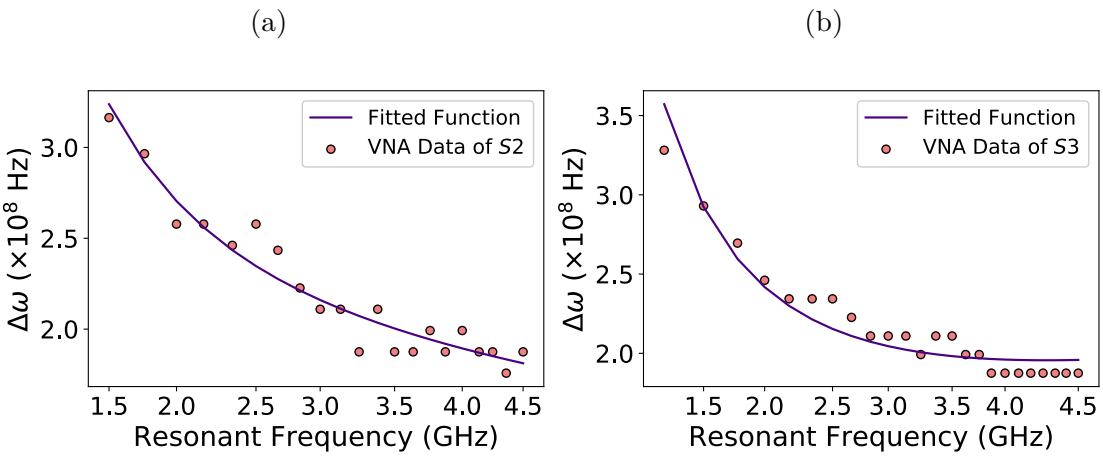

Figure 3.18: Graphs of resonant frequency ($\omega_o/2\pi$) plotted against the linewidth (FWHM) for $S2$ and $S3$ in IP configuration are shown in a) and b), respectively. Solid lines are least square curve fit to the experimental data. The data is fit against Eq. (3.24).

The extracted values of Gilbert's damping parameter (α) and inhomogeneous line broadening (ΔH_o) are presented in Table 3.3 which show that ΔH_o is comparable to the values found in some other studies of permalloy thin films [62].

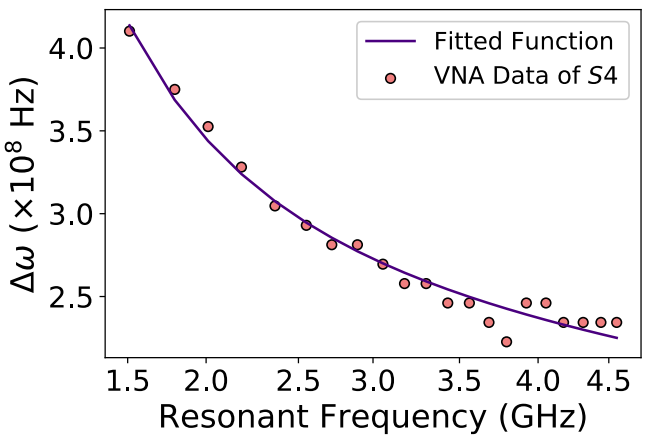

Figure 3.19: Graph of resonant frequency ($\omega/2\pi$) plotted against the linewidth (FWHM) for $S4$ in IP configuration. Solid lines are least square curve fit to the experimental data. The data is fit against Eq. (3.24).

The values of α are also comparable with the values mentioned in literature 0.003–

0.009 [62]. However, some previous studies shows that the value of α increases sharply with permalloy thin films of thickness lesser than 10 nm [63] and there's a little dependence on the film thickness above 30 nm [64]. Clearly, this was not the case for our thin film samples.

Table 3.3: Extracted VNA-FMR measurement parameters for IP configuration.

Sample	$\mathbf{M_s}$ (T)	**g**	$\boldsymbol{\gamma}$ (GHz T^{-1})	$\boldsymbol{\alpha}$	ΔH_o (T)	$\mathbf{A}(\times 10^{-8})$
NiFe 49 nm	1.107	2.060	28.94	0.004	0.023	2.873
NiFe 72 nm	1.107	2.225	31.26	0.005	0.047	5.335
NiFe 100 nm	1.107	2.087	29.32	0.006	0.057	8.618

The above table summarises all the parameters that we've extracted for the different permalloy thin films from VNA-FMR technique in IP configuration. We can say that the extracted parameters are in good agreement with established, well known empirical results, validating our experimental technique and measurement protocol.

Chapter 4

Lock-In Amplifier Based Phase Sensitive Detection of FMR

In a ferromagnetic resonance experiment, the resonance occurs in the microwave range by exciting the ferromagnetic sample with commonly applied fields (rf and dc) and measuring the response of the sample [65]. Since varying the microwave frequency varies the rf field which in return produces some changes in the magnetization dynamics, usually ferromagnetic resonance experiments are done by sweeping the external magnetic field at fixed frequency values. The resonance occurs when the applied magnetic field intensity is maximum, i.e., $H_o = H_r$ yielding, $\omega_o = \gamma\mu_o H_r$.

In Chapter 3, we discussed the basic underlying principles of the VNA-FMR technique which implies the frequency sweep at fixed magnetic field values. It was a fast but less sensitive technique. In this chapter, we'll discuss a slow but considerably more sensitive technique that we have developed for the measurements of thin film samples. This technique uses the phase-sensitive lock-in detection (LI) and implies a field sweep response of the magnetic sample.

Before discussing the LI-FMR detection in detail we need to discuss how a lock-in

amplifier works and measures the FMR response of ferromagnetic thin films. The chapter is organized by discussing the basics of lock-in amplifier followed by the testing of rf components. We then go into the specifics of LI-FMR, explaining the setup we built and present the data acquired from a systematic protocol of measurement on this system. Finally, we extract useful parameters and interpret the physics.

4.1 Basics of the Lock-In Amplifier

The lock-in amplifier is an incredibly powerful tool to detect weak, noisy and repetitive (sine wave) signals. It works on the basic principle of phase-sensitive detection (PSD) which is instrumental in picking up a weak signal possibly buried in the noise. This technique makes uses of a reference signal which has the same frequency and a fixed phase relationship with a noisy input signal. This reference signal could be a synchronized output of a function generator which is also the excitation source of the weak signal. One can read more about lock-in amplifiers in application notes such as [66].

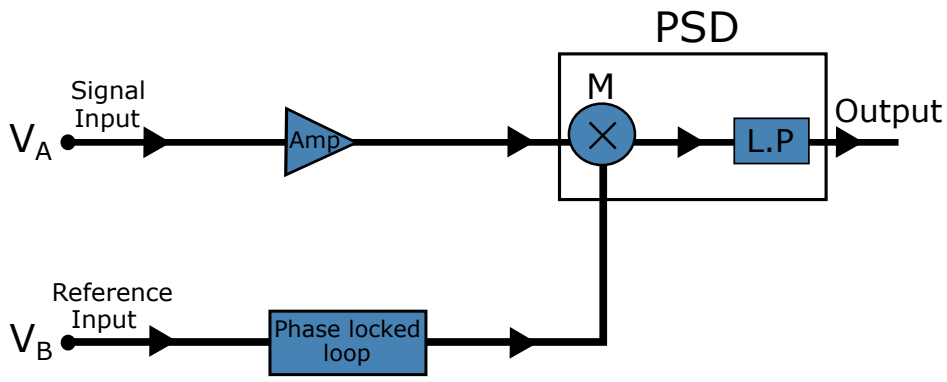

Figure 4.1: Block diagram of phase-sensitive lock-in amplifier, where **Amp**= amplifier, **PSD**= phase-sensitive detection box, **M**= mixer and **L.P**= low pas filter.

A lock-in amplifier has two input signals, i.e., input signal $\mathbf{V}_A$ and reference

signal $\mathbf{V}_{\mathrm{B}}$, and an output signal which has the same amplitude as of the input signal as shown in Figure 4.1. The output signal provides information about the phase relationship between the input signal and the reference signal. To understand this working better, let's consider that input signal $\mathbf{V}_{\mathrm{A}}$ has a frequency ω_{sig} and reference signal $\mathbf{V}_{\mathrm{B}}$ has a particular frequency ω_{ref} and the signals are given by

$$V_{in} = V_A \sin(\omega_{sig} t + \theta_{sig}), \tag{4.1}$$

$$V_{ref} = V_B \sin(\omega_{ref} t + \theta_{ref}). \tag{4.2}$$

Principally, the lock-in amplifier will take these two signals and multiply them using using an analog mixer. The output signal of the PSD has a dc component and high frequency harmonics given by

$$\begin{aligned} V_{PSD} = \frac{1}{2} V_A V_B \cos\Big((\omega_{sig} - \omega_{ref})t + (\theta_{sig} - \theta_{ref}) \Big) \\ -\frac{1}{2} V_A V_B \cos\Big((\omega_{sig} + \omega_{ref})t + (\theta_{sig} + \theta_{ref}) \Big). \end{aligned} \tag{4.3}$$

There are two different ac signals, one is the difference of frequencies $(\omega_{sig} - \omega_{ref})$ and one is their sum $(\omega_{sig} + \omega_{ref})$. The PSD output is then passed through a low-pass filter to remove the high frequency ac signal which is the second term on the R.H.S. For a special case, when the input frequency exactly matches the reference frequency, i.e., $\omega_{sig} = \omega_{ref}$, Eq. (4.3) assumes the form

$$V_{PSD} = \frac{1}{2} V_A V_B \cos(\theta_{sig} - \theta_{ref}), \tag{4.4}$$

which is a dc signal, ideally with no oscillatory term and proportional to the amplitude of input signal $\mathbf{V}_{\mathrm{A}}$.

The lock-in technique is valuable for FMR measurement because it helps in ex-

tracting the signal buried in noise. The only requirement is to make the signal oscillatory, a process that is called *modulation*. For an FMR measurement, the output signal (V_{PSD}) is proportional to the first derivative of complex susceptibility as a function of field ($\partial\chi/\partial H$). To understand this why this is the case, we first have to consider the I-V characteristics of an FMR system which is a microscopic device, i.e., I-V curve is not a straight line. That means we have to measure the gradient or slope at each point of the curve in order to have a better idea about the FMR response of a ferromagnetic thin film.

If we consider the complex susceptibility of DUT as a function of field $\mathbf{H}$ as: $\chi(\mathbf{H})$. Modulation produces an ac signal on top of a dc signal given as $\chi(\mathbf{H}_\mathrm{o} + \mathbf{h}e^{i\omega t})$. Now, if we expand this term by Taylor series ignoring the higher-order terms as

$$\chi(\mathbf{H}) = \chi(\mathbf{H}_\mathrm{o}) + (i\omega\mathbf{h})\frac{\partial\chi}{\partial H}\Big|_{\mathbf{H}_\mathrm{o}} e^{i\omega t} + \frac{(i\omega\mathbf{h})^2}{2}\frac{\partial^2\chi}{\partial H^2}\Big|_{\mathbf{H}_\mathrm{o}} e^{2i\omega t} + \cdots , \tag{4.5}$$

where the first term in the above equation is a dc term which will be removed by the lock-in amplifier and we'll be left with the oscillating term iso-frequency with the field modulation frequency (ω). Moreover, the shape of the absorption curve is the product of first derivative of the susceptibility ($\partial\chi/\partial H$) and the modulation frequency (ω). From Eq. (4.5) we can also say that to measure the first derivative we have to measure the first harmonics (1ω) and second harmonics (2ω) for the second derivative and so on.

4.2 Experimental Method for Lock-In Detection Based FMR

4.2.1 Overview of Field Swept FMR

In a typical field swept FMR measurement, the frequency is kept constant while magnetic field is swept over a wide range of fields, with measurements repeated for different frequency values. In this section, we are going to demonstrate how one can create an FMR with a lock-in amplifier, obviating the need for VNA, and the system is highly capable of detecting FMR spectra of ferromagnetic ultra thin film samples. Some of the samples may give such a low SNR that it might be difficult to detect with a VNA.

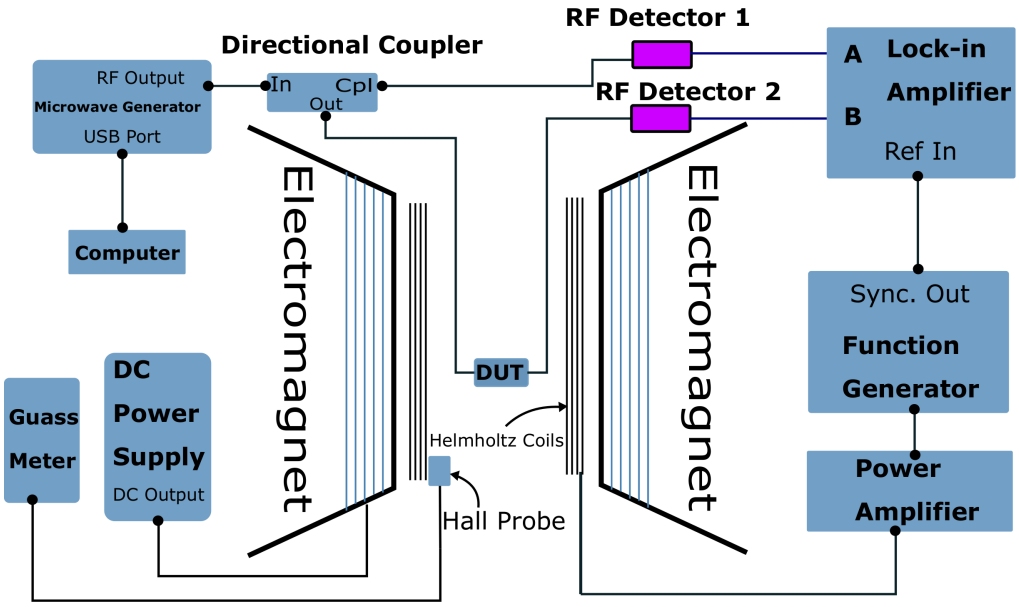

Figure 4.2: A schematic illustration of IP field swept LI-FMR spectrometer. The DUT is placed between the electromagnet and a pair of Helmholtz coils. A lock-in amplifier is also used to detect the output signal coming from the rf power detectors.

This system is based on conventional microwave components indicating a mi-

crowave generator, a function generator and rf detectors. All of these components together with the stripline and the lock-in amplifier (which serves as a detector) measure the FMR response of a ferromagnetic thin film in a broadband manner. Broadband means the system is not placed in a resonant cavity whose characteristics need to be altered every time the excitation frequency is varied. A schematic diagram of the field swept lock-in detection is shown in Figure 4.2.

The FMR responses are usually weak, therefore a lock-in amplifier is used to increase the signal to noise ratio. In Figure 4.2 the DUT is placed between the electromagnet which provides a dc field and a pair of Helmholtz coils is also mounted inside the electromagnets which serves as a source of modulation frequency. A power amplifier is used to provide current to the Helmholtz coils and a gauss meter is also used to measure the ac and dc fields. A function generator is used to provide the modulation frequency to Helmholtz coils and a reference signal to lock-in amplifier. The rf source generates a microwave signal that goes into the in-port of directional coupler and passes to the stripline which produces an rf field perpendicular to the applied dc field. The rf FMR signal coming from the stripline is converted into low frequency signal by an rf power detector (D2). The rf microwave signal coming from the cpl-port of directional coupler is also converted into low frequency signal by another rf power detector (D1). Both of these signal are detected through the lock-in amplifier's differential (A-B) mode.

4.2.2 Individual Testing of RF Components

The rf components which are mentioned in Table 4.1 are tested before using in our actual setup to check the reliability and behaviour of each component. We learn about the system in this patient, painstaking experimental ordeal and can later troubleshoot or make better optimization.

Table 4.1: RF components along with the brand names.

Components	**Brand**
Microwave generator	PicoSource AS-108
Power splitter	Mini-Circuits ZFRSC-183-S+
Directional coupler	Mini-Circuits ZCDC10-01203-S+
RF detectors	Mini-Circuits ZX47-55-S+
RF cables	Mini-Circuits 30-222726-10H+S
Digital oscilloscope	Agilent DXO-X-2002A

For each component, we provide input power from a microwave source quantify the output on a digital oscilloscope. The range of our microwave source is 3 kHz to 8 GHz with a power output ranging from −15 to +15 dBm. The measurement range of our oscilloscope is μs to 70 MHz only. So, we limit the testing frequency at about 50 MHz and a power of 0 dBm. The output is checked on an oscilloscope and the test bench is shown in Figure 4.3.

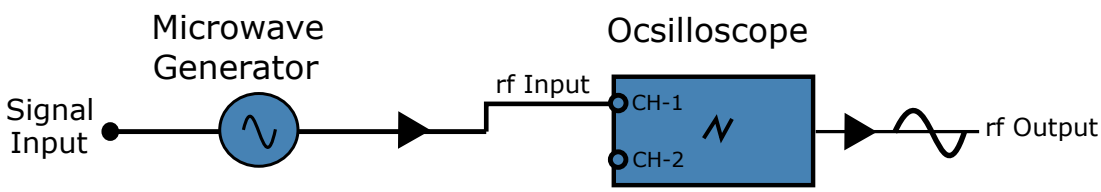

Figure 4.3: Block diagram of an oscilloscope interface showing an rf output of 530 mV when an rf input signal of 50 MHz and 0 dBm power is generated by the microwave source.

A 2 way-0° ZFRSC-183-S+ splitter is also checked by connecting the rf output of microwave source to the splitter. It is a 2 way-0° splitter, so it splits the power input signal equally. Refer to Figure 4.4 for the experimental arrangement.

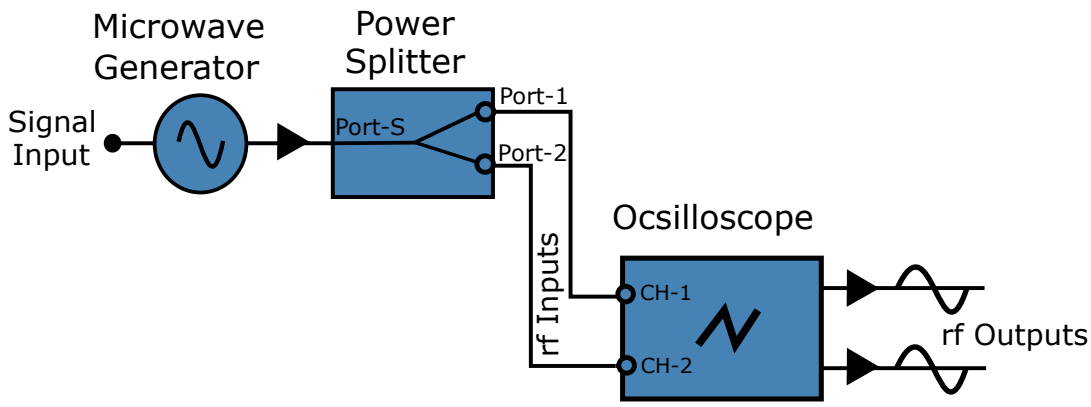

Figure 4.4: Block diagram of an oscilloscope interface showing rf outputs of 254 and 250 mV at port-1 and port-2 of the power splitter, respectively. An rf input signal of 50 MHz and 0 dBm power is applied to the Port-S of power splitter.

The rf output of microwave generator is then connected to a 10 dB 01203-S+ directional coupler. It has two output ports, one is out-port and the other one is cpl-port. The directional coupler increases the senstivity of the FMR system by directing the power coming from the in-port to the out-port and the cpl port. The layout is depicted in Figure 4.5.

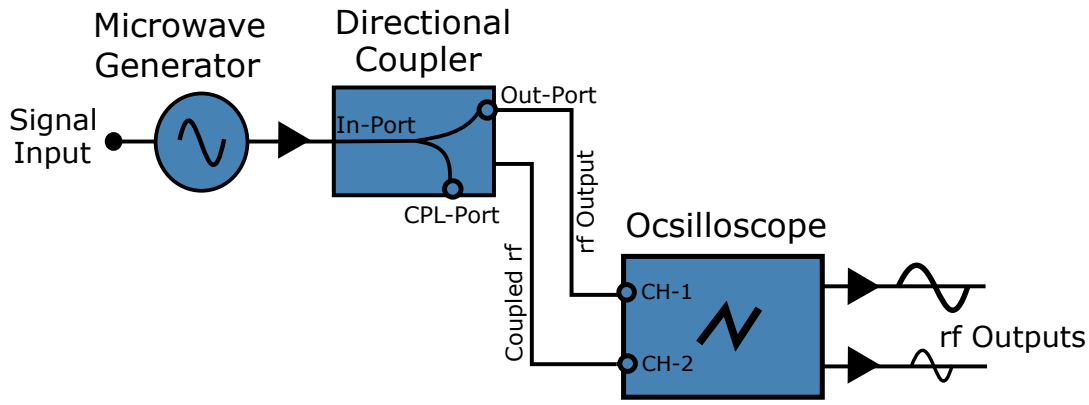

Figure 4.5: Block diagram of an oscilloscope interface showing an rf output of 249.1 mV and coupled rf output of 24.9 mV for a 10 dB directional coupler. An rf input signal of 50 MHz and 0 dBm power is applied to the directional coupler.

The output of ZX47-55-S+ power detectors is also checked which converts the microwave signal coming from the out-port of directional coupler into low frequency dc signal. One thing that's important to mention here is that the rf power detec-

tors have a negative slope which means by increasing the input power the output voltage decreases. The arrangement is shown in Figure 4.6.

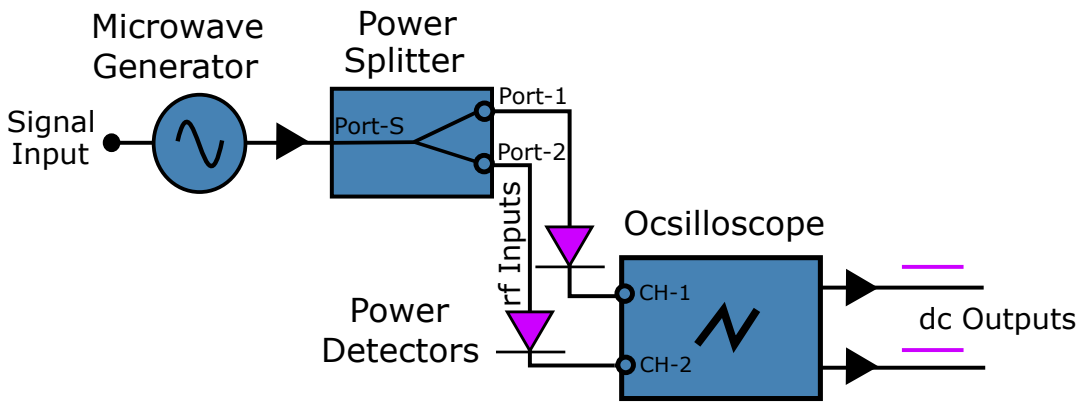

Figure 4.6: Block diagram of an oscilloscope interface showing the dc outputs of 870 mV for two rf power detectors. An rf input signal of 50 MHz and 0 dBm power is applied to the power splitter.

4.2.3 The Experiment Itself

Figure 4.7 shows the experimental setup for an IP field swept LI-FMR spectrometer. A PicoSource AS-108, our broadband microwave generator, generates an rf signal that passes through the Z−line and gives rise to an ac field. The whole DUT is mounted inside a GMW-3470 electromagnet which generates a static dc magnetic field. The DUT has been kept in place with the help of 58 mm long SMA cable holders the drawings of which are shown in Appendix A.3. The key difference is the placement of a pair of Helmholtz coils mounted inside the electromagnet coaxial with the pole pieces to provide an ac field that serves as a source of modulation frequency. The field modulation has been achieved using an RM-AT2500 amplifier which provides current to the Helmholtz coils, and power itself by a power supply. The connection is completed using a capacitor which creates a resonant circuit. With the help of function generator a modulation frequency of 220 Hz is applied to the pair of Helmholtz coils. The same function genera-

tor's sync output is used to provide the reference signal of 220 Hz to the lock-in amplifier's reference input. The combination of current and voltage are set such that the Helmholtz coils produces an ac field of 0.6 mT.

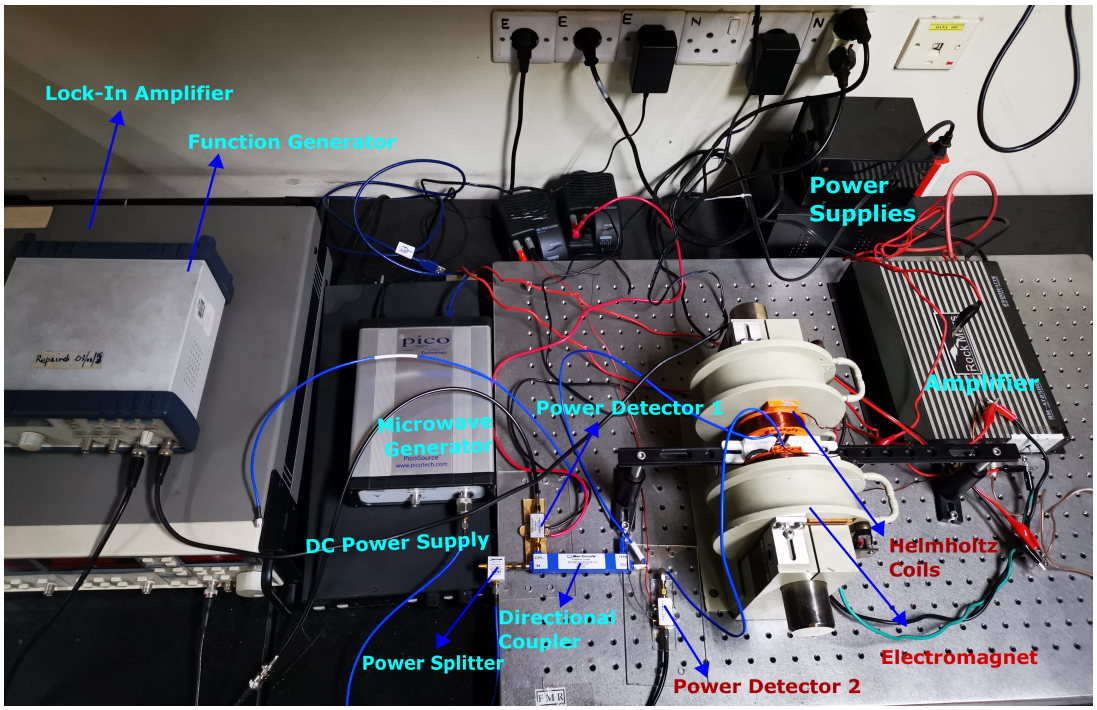

Figure 4.7: Experimental setup of lock-in detection based FMR spectrometer with field sweep technique in IP configuration. The DUT is placed between the electromagnets and a pair of Helmholtz coils. The lock-in amplifier compares the rf microwave signal coming from power detector (D1) and an rf FMR signal coming from power detector (D2) in A-B mode for higher sensitivity.

The microwave generator, generates an rf signal that is fed to the rf power splitter and then the output of power splitter is connected to the directional coupler. The directional coupler basically increases the sensitivity of the signal and takes out -10 dB of the rf signal coming from the power splitter and connects it to the rf detector (D1). The high frequency FMR signal, coming from the DUT can not be fed directly into lock-in amplifier. So, an rf detector (D2) is used to convert the FMR signal into a low-frequency output signal which is within the lockin's accessible frequency range. Let's just recall that ideally an rf detector converts

the microwave signal into low-frequency signal. Both of these signals emerges from D1 and D2 are fed to the lock-in amplifier which operates in the differential mode A-B, where A and B are the inputs of lock-in amplifier.

The FMR response of the sample obtained by lock-in detection is proportional to the first derivative of real part of complex susceptibility as a function of fixed frequency. The field is swept through the stripline and the first derivative is measured at a particular value of applied frequency. This process is repeated a certain times as the applied frequency is swept from 2 to 8 GHz in user defined steps of 0.5 GHz, and by quasi-statically sweeping the field from few a mT to nearly 83.6 mT. Let's see in the next section what we get from all of this.

4.3 Results from the IP LI-FMR Scheme

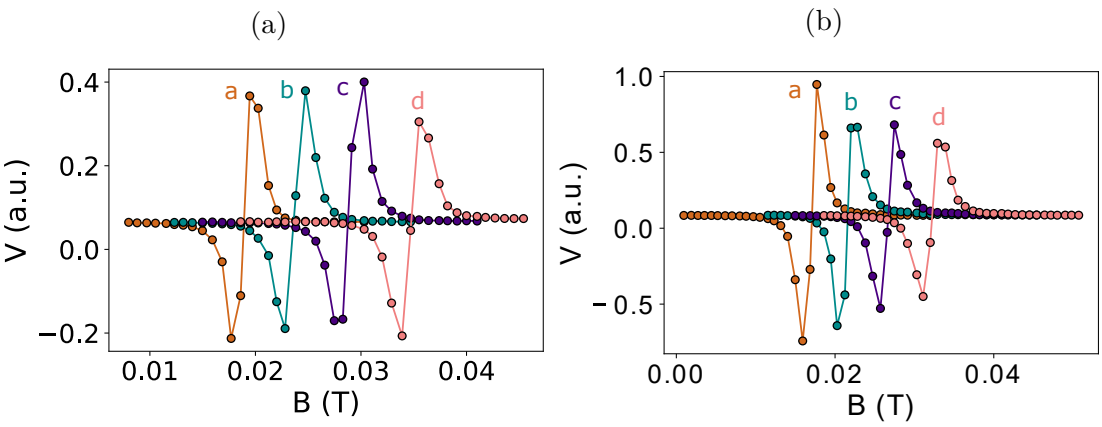

Figure 4.8: Graphs of a specific portion of FMR measurement plotted as a function of external field ($\mathbf{H}_o$) for $S2$ and $S3$ on Z−line for fixed values of frequencies, where $\mathbf{a}$ = 4 GHz, $\mathbf{b}$ = 4.5 GHz, $\mathbf{c}$ = 5 GHz and $\mathbf{d}$ = 5.5 GHz. Solid lines are guide to the eyes.

For the FMR measurements of $S2$, $S3$ and $S4$ with Z−line we fixed the power level to −3 dBm and number of sweep points to 200. A Pyhton script is written

to plot the FMR response of our thin film samples. Figure 4.8 shows the FMR spectra of samples $S2$ and $S3$. We now interpret the results, in the light of forgoing discussion. It is noticeable that varying the applied frequency changes the resonant field. Consequentially, the resonant peaks shifts towards higher magnetic field values as ω_o goes up. A similar result is obtained for the sample $S4$ is shown in Figure 4.9.

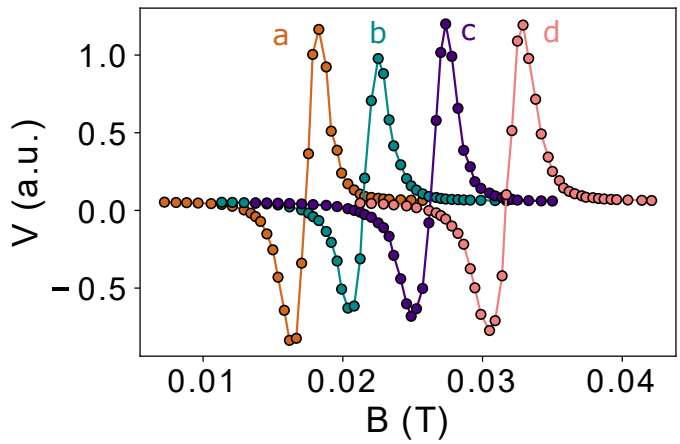

Figure 4.9: Graph of a specific portion of FMR measurement plotted against the external field ($\mathbf{H}_o$) of $S4$ on Z−line for fixed values of frequencies, where **a** = 4 GHz, **b** = 4.5 GHz, **c** = 5 GHz and **d** = 5.5 GHz. Solid lines are guide to the eyes.

From Kittel's Eq. (2.50) we calculated the resonant fields (H_o) of our thin film samples. For the applied microwave frequency range (2 to 8 GHz), the resonant field (H_o) ranges from 0.02 mT to nearly 0.06 mT.

For the LI-FMR measurements we have set a few parameters like the sensitivity of lock-in amplifier to 2.0 mV, time constant to 300 ms, current amplifying scale to 4.0 in order to get the ac field of 6.0 G. All of these parameters are central because changing any of the above mentioned parameters have dramatic effects on FMR response of thin film samples.

We were not able obtain a clear FMR response of sample $S1$ (20 nm NiFe) from frequency swept VNA-FMR scheme but we obtained a clear FMR response of $S1$

with lock-in detection. The FMR response of $S1$ is reproduced in Appendix A.5. This completes our discussion on FMR spectra of different ferromagnetic thin film samples. The next step is parameter extraction based on the methods outlined in Section 3.6.

4.4 Extraction of Measurement Parameters

4.4.1 Resonant Field

In order to extract the resonant fields from FMR measurements of $S2$, $S3$ and $S4$ thin film samples, as illustrated in Figures 4.8 and 4.9, we need to find the maximum and minimum values of each absorption peak. A Python script is written in order to do this task which is reproduced in A.6. This algorithm finds the maximum and minimum values of resonance peak at specific a applied frequency from the FMR data and then finds the central point of these two values. The resonant fields (H_o) of a few absorption peaks are shown in Figures 4.10 and 4.11.

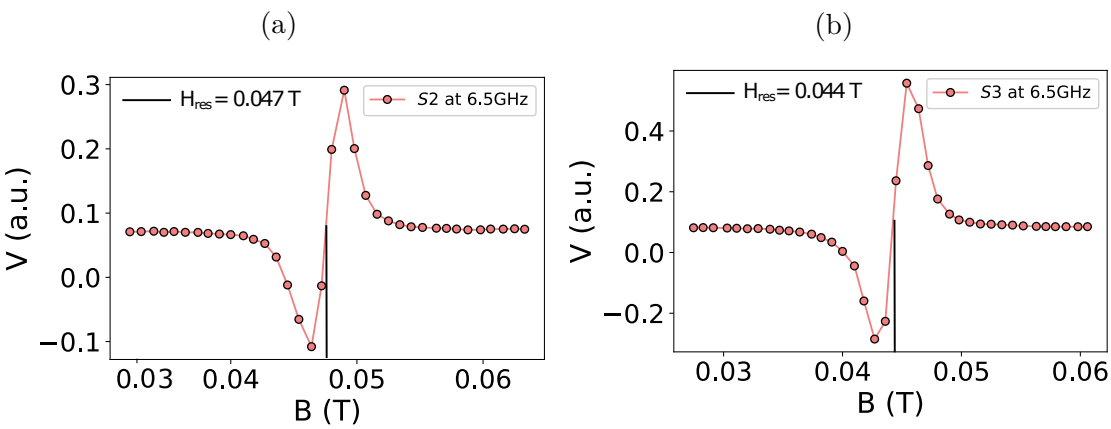

Figure 4.10: Graphs of a specific portion of FMR measurement plotted against external field ($\mathbf{H}_o$) for samples $S2$ and $S3$ in a) and b), respectively. Solid red line represents the resonant field of each peak at 6.5 GHZ.

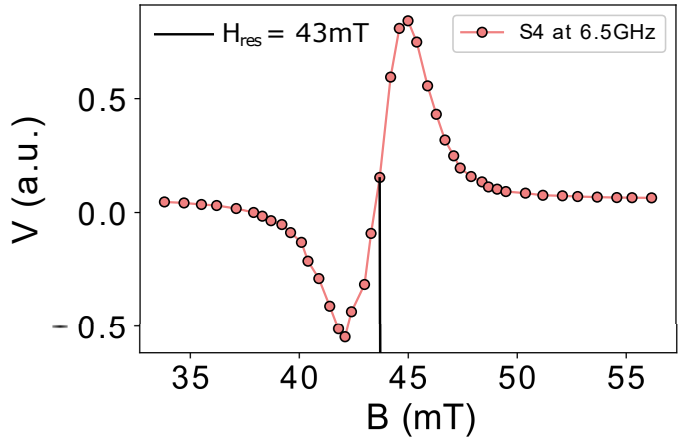

Figure 4.11: Graph of a specific portion of FMR measurement plotted against the external field ($\mathbf{H}_o$) for $S4$ on Z−line for a fixed value of frequency. Red line represents the resonant field of the absorption peak.

4.4.2 Gyromagnetic Ratio and Saturation Magnetization

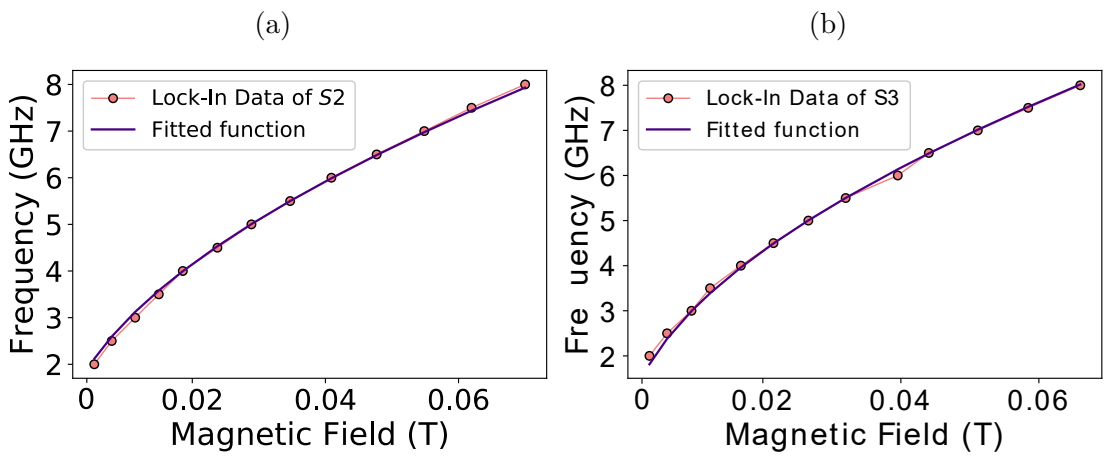

Figure 4.12: Graphs of external field ($\mathbf{H}_o$) as a function of specific frequency ($\omega_o/2\pi$) for $S2$ and $S3$ in IP configuration are shown in a) and b). Solid lines are least square curve fit to the experimental data. The data is fit to Eq. (2.53)

In order to extract the values of gyroamgnetic ratio (γ) and saturation magnetization ($\mathbf{M}_s$) for our thin film samples we've written a Pyhton script which curve fits Kittel's Eq. (2.53) on the FMR data obtained from lock-in amplifier. Fitting

is done using the Optimize library in Python and the code is reproduced in the Appendix A.6.

The extracted value of $\mathbf{M}_s$ is ≈ 1.107 T for all three samples which is in excellent agreement with the reported value and the one we found from VNA-FMR technique. We can use the extracted value of $\mathbf{M}_s$ to calculate the Landé g-factor (g). Similarly, the extracted values of g are found to be: 1.9773, 2.062 and 2.069 for $S2$, $S3$ and $S4$, respectively. These values are in good agreement with the literature value of 2.0–2.14 [61].

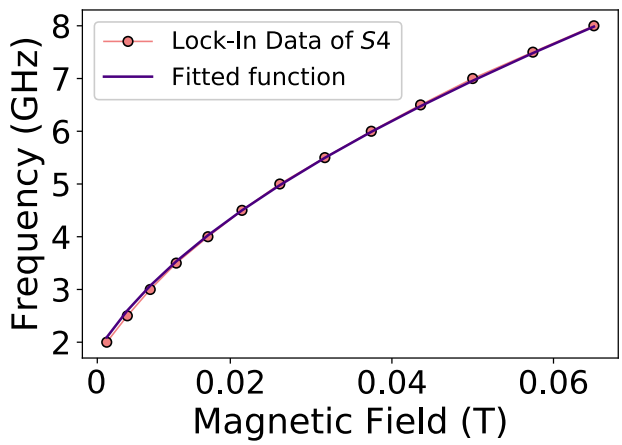

Figure 4.13: Graph of external field ($\mathbf{H}_o$) as a function of specific frequency ($\omega_o/2\pi$) for $S4$ in IP configuration. Solid line is least square curve fit to the experimental data.

The extracted values of gyromagnetic ratio (γ) in GHz T^{-1} are: 27.782, 28.97 and 28.72 for $S2$, $S3$ and $S4$, respectively. It's clear that the extracted values of γ are in good agreement with the values found in literature and VNA-FMR measurements.

4.4.3 Gilbert's Damping Parameter

In order to extract the values of Gilbert's damping parameter (α) for our thin film samples a Python script is written to find the linewidth of each absorption peak.

After extracting the linewidth of each peak, Eq. (3.18) is fitted to the experimental data using a Python script. The algorithms makes use of extracted values of $\mathbf{M}_s$, γ and Eq. (3.18) in order to calculate the values of α and the inhomogeneous line broadening (ΔH_o). Python scripts are reproduced in Appendix A.6. The graphs of resonance frequency vs linewidth (FWHM) for $S2$, $S3$ and $S4$ are shown in Figures 4.14 and 4.15, respectively.

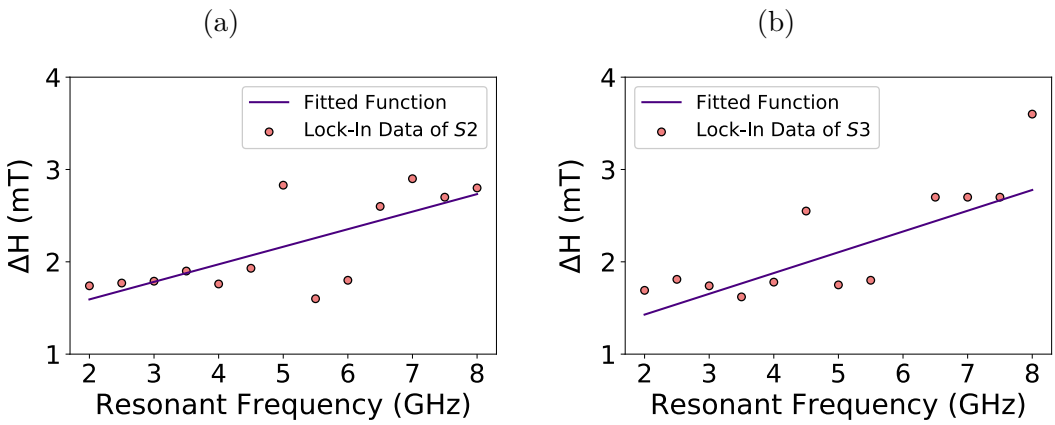

Figure 4.14: Graphs of resonant frequency ($\omega_o/2\pi$) plotted against the linewidth (FWHM) for $S2$ and $S3$ in IP configuration are shown in a) and b). Solid lines are least square curve fit to the experimental data. The data is fit against Eq. (3.18).

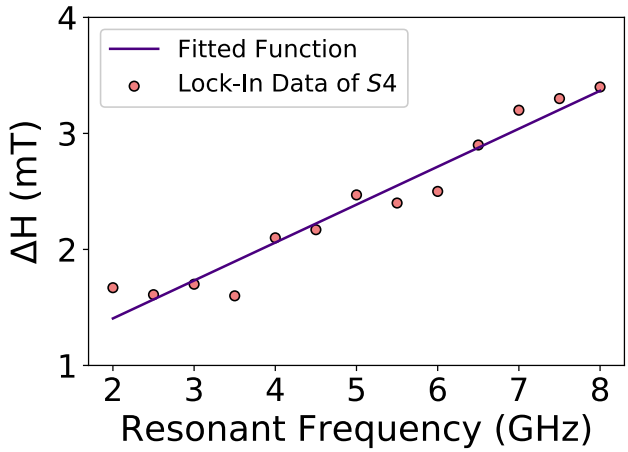

Figure 4.15: Graph of resonant frequency ($\omega_o/2\pi$) plotted against the linewidth (FWHM) for $S4$ in IP configuration. Solid lines are least square curve fit to the experimental data. The data is fit against Eq. (3.18).

The extracted values of Gilbert's damping parameter (α) and inhomogeneous line broadening (ΔH_o) are presented in Table 4.2. As summarized in Table 4.2, ΔH_o is much smaller than the values found in VNA-FMR measurements. The possible reason for this could be the high sensitivity of lock-in detection. Moreover, the values of α are also comparable with the values mentioned in literature 0.003–0.009 [62] and in VNA-FMR measurements.

Table 4.2: Extracted lock-in FMR measurement parameters for IP configuration.

Sample	$\mathbf{M_s}$ (T)	**g**	$\boldsymbol{\gamma}$ (GHz T^{-1})	$\boldsymbol{\alpha}$	ΔH_o (T)
NiFe 49 nm	1.107	1.977	27.782	0.004	0.00121
NiFe 72 nm	1.108	2.062	28.972	0.006	0.00097
NiFe 100 nm	1.107	2.069	28.725	0.007	0.00075

Table 4.2 summarises all the parameters that we've extracted for the different permalloy thin films from LI-FMR technique in IP configuration. We can say that the extracted parameters are in good agreement with established, well known empirical results, validating our experimental technique and measurement protocol.

Chapter 5

Conclusion and Future Outlook

In this chapter we are going to discuss the limitations of our broadband ferromagnetic resonance system. In which we've developed two techniques for the FMR measurements: VNA-FMR technique and lock-in detection. We'll also look at the possible future perspectives for our work.

5.1 Limitations

Frequency swept VNA-FMR measures the FMR response of a sample in IP configuration by sweeping the frequency which generates an rf magnetic field in the stripline. This rf magnetic field along with the static magnetic field excites the magnetic resonance in the sample produced by damped precession of magnetization. For this work we've fabricated several CPWs and a Z-shaped stripline with different critical dimensions. By measuring the transmission properties of CPWs and stripline we can say that the they have reasonable rf response. However, there's no FMR response for permalloy thin film of thickness 20 nm with VNA-FMR technique. The possible reasons for this is the impedance mismatch that created a ripple in the amplitude and lesser sensitivity of this technique.

Field swept lock-in detection technique makes use of very conventional microwave sources like: microwave generator, function generator and rf detectors, all together with a stripline and lock-in amplifier (which serves as a detector) to measure the FMR responses of magnetic samples in a broadband system. Ee got FMR response for permalloy thin film of thickness 20 nm using lock-in detection. The results of which are presented in Appendix *A*.5. In VNA-FMR measurement we can not exceed the upper limit of 6 GHz because of the range of our VNA. Similarly, for lock-in detection this limit is 8 GHz.

5.2 Future Perspectives

To probe the magnetization dynamics in thin films we will certainly continue to use the two techniques that we've developed during the course of this work. To get a more clear FMR response we could decrease the impedance mismatch by tapering the CPWs. In this work VNA-FMR measurements are conducted in the frequency domain, while lock-in detection uses field swept FMR technique. But field swept VNA-FMR and frquency swept lock-in detection is also possible. Both of these setups takes the FMR measurements in IP configuration but are fully capable of taking the FMR measurements in OOP configuration and making a full angle dependent measurement in both IP and OOP configurations.

From the FMR measurements of both techniques we've extracted the important parameters in IP configuration. But we can see there's some difference in the values of gyromagnetic ratio (γ) and inhomogeneous line-broadening (ΔH_o) extracted from the VNA-FMR measurements and lock-in measurements which could be decreased by taking more precise measurements and by decreasing the

bandwidth of VNA. For the FMR response of thin films we can use these setups to investigate the static and dynamic properties of not only permalloy but for other novel magnetic materials also. By doing a field sweep FMR measurement in OOP configuration one could find the field linewidth (ΔH), effective magnetization ($\mathbf{M}_{\mathrm{o}}$), gyromagnetic ratio (γ) and landé g-factor (g) which could also give us some idea about the anisotropy field ($\mathbf{H}_{\mathrm{a}}$). One can also extract the damping parameter (α) in OOP configuration by finding the linewidth ($\Delta\omega$) for frequency and field swept FMR measurements.

Appendices

Appendix A

The First Appendix

A.1 Modulation Amplitudes of Magnetization

If we take **M** and **H** in spherical co-ordinates as

$$\mathbf{M} = M_s(\sin\theta\cos\phi, \sin\theta\sin\phi, \cos\theta), \tag{A.1}$$

$$\mathbf{H} = H(\sin\theta_H\cos\phi_H, \sin\theta_H\sin\phi_H, \cos\theta_H). \tag{A.2}$$

Now, if we consider Eq. (2.57), (A.1) and (A.2) then the total energy of a magnetic system becomes

$$\begin{aligned} E_T &= -K_u\cos^2_\theta + \frac{1}{2}(N_z - N_x)M_s^2 cos^2_\theta - M_s H\big[\sin\theta\cos\phi\sin\theta_H\cos\phi_H \\ &\quad + \sin\theta\sin\phi\sin\theta_H\sin\phi_H + \cos\theta\cos\theta_H\big]. \end{aligned} \tag{A.3}$$

If we take the derivative of Eq. (A.3) w.r.t. θ and ϕ first and then again take the derivative of these two equations w.r.t H_i we get

$$\begin{aligned}\frac{\partial}{\partial H_i}\left(\frac{\partial E}{\partial \theta}\right) &= \big[(K_{\text{eff}} - K_1 \sin^2_\phi) 2\cos 2\theta_o - M_s(-H_x \sin\theta_o \cos\phi_o - H_y \sin\theta_o \\ &\quad \sin\phi_o - H_z \cos\theta)\big]\frac{\partial\theta}{\partial H_i} + \big[-K_1 \sin 2\phi_o \sin 2\theta_o - M_s \cos\theta_o \\ &\quad (-H_x \sin\phi_o + H_y \cos\phi_o)\big]\frac{\partial\phi}{\partial H_i} - M_s(f)\frac{\partial H}{\partial H_i}, \end{aligned} \tag{A.4}$$

$$\begin{aligned}\frac{\partial}{\partial H_i}\left(\frac{\partial E}{\partial \phi}\right) &= \big[K_1 \sin 2\phi_o \cos\theta_o + M_s \cos\theta_o (H_x \sin\phi_o - H_y \cos\phi_o)\big]\frac{\partial\theta}{\partial H_i} \\ &\quad + \big[-2K_1 \sin\theta_o \cos 2\phi_o + M_s \sin\theta_o (H_x \cos\phi_o + H_y \sin\phi_o)\big]\frac{\partial\phi}{\partial H_i} \\ &\quad + M_s(g)\frac{\partial H}{\partial H_i}. \end{aligned} \tag{A.5}$$

In the above equations

$$f = (\cos\theta_o \cos\phi_o, \cos\theta_o \sin\phi_o, -\sin\theta_o), \tag{A.6}$$

$$g = (\sin\theta_o \sin\phi_o, -\sin\theta_o \cos\phi_o, 0). \tag{A.7}$$

Moreover, $\partial E/\partial\theta = 0 = \partial E/\partial\phi$ at equilibrium angles (θ_o, ϕ_o). We can see that Eq. (A.4) and (A.5) are coupled differential equations and can be solved for $\partial\theta/\partial H_i$ and $\partial\phi/\partial H_i$ by taking

$$\mathbf{H} = H_x\hat{i} + H_y\hat{j} + H_z\hat{k}, \tag{A.8}$$

$$\hat{m} = (\sin\theta\cos\phi, \sin\theta\sin\phi, \cos\theta), \tag{A.9}$$

$$H_k = \frac{2K_{\text{eff}}}{M_s}, \tag{A.10}$$

$$H_A = \frac{2K_1}{M_s}. \tag{A.11}$$

we get

$$\frac{\partial\theta}{\partial H_i} = \frac{1}{F_1}(f_i - Cg_i), \tag{A.12}$$

$$\begin{aligned}\frac{\partial\phi}{\partial H_i} &= \frac{1}{F_1F_2}\Big[f_i\big[\frac{1}{2}H_A\sin 2\theta_o\sin 2\phi_o - \cos\theta_o(H_x\sin\phi_o - H_y\sin\phi_o)\big] \\ &\quad -g_i\big[(H_k - H_A\sin^2\phi_o)\cos 2\theta_o + \vec{H}\cdot\hat{m}\big]\Big],\end{aligned} \tag{A.13}$$

where

$$\begin{aligned}F_1 &= (H_k - H_A\sin^2\phi_o)\cos 2\theta_o + \vec{H}\cdot\hat{m} \\ &\quad -C\big[\frac{1}{2}H_A\sin 2\theta_o\sin 2\phi_o - \cos\theta_o(H_x\sin\phi_o - H_y\cos\phi_o)\big],\end{aligned} \tag{A.14}$$

$$F_2 = -H_A\sin^2\theta_o\cos 2\phi_o + (H_x\cos\phi_o + H_y\sin\phi_o)\sin\theta_o, \tag{A.15}$$

$$C = \frac{1}{F_2}\big[\frac{1}{2}H_A\sin 2\phi_o\sin 2\theta_o - \cos\theta_o(H_x\sin\phi_o - H_y\cos\phi_o)\big]. \tag{A.16}$$

Now, we can find the change in the equilibrium angles of magnetization ($\Delta\theta$, $\Delta\phi$) by assuming $|H_A| << |H\sin\theta_H|$ and $\phi_o = \phi_H$ and taking

$$\Delta\theta = \frac{\partial\theta}{\partial H_x}\Delta H_x + \frac{\partial\theta}{\partial H_y}\Delta H_y + \frac{\partial\theta}{\partial H_z}\Delta H_z, \tag{A.17}$$

$$\Delta\phi = \frac{\partial\phi}{\partial H_x}\Delta H_x + \frac{\partial\phi}{\partial H_y}\Delta H_y + \frac{\partial\phi}{\partial H_z}\Delta H_z. \tag{A.18}$$

If we put Eq. (A.12) and (A.13) in Eq. (A.17) and (A.18) respectively we get

$$\Delta\theta = \frac{\cos\theta_o(\Delta H_x\cos\phi_H + \Delta H_y\sin\phi_H) - \sin\theta_o\Delta H_z}{(H_k - H_A\sin^2\phi_o)\cos 2\theta_o + H\cos(\theta_H - \theta_o)}, \tag{A.19}$$

$$\Delta\phi = \frac{-\Delta H_x\sin\phi_H + \Delta H_y\cos\phi_H}{-H_A\sin\theta_o\cos 2\phi_H + H\sin\theta_H}. \tag{A.20}$$

So, Eq. (A.19) and (A.20) represent the modulation amplitudes of magnetization angles [67].

A.2 Few Words on Spin Orbit Torque

Spin-orbit-torque (SOT) is used to label phenomena associated to changes of magnetization state induced by spin polarised currents. When an electric current passes through some magnetically polarized material, it will in general exhibit some finite spin polarization. Now, if this current passes through an area where the state of magnetization corresponds to a different orientation of spin polarization, then somehow the carriers have to adopt this orientation. Because of which there will be a change in spin expectation value (polarization/orientation).

We're considering different magnetization states in a material as given, and their role is to impose the boundary conditions to which the carriers have to adopt. But in reaction there will be an effect on the polarization state of magnetic material, which is called "Spin-Transfer-Torque". Whereas, in general both spin-transfer-torque and spin-orbit-torque happen when non-equilibrium spin density is not collinear to the direction of magnetization. The torque is non-zero only when two vectors are non-collinear. Depending on the strength of non-equilibrium spin density compared to magnetization, we can have alignment of spins with magnetization (spin is large).

The difference between spin-transfer-torque (STT) and spin-orbit-torque resides in the origin of spin density. In spin-transfer-torque, the spin density originates from the polarization by ferromagnetic layer. Whereas, in spin-orbit-torque the spin density originates from spin-orbit coupling which favours the direction of

spin angular momentum in a particular region of space. When current is passed through a sample there is a induced magnetic field with oersted field, which tends to change the equilibrium angle of magnetization (θ_o, ϕ_o). The sample geometry, equilibrium magnetization **M** and applied magnetic field **H** is shown in Figure 2.6.

A.3 SMA Cable Holder Drawing

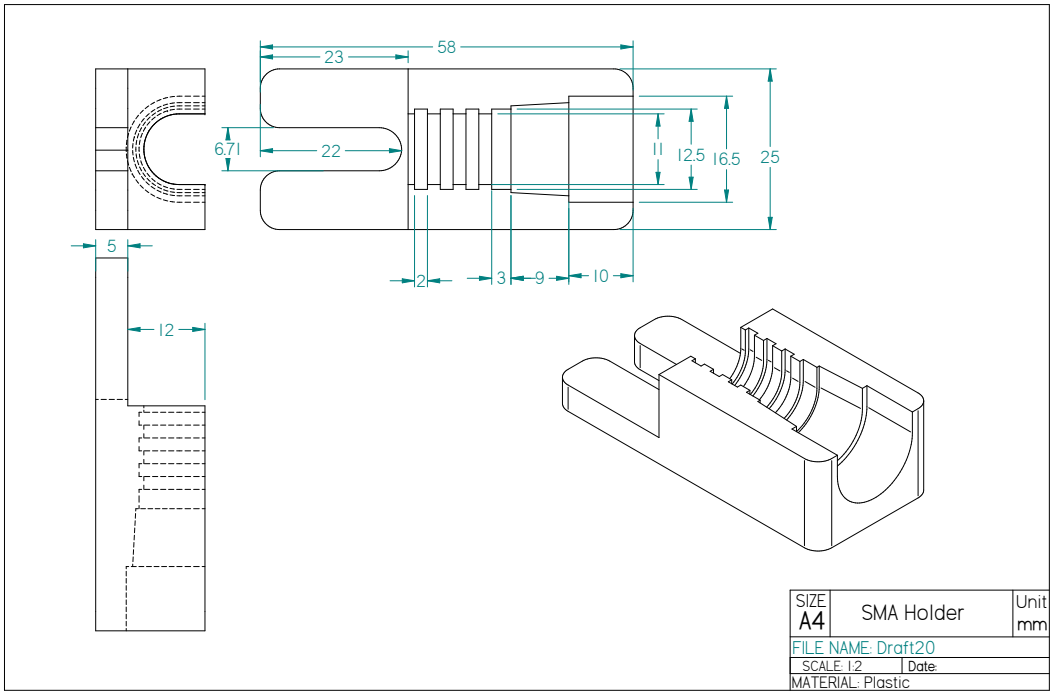

Figure A.1: Drawings of 58 mm SMA cable holders. All the dimensions are in millimeters.

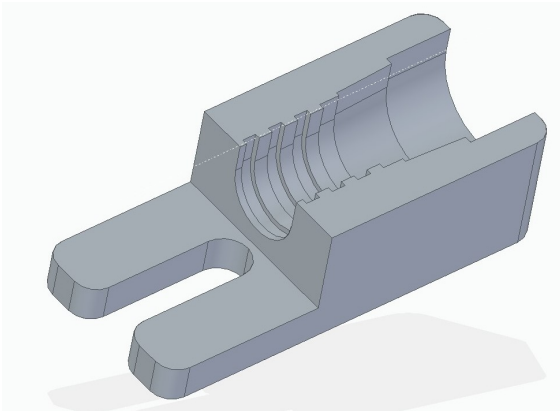

Figure A.2: Design of 58 mm SMA cable holders.

A.4 LabView Interface for FMR Setup

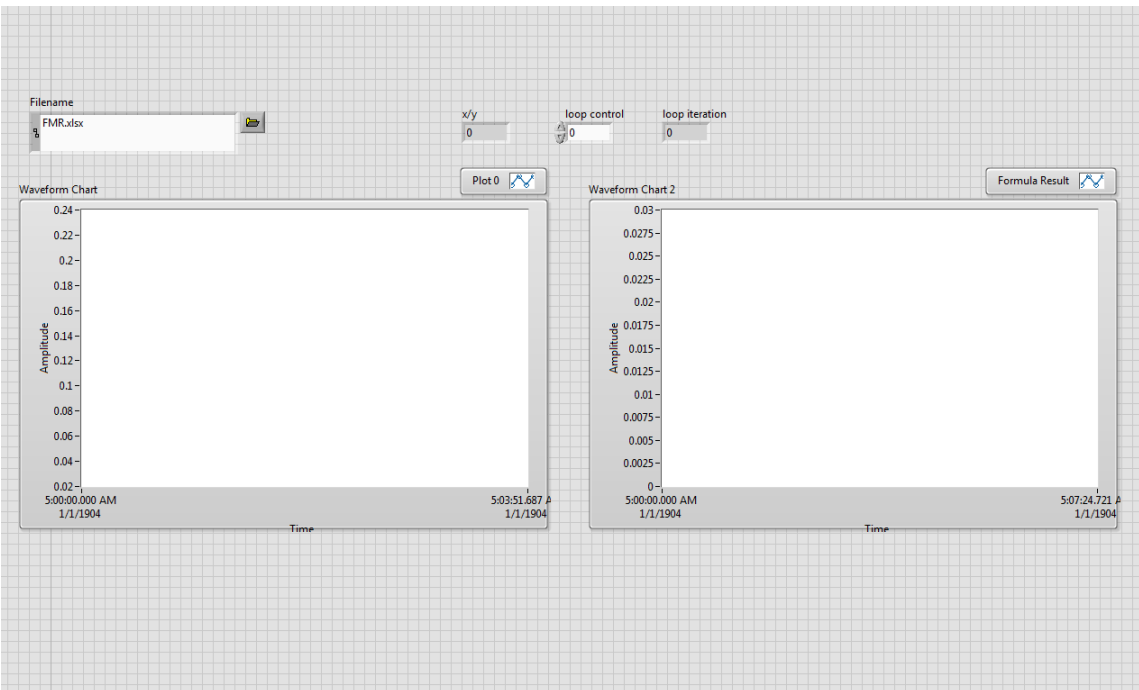

Figure A.3: Front panel of FMR Setup visualized in LabView. The graphical VI's displays the output voltages from lock-in channels (X and Y), whereas the current tab controls the input current of power supply.

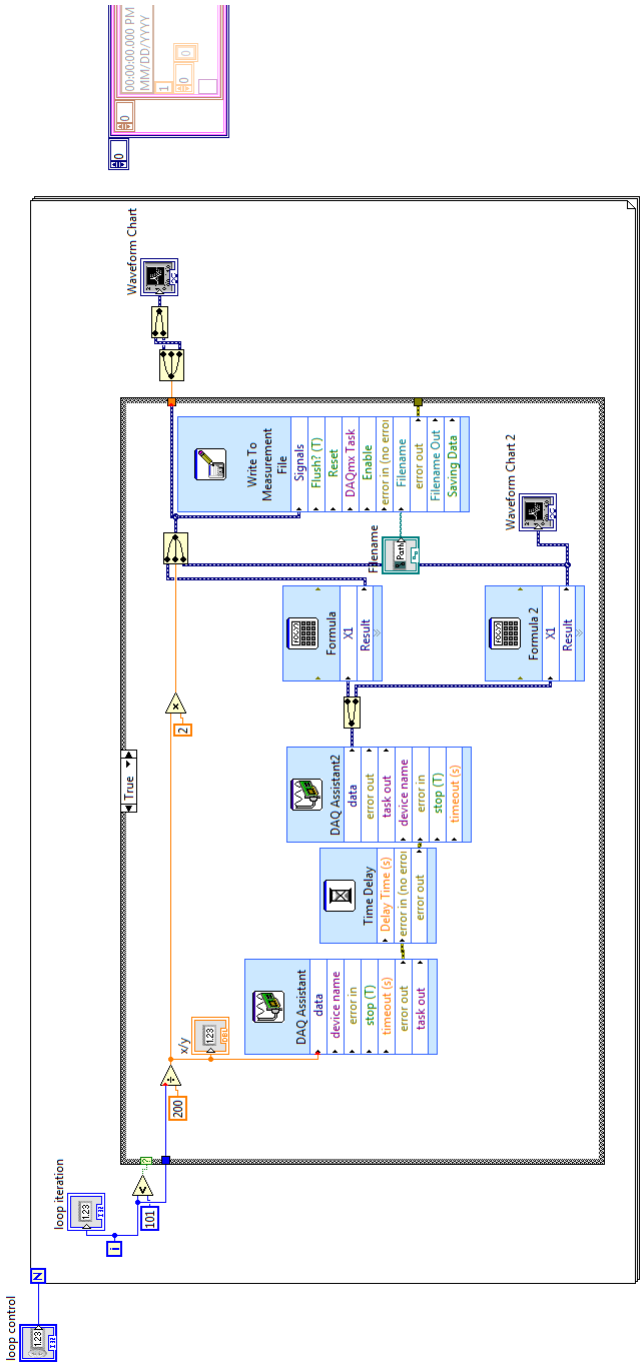

Figure A.4: Block diagram of virtual elements of LabView program for FMR setup. Where **DAQ Assistant** = data acquisition, **loop iterations** controls the input current of power supply and **write to measurement** = element for storing data.

A.5 FMR Spectrum of S1 with Lock-In Detection

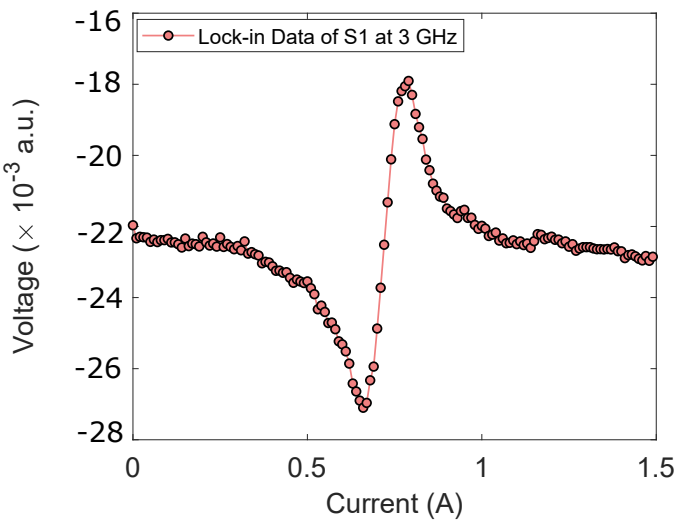

Figure A.5: Graph of a specific portion of FMR measurement plotted against the resonant field ($\mathbf{H}_o$) for $S1$ on Z−line for fixed values of frequencies.

A.6 FMR Source Codes

A.6.1 Matlab Script for Data Extraction

```
clear all

for i=1:3
    p=1;
    for k=1:26
        FA=fopen(['D:\Basit\Lums\3rd Semester (In Sha
           Allah both acha)\Research\VNA\22-06-21\'
```

```
            num2str(1) 'th Measurement/cpw_' num2str(k) '.
            s2p']);
        B=fscanf(FA,'%c');
        D=regexp(B, '[\n]');
        B=B(D(4):end);
        B=split(B,' ');
        emptyCells = cellfun('isempty', B);
        B(all(emptyCells,2),:) = [];
        B(end)=[];

        for n=1:length(B)
            S(n)=str2num(B{n});
        end
        B=S;
        B=reshape(B,[9,512]);
        B=B';
         Real_0(p).a=B(:,4);%Reads the Real part
        Imag_0(p).a=B(:,5);%Reads the imaginary part
        Freqq=B(:,1);%Reads the frequency coulomn
        p=p+1;
    end

    for w=2:26
        Diff_real(w-1).a=Real_0(w).a-Real_0(26).a;
%Take Differential
        Diff_imag(w-1).a=Imag_0(w).a-Imag_0(26).a;
```

```
    end

    for v=2:26
        Div_real(v-1).a=Real_0(w).a./Real_0(26).a;
        Div_imag(v-1).a=Imag_0(w).a./Imag_0(26).a;
    end
end

R0=(Real_0(1).a); %To change the file that contains whole data
I0=(Imag_0(1).a);
R1=(Real_0(2).a); %To change the file that contains whole data
I1=(Imag_0(2).a);
R2=(Real_0(3).a); %To change the file that contains whole data
I2=(Imag_0(3).a);
R3=(Real_0(4).a); %To change the file that contains whole data
I3=(Imag_0(4).a);
R4=(Real_0(5).a); %To change the file that contains whole data
I4=(Imag_0(5).a);


```

```
R00=Diff_real(19).a; %To change the file that takes differential
I00=Diff_imag(19).a;
R11=Diff_real(20).a; %To change the file that takes differential
I11=Diff_imag(20).a;
R22=Diff_real(21).a; %To change the file that takes differential
I22=Diff_imag(21).a;
R33=Diff_real(22).a; %To change the file that takes differential
I33=Diff_imag(22).a;
R44=Diff_real(23).a; %To change the file that takes differential
I44=Diff_imag(23).a;
figure
plot(Freqq,R00,'b-')
hold on
plot(Freqq,R11,'r-')
hold on
plot(Freqq,R22,'y-')
 hold on
plot(Freqq,R33,'g-')
hold on
plot(Freqq,R44,'k-')
```

```
lgd=legend('.453mT WS- 74.6mT WS','1.353mT WS- 74.6mT WS'
    ,'2.160mT WS - 74.6mT WS','3.08mT WS - 74.6mT WS');
lgd.FontSize=14;
hold off
xlabel('Frequency (MHz)','FontSize',18);
ylabel('Real part of dS_{21} (X 10^{-3} dB)','FontSize'
    ,18);
axis([3.609375000000000e+03 4.804687500000000e+03 -10e-03
     1e-03])

[a,b]=find(Freqq==4207.031300);
[c,d]=find(Freqq==4710.9375000);
kkk=Diff_real(24).a(a:c,1);
PPP=abs(kkk);
OOO=Diff_imag(24).a(a:c,1);
III=R1(a:c,1);
UUU=I1(a:c,1);
FFF=Freqq(a:c,1);
figure
plot(FFF,PPP, 'b*')% Plotting a specific FMR Peak
xlabel('Frequency (MHz)')
ylabel('Real part of dS_{21} (arb.units)')
title('Specific Diff Real part at 3(1) A Field')
figure
plot(FFF,OOO, 'mo')
xlabel('Frequency (MHz)')
```

```
ylabel('Imag part of dS_{21} (arb.units)')
title('Specific Diff Imag part at 3(1) A Field')
% Finding the line-width of specific curve
halfMax = (min(PPP) + max(PPP))/2;
index1 = find(PPP >= halfMax, 1, 'first');
index2 = find(PPP >= halfMax, 1, 'last');
fwhmx = Freqq(index2) - Freqq(index1);
```

A.6.2 Python Scripts for Extraction of Measurement Parameters

```
#Source code for the curve fitting of FMR Peak
from scipy import optimize
import numpy as np
import matplotlib.pyplot as pl
curblist=np.array([0,0,0,0,-0.0000999999999999890,..])
cuiblist=np.array
   ([-0.0399999999999992,-0.0499999999999972,...])
b1list=np.array([3890.625,3902.3438,...])
#N=2*np.pi
#FIlist=np.array([x*N for x in FIlist])
def Sxx1(omega,del_omega,H_not):
#    del_omega=714.8437*10**6
    gamma=28*10**7.8
    M_s=1.107825
    mew_not=12.56*10**-7
#    H_not=4477
```

```
    omega_rs=mew_not*gamma*H_not
    omega_m=mew_not*gamma*M_s
    SxxR=(omega_m*((gamma*mew_not*H_not)*(omega_rs**2-omega**2)+(omega*del_omega**2)))/((omega_rs**2-omega**2)**2+(omega*del_omega)**2)
    return SxxR
def Sxx2(omega,del_omega,H_not):
#    del_omega=714.8437*10**6
    gamma=28*10**7.8
    M_s=1.10782
    mew_not=12.56*10**-7
#    H_not=4477
    omega_rs=mew_not*gamma*H_not
    omega_m=mew_not*gamma*M_s
    SxxI=((omega_m*del_omega)*((gamma*mew_not*H_not*omega)-(omega_rs**2-omega**2)))/((omega_rs**2-omega**2)**2+(omega*del_omega)**2)
    return SxxI
def dffR(omega,del_omega,H_not,H):
    dff1=(Sxx1(omega,del_omega,H_not+H)-(Sxx1(omega,del_omega,H_not-H)))/H
    return dff1
def dffI(omega,del_omega,H_not,H):
    dff2=(Sxx2(omega,del_omega,H_not+H)-(Sxx2(omega,del_omega,H_not-H)))/H
    return dff2
```

```
def s21R(omega,del_omega,H_not,H,A):
    ds21R=A*omega*dffI(omega,del_omega,H_not,H)
    return ds21R
def s21I(omega,del_omega,H_not,H,A):
    ds21I=A*omega*dffR(omega,del_omega,H_not,H)
    return ds21I
params, params_covariance = optimize.curve_fit(s21R,
    b1list, curblist, p0=[1,1,1,1], maxfev=25000)
print(params)
pl.figure(2)
pl.plot(b1list,curblist,label="VNA Data: 49nm NiFe",
    linestyle='--',marker='*')
pl.plot(b1list,s21R(b1list, params[0], params[1], params
    [2], params[3]), label='Fitted Function')
pl.xlabel('Frequency (GHz)', fontsize=20)
pl.ylabel('Real $S_{21}$ (arb. units)', fontsize=20)
pl.xticks([4007.8125,4207.0313,...],["4.0","4.2","4.4","
    4.6","4.8","5.0"])
pl.rc('xtick', labelsize=18)
pl.rc('ytick', labelsize=18)
pl.legend(loc='lower right', prop={"size":15})
#pl.savefig("fvss21R42nmNiFe.eps",bbox_inches='tight',dpi
    =600)
params, params_covariance = optimize.curve_fit(s21I,
    b1list, cuiblist, p0=[1,1,1,1], maxfev=25000)
print(params)
```

```
pl.figure(3)
pl.plot(b1list,cuiblist,label="VNA Data: 49nm NiFe",
    linestyle='--',marker='*')
pl.plot(b1list,s21I(b1list, params[0], params[1], params
    [2], params[3]), label='Fitted Function')
pl.xlabel('Frequency (GHz)', fontsize=20)
pl.ylabel('Imaginary $S_{21}$ (arb. units)', fontsize=20)
pl.rc('xtick', labelsize=18)
pl.rc('ytick', labelsize=18)
pl.xticks([4007.8125,4207.0313,...],["4.0","4.2","4.4","
    4.6","4.8","5.0"])
pl.legend(loc='lower right', prop={"size":15})
pl.savefig("fvss21I42nmNiFe.eps",bbox_inches='tight',dpi
    =600)
#Ip busf curve fitting for 100nm-NiFe
HIlist=np.array
    ([0.000453,0.001353,0.002160,0.00308,0.00398,...])
FIlist=np.array([984.4*10**6,1055*10**6,...])
def KITI(H,g):
#    M=1.107825
#    g=0.33217689
    mew_b=9.27*10**-24
    h_bar=1.056*10**-34
    gamma=(mew_b*g)/h_bar
    omega= (gamma)*(H*(H+M))**0.5
    return omega
```

```
77 params, params_covariance = optimize.curve_fit(KITI,
      HIlist, FIlist, p0=[1], maxfev=25000)
78 print(params)
79 pl.figure(3)
80 pl.plot(HIlist,FIlist,label="VNA Data: 100nm NiFe",
      linestyle=':',marker='*')
81 pl.plot(HIlist,KITI(HIlist, params[0]), label='Fitted
      function')
82 pl.xlabel('Magnetic Field (mT)', fontsize=20)
83 pl.ylabel('Frequency (GHz)', fontsize=20)
84 pl.xticks([0.000453,0.00570,..],["0.4","5",..])
85 pl.yticks([984.4*10**6,..],["0.5","1.5",..])
86 pl.rc('xtick', labelsize=18)
87 pl.rc('ytick', labelsize=18)
88 pl.legend(loc='best', prop={"size":15})
89 pl.savefig("bvsf100nmNiFe.eps",bbox_inches='tight',dpi
      =600)
90 #Ip fvsfwhm curve fitting 100nm-NiFe
91 FWHMlist=np.array([410.1562*10**6,375*10**6,...])
92 FIlist=np.array([1570*10**6,1840*10**6,...])
93 def WI(omega,alpha,del_H):
94     gamma=28*10**9
95     M_s=1.014109
96 #    del_H=0.034
97     W_IP=(((2*alpha*(2*np.pi*omega))+(gamma*del_H))
          *((1+((gamma*M_s)/(2*(2*np.pi*omega)))**2)**0.5))
```

```
        /(2*np.pi)
    return W_IP
params, params_covariance = optimize.curve_fit(WI, FIlist, FWHMlist, p0=[1,1], maxfev=25000)
print(params)
pl.figure(3)
pl.scatter(FIlist,FWHMlist,label="VNA Data:100nm NiFe", linestyle=':',marker='*')
pl.plot(FIlist,WI(FIlist, params[0], params[1]), label='Fitted Function')
pl.xlabel('Resonant Frequency (GHz)', fontsize=20)
pl.ylabel('FWHM (Hz)', fontsize=20)
pl.xticks([1559*10**6,2027*10**6,..],["1.5","2.0",..])
pl.rc('xtick', labelsize=18)
pl.rc('ytick', labelsize=18)
pl.legend(loc='best', prop={"size":15})
pl.savefig("fvsfwhm100nmNiFe.eps",bbox_inches='tight',dpi=600)
#Resonant field for Lock-in amplifier Measurements
freqqlist=np.array([2,2.5,3,3.5,4,4.5,5,5.5,6,6.5,7,7.5,8])
N=10**9
freqlist=np.array([x*N for x in freqqlist])
del_Hlist=np.array([0.00174,0.00177,0.00179,0.0019,..])
def WI(omega,alpha,del_Ho):
    gamma=27*10**9
```

```
#     del_Ho=0.001691
    del_H=del_Ho+((2*alpha*omega)/(gamma*(3)**0.5))
    return del_H
params, params_covariance = optimize.curve_fit(WI,
   freqlist, del_Hlist, p0=[1,1], maxfev=25000)
print(params)
pl.figure(4)
pl.scatter(freqlist,del_Hlist,label="Lock-In Data: 49nm
   NiFe",linestyle=':',marker='*')
pl.plot(freqlist,WI(freqlist, params[0], params[1]),
   label='Fitted Function')
pl.xlabel('Resonant Frequency (GHz)', fontsize=22)
pl.ylabel('FWHM (mT)', fontsize=22)
pl.xticks([2*10**9,3*10**9,..],["2","3",..])
#pl.xticks([0.00174,0.00179,..],["1.74","1.79",.])
pl.rc('xtick', labelsize=20)
pl.rc('ytick', labelsize=20)
pl.legend(loc='best', prop={"size":15})
pl.ylim(0.001, 0.004)
#pl.savefig("fvsfwhm49nmNiFelockin.jpg",dpi=600)
pl.savefig("fvsfwhm49nmNiFelockin.eps",bbox_inches='tight
   ',dpi=600)
```

Bibliography

[1] J. H. Griffiths, "Anomalous High-Frequency Resistance of Ferromagnetic Metals," *Nature*, vol. 158, no. 4019, pp. 670–671, 1946.

[2] C. Kittel, J. Galt, and W. Campbell, "Crucial Experiment Demonstrating Single Domain Property of Fine Ferromagnetic Powders," *Physical Review*, vol. 77, no. 5, p. 725, 1950.

[3] J. Martın, J. Nogues, K. Liu, J. Vicent, and I. K. Schuller, "Ordered Magnetic Nanostructures: Fabrication and Properties," *Journal of magnetism and magnetic materials*, vol. 256, no. 1-3, pp. 449–501, 2003.

[4] S. O. Demokritov and B. Hillebrands, "Spinwaves in Laterally Confined Magnetic Structures," *Spin Dynamics in Confined Magnetic Structures I*, pp. 65–92, 2002.

[5] A. Thiaville and Y. Nakatani, "Domain-Wall Dynamics in Nanowiresand Nanostrips," *Spin dynamics in confined magnetic structures III*, pp. 161–205, 2006.

[6] N. Vukadinovic, "High-Frequency Response of Nanostructured Magnetic Materials," *Journal of magnetism and magnetic materials*, vol. 321, no. 14, pp. 2074–2081, 2009.

[7] C. Heck, *Magnetic Materials and their Applications.* Elsevier, 2013.

[8] L. R. Walker, "Magnetostatic Modes in Ferromagnetic Resonance," *Physical Review*, vol. 105, no. 2, p. 390, 1957.

[9] N. Cramer, D. Lucic, R. Camley, and Z. Celinski, "High Attenuation Tunable Microwave Notch Filters Utilizing Ferromagnetic Resonance," *Journal of Applied Physics*, vol. 87, no. 9, pp. 6911–6913, 2000.

[10] M. Kostylev, A. Serga, T. Schneider, B. Leven, and B. Hillebrands, "Spin-Wave Logical Gates," *Applied Physics Letters*, vol. 87, no. 15, p. 153501, 2005.

[11] J. S. Ward and A. Barker, "Undefined By Data: A Survey of Big Data Definitions," *arXiv preprint arXiv:1309.5821*, 2013.

[12] A. Ney, C. Pampuch, R. Koch, and K. Ploog, "Programmable Computing with a Single Magnetoresistive Element," *Nature*, vol. 425, no. 6957, pp. 485–487, 2003.

[13] D. Apalkov, B. Dieny, and J. Slaughter, "Magnetoresistive Random Access Memory," *Proceedings of the IEEE*, vol. 104, no. 10, pp. 1796–1830, 2016.

[14] E. Grochowski and R. D. Halem, "Technological Impact of Magnetic Hard Disk Drives on Storage Systems," *IBM Systems Journal*, vol. 42, no. 2, pp. 338–346, 2003.

[15] E. Luo, S. Wong, A. Pakhomov, J. Xu, I. Wilson, and C. Wong, "Tunneling Current and Thickness Inhomogeneities of Ultrathin Aluminum Oxide Films in Magnetic Tunneling Junctions," *Journal of Applied Physics*, vol. 90, no. 10, pp. 5202–5207, 2001.

[16] J. C. Mallinson, *Magneto-Resistive and Spin Valve Heads: Fundamentals and Applications*. Elsevier, 2001.

[17] G. A. Prinz, "Magnetoelectronics," *Science*, vol. 282, no. 5394, pp. 1660–1663, 1998.

[18] L. A. C. Diaz, *Growth by Chemical Beam Epitaxy and Characterization of (Gallium, Manganese) Nitrogen*. University of Houston, 2004.

[19] A. Kehlberger, U. Ritzmann, D. Hinzke, E.-J. Guo, J. Cramer, G. Jakob, M. C. Onbasli, D. H. Kim, C. A. Ross, M. B. Jungfleisch, *et al.*, "Length Ccale of the Spin Seebeck Effect," *Physical review letters*, vol. 115, no. 9, p. 096602, 2015.

[20] A. Hoffmann and S. D. Bader, "Opportunities at the Frontiers of Spintronics," *Physical Review Applied*, vol. 4, no. 4, p. 047001, 2015.

[21] A. Goldman, *Handbook of Modern Ferromagnetic Materials*, vol. 505. Springer Science & Business Media, 2012.

[22] T. L. Gilbert, "A Phenomenological Theory of Damping in Ferromagnetic Materials," *IEEE transactions on magnetics*, vol. 40, no. 6, pp. 3443–3449, 2004.

[23] D. Allwood, G. Xiong, M. Cooke, and R. Cowburn, "Magneto-Optical Kerr effect Analysis of Magnetic Nanostructures," *Journal of Physics D: Applied Physics*, vol. 36, no. 18, p. 2175, 2003.

[24] J. Stöhr, "X-ray Magnetic Circular Dichroism Spectroscopy of Transition Metal Thin Films," *Journal of Electron Spectroscopy and Related Phenomena*, vol. 75, pp. 253–272, 1995.

[25] S. Foner, "The Vibrating Sample Magnetometer: Experiences of a Volunteer," *Journal of applied physics*, vol. 79, no. 8, pp. 4740–4745, 1996.

[26] S. Foner, "High-Field Antiferromagnetic Resonance in Cr 2 O 3," *Physical Review*, vol. 130, no. 1, p. 183, 1963.

[27] S. S. Kalarickal, P. Krivosik, M. Wu, C. E. Patton, M. L. Schneider, P. Kabos, T. J. Silva, and J. P. Nibarger, "Ferromagnetic Resonance Linewidth in Metallic Thin Films: Comparison of Measurement Methods," *Journal of Applied Physics*, vol. 99, no. 9, p. 093909, 2006.

[28] A. Aharoni *et al.*, *Introduction to the Theory of Ferromagnetism*, vol. 109. Clarendon Press, 2000.

[29] C. Kittel, "Physical Theory of Ferromagnetic Domains," *Reviews of modern Physics*, vol. 21, no. 4, p. 541, 1949.

[30] S. M. Rezende, *Fundamentals of Magnonics*, vol. 969. Springer, 2020.

[31] P. W. Atkins and R. S. Friedman, *Molecular Quantum Mechanics*. Oxford university press, 2011.

[32] W. Demtröder, *Atoms, Molecules and Photons*, vol. 3. Springer, 2010.

[33] N. A. Spaldin, *Magnetic Materials: Fundamentals and Applications*. Cambridge university press, 2010.

[34] M. Boufligha and S. Boukhtache, "A Simultaneous Solution of the Gilbert Equation and its Equivalent Landau-Lifshitz-Gilbert Equation," *Advances in Modelling and Analysis D*, vol. 21, no. 1, 2016.

[35] M. Lakshmanan, "The Fascinating World of the Landau–Lifshitz–Gilbert Equation: an Overview," *Philosophical Transactions of the Royal Society A: Mathematical, Physical and Engineering Sciences*, vol. 369, no. 1939, pp. 1280–1300, 2011.

[36] E. Olive, Y. Lansac, M. Meyer, M. Hayoun, and J.-E. Wegrowe, "Deviation from the Landau-Lifshitz-Gilbert Equation in the Inertial Regime of the Magnetization," *Journal of Applied Physics*, vol. 117, no. 21, p. 213904, 2015.

[37] B. D. Cullity and C. D. Graham, *Introduction to Magnetic Materials.* John Wiley & Sons, 2011.

[38] *Spin Currents and Ferromagnetic Resonance in Magnetic Thin Films, author=Ellsworth, David.* PhD thesis, Colorado State University, 2017.

[39] D. M. Pozar, *Microwave Engineering.* John wiley & sons, 2009.

[40] C. Kittel, "Ferromagnetic Resonance," 1951.

[41] B. Kuanr, R. Camley, and Z. Celinski, "Effect of Shape Anisotropy on Stop-Band Response of Fe and Permalloy Based Tunable Microstrip Filters," *IEEE transactions on magnetics*, vol. 40, no. 4, pp. 2841–2843, 2004.

[42] J. M. Coey, *Magnetism and Magnetic Materials.* Cambridge university press, 2010.

[43] A. Riegler, *Ferromagnetic Resonance Study of the Half-Heusler Alloy NiMnSb: The Benefit of Using NiMnSb as a Ferromagnetic Layer in Pseudo-Spin-Valve based Spin-Torque Oscillators.* PhD thesis, Universität Würzburg, 2011.

[44] S. N. Karmakar, S. K. Maiti, and C. Jayeeta, *Physics of Zero-and One-Dimensional Nanoscopic Systems*, vol. 156. Springer Science & Business Media, 2007.

[45] B. Goodman and P. Hall, "Electron Paramagnetic Resonance Spectroscopy," in *Clay Mineralogy: spectroscopic and chemical determinative methods*, pp. 173–225, Springer, 1994.

[46] R. K. Harris, "Nuclear Magnetic Resonance Spectroscopy," 1986.

[47] J. Smith, "Nuclear Quadrupole Resonance Spectroscopy. General Principles," *Journal of Chemical Education*, vol. 48, no. 1, p. 39, 1971.

[48] N. M. Atherton, M. Davies, and B. Gilbert, *Electron Spin Resonance*, vol. 14. Royal Society of Chemistry, 1994.

[49] J. A. Weil and J. R. Bolton, *Electron Paramagnetic Resonance: Elementary Theory and Practical Applications*. John Wiley & Sons, 2007.

[50] G. T. Rado and J. R. Weertman, "Spin-Wave Resonance in a Ferromagnetic Metal," *Journal of Physics and chemistry of solids*, vol. 11, no. 3-4, pp. 315–333, 1959.

[51] A. Akbar, *Some Explorations in Magneto-Optics and Opto-Magnetics*. PhD thesis, Lahore University of Management Sciences, 2020.

[52] Z. Qiu, J. Pearson, and S. Bader, "Asymmetry of the Spin Reorientation Transition in Ultrathin Fe Films and Wedges Grown on Ag (100)," *Physical Review Letters*, vol. 70, no. 7, p. 1006, 1993.

[53] T. C. Oakberg, "Magneto-Optic Kerr Effect," *Hinds Instruments*, vol. 1, no. 1, 2005.

[54] R. N. Simons, *Coplanar Waveguide Circuits, Components, and Systems*, vol. 165. John Wiley & Sons, 2004.

[55] S. Holladay, "Frequency-Swept Ferromagnetic Resonance Characterization of Permalloy Thin Films," tech. rep., Technical Report No. UCB/EECS-2018-53 University of California at Berkeley, 2018.

[56] R. N. Simons, N. I. Dib, and L. P. Katehi, "Modeling of Coplanar Stripline Discontinuities," *IEEE transactions on microwave theory and techniques*, vol. 44, no. 5, pp. 711–716, 1996.

[57] "Microwaves101, https://www.microwaves101.com/calculators/864-coplanar-waveguide-calculator," 2021.

[58] H. Maier-Flaig, S. T. Goennenwein, R. Ohshima, M. Shiraishi, R. Gross, H. Huebl, and M. Weiler, "Note: Derivative Divide, A Method for the Analysis of Broadband Ferromagnetic Resonance in the Frequency Domain," *Review of Scientific Instruments*, vol. 89, no. 7, p. 076101, 2018.

[59] M. Back, "Out-of-Plane Ferromagnetic Resonance (FMR) Measurements on Magnetic Nanoparticle Dispersions for Biomedical Sensor Applications," 2020.

[60] *Spin-Pumping and Two-magnon Scattering in Magnetic Multilayers, author=Woltersdorf, Georg.* PhD thesis, Sinon Fraser University, 2004.

[61] C. Luo, Z. Feng, Y. Fu, W. Zhang, P. Wong, Z. Kou, Y. Zhai, H. Ding, M. Farle, J. Du, *et al.*, "Enhancement of Magnetization Damping Coefficient of Permalloy Thin Films with Dilute Nd Dopants," *Physical Review B*, vol. 89, no. 18, p. 184412, 2014.

[62] E. Montoya, T. Sebastian, H. Schultheiss, B. Heinrich, R. E. Camley, and Z. Celinski, "Magnetization Dynamics," in *Handbook of Surface Science*, vol. 5, pp. 113–167, Elsevier, 2015.

[63] J. O. Rantschler, B. Maranville, J. J. Mallett, P. Chen, R. D. McMichael, and W. F. Egelhoff, "Damping at Normal Metal/Permalloy Interfaces," *IEEE transactions on magnetics*, vol. 41, no. 10, pp. 3523–3525, 2005.

[64] Y. Zhao, Q. Song, S.-H. Yang, T. Su, W. Yuan, S. S. Parkin, J. Shi, and W. Han, "Experimental Investigation of Temperature-Dependent Gilbert Damping in Permalloy Thin Films," *Scientific reports*, vol. 6, no. 1, pp. 1–8, 2016.

[65] E. Montoya, T. McKinnon, A. Zamani, E. Girt, and B. Heinrich, "Broadband Ferromagnetic Resonance System and Methods for Ultrathin Magnetic Films," *Journal of magnetism and magnetic materials*, vol. 356, pp. 12–20, 2014.

[66] J. H. Scofield, "Frequency-Domain Description of a Lock-In Amplifier," *American journal of physics*, vol. 62, no. 2, pp. 129–133, 1994.

[67] M. Hayashi, J. Kim, M. Yamanouchi, and H. Ohno, "Quantitative Characterization of the Spin-Orbit Torque using Harmonic Hall Voltage Measurements," *Physical Review B*, vol. 89, no. 14, p. 144425, 2014.